

**DEVELOPMENT OF THE OPTICAL SYSTEM  
OF THE FIRST UNDULATOR BEAMLIN  
FOR THE SIAM PHOTON LABORATORY**

**Anusorn Tong-on**

**A Thesis Submitted in Partial Fulfillment of the Requirements for the**

**Degree of Doctor of Philosophy in Physics**

**Suranaree University of Technology**

**Academic Year 2010**

**DEVELOPMENT OF THE OPTICAL SYSTEM  
OF THE FIRST UNDULATOR BEAMLIN  
FOR THE SIAM PHOTON LABORATORY**

Suranaree University of Technology has approved this thesis submitted in partial fulfillment of the requirements for the Degree of Doctor of Philosophy.

Thesis Examining Committee

---

(Asst. Prof. Dr. Rattikorn Yimnirun)

Chairperson

---

(Assoc. Prof. Dr. Prayoon Songsiriritthigul)

Member (Thesis Advisor)

---

(Dr. Hideki Nakajima)

Member

---

(Assoc. Prof. Dr. Vittaya Amornkitbamrung)

Member

---

(Dr. Saroj Rujirawat)

Member

---

(Prof. Dr. Sukit Limpijumnong) (Assoc. Prof. Dr. Prapun Manyum)

Vice Rector for Academic Affairs Dean of Institute of Science

อนุสรณ์ ตองอ่อน : การพัฒนาระบบทัศนศาสตร์ของระบบลำเลียงแสงอันดูลเตอร์แรก  
สำหรับห้องปฏิบัติการแสงสยาม (DEVELOPMENT OF THE OPTICAL SYSTEM OF  
THE FIRST UNDULATOR BEAMLINE FOR THE SIAM PHOTON LABORATORY)  
อาจารย์ที่ปรึกษา : รองศาสตราจารย์ ดร.ประยูร สังกสิริฤทธิกุล, 142 หน้า.

ระบบลำเลียงแสงที่มาจากอันดูลเตอร์ของห้องปฏิบัติการแสงสยาม ถูกออกแบบและสร้าง  
ขึ้นเพื่อใช้วิเคราะห์โครงสร้างอิเล็กทรอนิกส์และพื้นผิวของวัสดุ โดยระบบดังกล่าวลำเลียงแสงที่มี  
พลังงานของโฟตอนในช่วง 40-160 และ 220-1040 อิเล็กตรอนโวลต์ สำหรับใช้ในการทดลอง  
ทางด้านโฟโตอิมิชชัน และจุลทรรศน์อิเล็กตรอนแบบโฟโตอิมิชชัน เพื่อที่จะทำให้มีการใช้แสง  
ที่มาจากอันดูลเตอร์อย่างมีประสิทธิภาพสูงสุด จึงได้มีการออกแบบให้ระบบลำเลียงแสงมีการแยกการ  
ใช้แสงหลังผ่านการถูกคัดเลือกพลังงานเป็น 2 กิ่ง ซึ่งเรียกว่าระบบลำเลียงแสง BL3.2a: PES และ  
BL3.2b: PEEM ในการสร้างระบบลำเลียงแสงใหม่นี้ ได้นำอุปกรณ์เชิงกลเกือบทั้งหมดจากระบบ  
ลำเลียงแสง BL4 เก่าที่เลิกใช้งาน เช่น ระบบโฟกัสของกระจกส่วนหน้า ระบบคัดเลือกพลังงาน  
และ ระบบโฟกัสของกระจกส่วนหลัง อีกทั้งอุปกรณ์เชิงกลที่ได้ถูกออกแบบและผลิตขึ้นมาใหม่มาใช้  
งาน ได้แก่ ส่วนหน้าของระบบลำเลียงแสง ระบบโฟกัสของกระจกตัวที่สอง ระบบกระจกเพื่อเลือก  
สถานีทดลอง และระบบโฟกัสของกระจกแบบ K-B ส่วนการควบคุมอันดูลเตอร์และระบบ  
ทัศนศาสตร์ได้พัฒนาซอฟต์แวร์ขึ้นมาโดยใช้โปรแกรม LabView หลังจากได้ทำการติดตั้งเสร็จ  
เรียบร้อยแล้ว ได้ทำการทดลองวัดคุณลักษณะเชิงแสงของระบบลำเลียงแสง ได้มีการนำผลที่ได้จาก  
การทดลองมาเปรียบเทียบกับผลที่ได้จากการคำนวณ และจากการจำลองด้วยโปรแกรมจำลอง  
เส้นทางการเดินของแสง

สาขาวิชาฟิสิกส์  
ปีการศึกษา 2553

ลายมือชื่อนักศึกษา \_\_\_\_\_  
ลายมือชื่ออาจารย์ที่ปรึกษา \_\_\_\_\_

ANUSORN TONG-ON : DEVELOPMENT OF THE OPTICAL  
SYSTEM OF THE FIRST UNDULATOR BEAMLIN FOR THE SIAM  
PHOTON LABORATORY. THESIS ADVISOR : ASSOC. PROF.  
PRAYOON SONGSIRIRITTHIGUL, Ph.D. 142 PP.

The undulator beamline in the BL3 was designed for the surface science research. In the designed optics simulated by a ray-tracing program, the beamline delivers an undulator radiation to the experimental stations in the range of VUV (vacuum ultraviolet) and SX (soft X-rays) corresponding to a photon energy of 40 - 1040 eV, and the photon beam size at the sample position is in the order of micrometer with an intensity of about 2000 times, higher than that obtained from the bending magnet. In the mechanical design of the beamline under limited funding, most of the mechanical components were reused from the obsolete bending magnet beamline in the BL4, and vacuum components were fabricated in the in-house machining facility. The control softwares of the undulator and grating were also developed using a graphical programming software called LabView. To make the most uses of the U60 undulator radiation, the beamline was designed to be divided in two branches for two experimental techniques : angle-resolved photoemission spectroscopy and photoemission electron microscopy. After the construction was completed, the performance of the optical beamline based on the commissioning results was evaluated, and compared with the results from analytical calculations and ray-tracing simulations.

## ACKNOWLEDGEMENTS

I would like express my gratitude to Assoc. Prof. Dr. Prayoon Songsiriritthigul, my thesis advisor, for his encouragement and endless support. His comments and suggestions brought me to solve the problems. He is not only a great advisor but also a great boss and friend. I am also very thankful Assist. Prof. Dr. Ruttikorn Yimnirun, Dr. Hideki Nakajima, Assoc. Prof. Dr. Vittaya Amornkitbamrung, Dr. Saroj Rujirawat and Assist. Prof. Dr. Supagorn Rugmai for valuable advices, comments and suggestions for my thesis.

The work on the mechanical parts design and fabrication would have been impossible to finish without Mr. Methee Sophon, Mr. Sarunyu Chaichuay, Mr. Krerkrit Sittisard, Mr. Samrerng Duangnil, Mr. Denchay Bamrungkhao, Mr. Piyawat Pruekthaisong and technicians at the SLRI machine shop.

I like also thank Mr. Surachet Rattanasuporn and Mr. Nattaphol. Sumano, for the development of the control software and the assistance in beamline installation.

Financial support from the Synchrotron Light Research Institute (Public Organization) and Suranaree University of Technology for is acknowledged.

It is impossible to list all of my fellow graduate students that were a great support during my Ph.D. studies, for all the great times we had together.

Finally, I would like to thank my family as my mother, my father, my brothers, my daughter and my wife who always supports and encourages me.

Anusorn Tong-on

# CONTENTS

	<b>Page</b>
ABSTRACT IN THAI . . . . .	I
ABSTRACT IN ENGLISH . . . . .	II
ACKNOWLEDGEMENTS . . . . .	III
CONTENTS . . . . .	IV
LIST OF TABLES . . . . .	VII
LIST OF FIGURES . . . . .	VIII
LIST OF ABBREVIATIONS . . . . .	XIX
<b>CHAPTER</b>	
<b>I INTRODUCTION . . . . .</b>	<b>1</b>
<b>II SYNCHROTRON LIGHT . . . . .</b>	<b>4</b>
2.1 Synchrotron radiation source . . . . .	5
2.1.1 Bending magnet . . . . .	8
2.1.2 Insertion devices . . . . .	9
2.1.3 The Siam photon source . . . . .	13
2.2 Optical path . . . . .	13
2.3 Optical components . . . . .	19
2.3.1 Mirrors and reflective coating . . . . .	19
2.3.2 Focusing properties of single mirror . . . . .	20
2.3.3 Kirkpatrick - Baez systems . . . . .	23
2.3.4 Varied lines space plane grating (VLSPG) . . . . .	24
2.4 Synchrotron radiation based measurement techniques . . . . .	28

## CONTENTS (Continued)

	<b>Page</b>
2.4.1 Angle-Resolved Photoemission Spectroscopy (ARPES) . . .	32
2.4.2 X-ray photoelectron spectroscopy (XPS) . . . . .	34
2.4.3 Photoemission Electron Microscopy (PEEM) . . . . .	41
2.4.4 X-ray absorption spectroscopy (XAS) . . . . .	45
2.5 Beamline . . . . .	47
2.5.1 Photon-energy scanning mechanism . . . . .	49
2.5.2 Photodiode detector . . . . .	51
<b>III DESIGN CONSIDERATIONS . . . . .</b>	<b>55</b>
<b>IV OPTICAL DESIGN AND RESULTS . . . . .</b>	<b>64</b>
4.1 Optical layout . . . . .	64
4.2 Pre-focusing mirror . . . . .	69
4.2.1 Meridional focusing of pre-focusing mirror (M0) . . . . .	69
4.2.2 Sagittal focusing of pre-focusing mirror (M0) . . . . .	75
4.3 Monochromators . . . . .	77
4.4 Post-focusing mirrors . . . . .	84
4.4.1 Toriodal mirror for ARPES . . . . .	85
4.4.2 K-B mirrors for PEEM . . . . .	89
4.5 Flux at sample . . . . .	91
4.6 Beam size at sample position . . . . .	93
4.6.1 ARPES position . . . . .	93
4.6.2 PEEM position . . . . .	94
4.7 Resolving power . . . . .	98
4.8 Heat on the mask . . . . .	99

## CONTENTS (Continued)

	Page
<b>V COMMISSIONING RESULTS AND DISCUSSION . . . . .</b>	<b>103</b>
5.1 First photon beam alignment and PBPM results . . . . .	103
5.2 The undulator photon energy spectrum . . . . .	104
5.3 The pre-focusing mirror (M0) alignment . . . . .	106
5.4 The slit alignment . . . . .	109
5.5 The M0 stability . . . . .	111
5.6 Photon energy scanning mechanism of the U60 undulator . . . . .	112
5.7 Photon energy calibration of the VLSPGs . . . . .	115
5.8 Harmonic photon energy shift (red shift) . . . . .	116
5.9 Flux measurement at sample position . . . . .	118
<b>VI CONCLUSIONS . . . . .</b>	<b>122</b>
<b>REFERENCES . . . . .</b>	<b>124</b>
<b>APPENDICES</b>	
APPENDIX A APPENDICES . . . . .	130
A.1 BL3 front-end . . . . .	130
A.2 Vacuum system . . . . .	133
A.3 Interlock system . . . . .	136
APPENDIX B PUBLICATION PAPER . . . . .	138
<b>CURRICULUM VITAE . . . . .</b>	<b>142</b>

# LIST OF TABLES

Table		Page
2.1	Summary of SPS storage ring's main parameters. . . . .	15
2.2	The coefficients of $a_{ij}$ for toroid, paraboloid and ellipsoid surfaces. .	18
3.1	Parameters for the Undulator (U60) of the SPS. . . . .	57
3.2	Parameters for the photon source size and divergences of the un- dulator of the SPS. . . . .	57
4.1	Summary of the BL3 optical elements descriptions. . . . .	65
4.2	Summary of the Radius of curvature of M0 depend on the demag- nification. . . . .	72
4.3	Summary of the specifications of M0. . . . .	77
4.4	The optimized values of $E_1$ , $E_2$ , $E_3$ and $E_4$ that used for determin- ing the coefficient of line spacing and the exit arm length of the BL3's VLSPG gratings. . . . .	81
4.5	Summary of the specifications of M1/1. . . . .	81
4.6	Summary of the specifications of M1/2. . . . .	82
4.7	The specifications of the BL3's VLSPG gratings. . . . .	85
4.8	Summary of the specifications of M2Cy. . . . .	86
4.9	Summary of the specifications of M2T. . . . .	88
4.10	Summary of the specifications of M2V. . . . .	91
4.11	Summary of the specifications of M2H. . . . .	92
4.12	The properties of the water at temperature of 31°C. . . . .	99

# LIST OF FIGURES

Figure		Page
1.1	Calculated spectra of synchrotron light of the Siam Photon Source: The spectra are generated from the bending magnet of the storage ring, the U60 planar undulator and the 6.4-Tesla superconducting magnet wavelength shifter. . . . .	3
2.1	The electron beam coordinate system in the storage ring. . . . .	6
2.2	Parameter of the phase space ellipse. . . . .	7
2.3	Emission of synchrotron radiation from bending magnet. (a) Top view and (b) side view. . . . .	10
2.4	The layout of the storage ring of SPS. . . . .	14
2.5	Rays from the source $A$ incident on a surface $P(\xi, \omega, l)$ and form an image at $B$ . . . . .	16
2.6	The calculated reflectivity for nickel and gold with the grazing an- gles as a function of photon energies (a) P-polarized and (b) S- polarized. . . . .	21
2.7	The conventional definitions of the mirror configurations (a) toriod (b) paraboloid and (c) ellipsoid. . . . .	24
2.8	The Kirkpatrick-Baez optical system. . . . .	25
2.9	A diffraction grating showing the diffraction orders. . . . .	26
2.10	Schematic diagram of the sample-analyzer work function in a pho- toemission system. . . . .	33
2.11	Universal curve of electron mean free path (Briggs and Seah, 1990). . . . .	34

## LIST OF FIGURES (Continued)

<b>Figure</b>		<b>Page</b>
2.12	The layout of the end station of ARPES with in situ system. . . . .	35
2.13	Diagram of the PES system at Beamline 3.2a. . . . .	37
2.14	A cross section of the conventional concentric hemispherical ana- lyzer (CHA). . . . .	38
2.15	The diagram shows energy levels at the conducting sample and the electron analyzer in a PES measurement. . . . .	40
2.16	chematic diagram of X-PEEM. . . . .	42
2.17	Contrast mechanism of X-PEEM. . . . .	43
2.18	The total electron yield mode of recording in XAS. . . . .	47
2.19	The layout of the PEEM end station at Beamline 3.2b. . . . .	48
2.20	The sine-bar for the grating rotation of the BL3 beamline. . . . .	50
2.21	The picture of the grating chamber. The grating is rotated by a sine-bar which is driven by a DC stepping motor. The linear encoder is installed outside the chamber. . . . .	52
2.22	The quantum efficiency of the AXUV100A12 photodiode corre- sponding to the photon energy. . . . .	54
3.1	The experimental hall layout (shade area is the new extension area). . . . .	56
3.2	U60, the first undulator to be installed at the Siam Photon Labo- ratory. . . . .	56
3.3	Image of the photon source size of 60 mm period undulator for photon energy 40 eV. . . . .	58

## LIST OF FIGURES (Continued)

<b>Figure</b>	<b>Page</b>
3.4	Image of the photon source divergence of 60 mm period undulator for photon energy 40 eV. . . . . 58
3.5	The vertical photon source size in the energy range of interest. . . . . 59
3.6	The divergences of the photon source in the energy range of interest. 60
3.7	Shows the calculated photon flux of 60 mm period undulator. Current in SPS storage ring is assumed to be 100 mA. . . . . 61
3.8	The power delivered by the undulator in function of the peak energy. Current in the storage ring is 100 mA. . . . . 61
3.9	Angular power density delivered by the U60 undulator with current in the storage ring 100 mA. . . . . 62
3.10	Angular power density delivered by the U60 undulator with current in the storage ring 100 mA. . . . . 62
3.11	Angular power density delivered by the U60 undulator with current in the storage ring 100 mA. . . . . 63
4.1	The optical layout of the BL3 beamline. . . . . 66
4.2	The schematic diagram of the focusing optical element in the BL3 beamline for ARPES branchline a) in the vertical direction b) in the horizontal direction. . . . . 67
4.3	The schematic diagram of the focusing optical element in the BL3 beamline for PEEM branchline a) in the vertical direction b) in the horizontal direction. . . . . 68
4.4	Reflection mirror with grazing incident geometry. . . . . 69

## LIST OF FIGURES (Continued)

<b>Figure</b>		<b>Page</b>
4.5	The focusing property of M0. The sagittal focusing of M0 is agreed with the calculation (circle) but the meridional focusing of M0 is shown the divergence beam (square). . . . .	70
4.6	The relation between the focal point and the radius of curvature of M0. . . . .	71
4.7	The images of the photon energy 40 eV at sample position which are optimized by simulation, a) demagnification is 10, b) demagnification is 15 and c) demagnification is 20. . . . .	73
4.8	Image of the photon energy 40 eV of the expected focusing position of M0 using the calculated radius of 142858 mm with demagnification 10. . . . .	74
4.9	Image of the photon energy 40 eV of the expected focusing position of M0 using the optimized radius of 232360 mm from simulations with demagnification 10. . . . .	74
4.10	Image at sample position using the calculated radius of 142858 mm with demagnification 10 for photon energy 40 eV. . . . .	75
4.11	Image at sample position using the optimized radius of 245299.4 mm from simulations with demagnification 10 for photon energy 40 eV. . . . .	75
4.12	The image of the pre-focusing mirror (M0) of the sagittal focus the beam onto the entrance slit (S1) for photon energy 40 eV. . . . .	76

## LIST OF FIGURES (Continued)

<b>Figure</b>		<b>Page</b>
4.13	The footprint of the pre-focusing mirror (M0) for photon energy 40 eV and opening angle $0.2 \times 1 \text{ mrad}^2$ in vertical and horizontal, respectively. The shade rectangular and the transparent rectangular are represented the optical active area and the dimension of M0, respectively. . . . .	77
4.14	The diagram of the BL3 monochromator section that consist of entrance slit (S1), X-Y aperture, two exchangeable focusing spherical mirrors (M1/1 and M1/2), VLSPG gratings and exit slit (S2). . . .	79
4.15	The convergent synchrotron beam hit on VLSPG. It should be noted that the differences of incidence angles and diffraction angles at point 1 and 2 are small different. . . . .	80
4.16	The footprint of the M1/1 mirror for photon energy 280 eV and opening angle $0.2 \times 1 \text{ mrad}^2$ in vertical and horizontal, respectively. The shade rectangular and the transparent rectangular are represented the optical active area and the dimension of M1/1 mirror, respectively. . . . .	82
4.17	The footprint of the M1/2 mirror for photon energy 40 eV and opening angle $0.2 \times 1 \text{ mrad}^2$ in vertical and horizontal, respectively. The shade rectangular and the transparent rectangular are represented the optical active area and the dimension of M1/2 mirror, respectively. . . . .	83

## LIST OF FIGURES (Continued)

Figure		Page
4.18	The footprint of the 1st VLSPG grating for photon energy 40 eV and opening angle $0.2 \times 1$ mrad <sup>2</sup> in vertical and horizontal, respectively. The shade rectangular and the transparent rectangular are represented the optical active area and the dimension of the 1st VLSPG grating, respectively. . . . .	84
4.19	The calculation of spherical, coma, defocus, tangent error aberrations and slit limited by the width of the entrance and the exit slit of the 1st grating of BL3 beamline. . . . .	86
4.20	The calculation of spherical, coma, defocus, tangent error aberrations and slit limited by the width of the entrance and the exit slit of the 2 <sup>nd</sup> and 3 <sup>rd</sup> grating of BL3 beamline. . . . .	87
4.21	The widths of entrance and exit slit with the photon energy for grating 1 (low photon energy) that obtain at a fixed resolution of $1 \times 10^{-4}$ . . . . .	88
4.22	The widths of entrance and exit slit with the photon energy for grating 2 and 3 (high photon energy) that obtain at a fixed resolution of $1 \times 10^{-4}$ . . . . .	89
4.23	The footprint of the M2Cy mirror for photon energy 40 eV and opening angle $0.2 \times 1$ mrad <sup>2</sup> in vertical and horizontal, respectively. The shade rectangular and the transparent rectangular are represented the optical active area and the dimension of the M2Cy mirror, respectively. . . . .	90

## LIST OF FIGURES (Continued)

<b>Figure</b>	<b>Page</b>	
4.24	The footprint of the M2T mirror for photon energy 40 eV and opening angle $0.2 \times 1 \text{ mrad}^2$ in vertical and horizontal, respectively. The shade rectangular and the transparent rectangular are represented the optical active area and the dimension of the M2T mirror, respectively. . . . .	91
4.25	The footprint of the M2V mirror for photon energy 40 eV and opening angle $0.2 \times 1 \text{ mrad}^2$ in vertical and horizontal, respectively. The shade rectangular and the transparent rectangular are represented the optical active area and the dimension of the M2V mirror, respectively. . . . .	92
4.26	The footprint of the M2H mirror for photon energy 40 eV and opening angle $0.2 \times 1 \text{ mrad}^2$ in vertical and horizontal, respectively. The shade rectangular and the transparent rectangular are represented the optical active area and the dimension of the M2H mirror, respectively. . . . .	93
4.27	Calculated flux of the PEEM branchline at sample position assuming an current in the storage ring 100 mA. The calculated flux includes the reflectivity of the mirrors, the efficiency of grating, the reflectivity of the grating and the beam intensity after the entrance and exit slits. . . . .	94
4.28	The beam size at ARPES sample position for the photon energy 40 eV which is used grating number 1 and opening angle of $0.2 \text{ mrad}^2$ .	95

## LIST OF FIGURES (Continued)

Figure		Page
4.29	The beam size at ARPES sample position for the photon energy 280 eV which is used grating number 2 and opening angle of 0.2 mrad <sup>2</sup> . . . . .	95
4.30	The beam size at ARPES sample position for the photon energy 600 eV which is used grating number 3 and opening angle of 0.2 mrad <sup>2</sup> . . . . .	96
4.31	The beam size at PEEM sample position for the photon energy 40 eV which is used grating number 1 and opening angle of 0.2 mrad <sup>2</sup> . . . . .	96
4.32	The beam size at PEEM sample position for the photon energy 280 eV which is used grating number 2 and opening angle of 0.2 mrad <sup>2</sup> . . . . .	97
4.33	The beam size at PEEM sample position for the photon energy 600 eV which is used grating number 3 and opening angle of 0.2 mrad <sup>2</sup> . . . . .	97
4.34	The beam profile at the sample position of PEEM with resolving power as 10000 and the opening angle of 0.2 mrad <sup>2</sup> . . . . .	99
4.35	The front view drawing of Mask of the BL3.2 beamline (a unit of length is millimeter). . . . .	100
4.36	The power distribution on the Mask. . . . .	102
5.1	The definitions of rotations and orientations of the pre-focusing mirror of the BL3.2 beamline. . . . .	104
5.2	The drain current measurement at behind entrance slit with slit width 100 $\mu\text{m}$ in the vertical translation (Z) of the pre-focusing mirror (M0). . . . .	105

## LIST OF FIGURES (Continued)

Figure	Page
5.3	The drain current measurement at behind entrance slit with slit width 100 $\mu\text{m}$ in the transversal translation (X) of the pre-focusing mirror (M0). . . . . 106
5.4	The drain current measurement at behind entrance slit with slit width 100 $\mu\text{m}$ in the yaw ( $\theta_z$ ) of the pre-focusing mirror (M0). . . . 107
5.5	The drain current measurement at behind entrance slit with slit width 100 $\mu\text{m}$ in the pitch ( $\theta_x$ ) of the pre-focusing mirror (M0). . . . 108
5.6	The in-house developed software is used to measure drain current for slits alignment. . . . . 109
5.7	The drain current measurement at behind entrance slit with slit width 100 $\mu\text{m}$ . . . . . 109
5.8	The drain current measurement at behind exit slit with slit width 100 $\mu\text{m}$ . . . . . 110
5.9	The drain current measurement as a function of time at behind entrance slit with slit width 100 $\mu\text{m}$ . . . . . 111
5.10	The beam size at entrance slit position before and after open ABS. 111
5.11	The relationship between the undulator gap and magnetic field. . . . 112
5.12	The in-house developed software which is used for scanning undulator. 113
5.13	The comparison of the U60 spectrum from the simulation and experiment results. . . . . 113
5.14	The photon wavelength calibration curve for VLSPGs of BL3.2 beamline by measured from photoemission spectra of gold. . . . . 114

## LIST OF FIGURES (Continued)

<b>Figure</b>		<b>Page</b>
5.15	The new in-house developed software which is developed for scanning the undulator and grating in the same time and energy. . . . .	115
5.16	The flux of the undulator from experiments is compared with simulation result. . . . .	117
5.17	The photoemission spectra of the Fermi edge of gold. . . . .	117
5.18	The drain current behind exit slit is measured by scanning photon energy with the undulator gap is 27 mm. . . . .	119
5.19	The drain current behind exit slit is measured by scanning photon energy with the undulator gap is 40 mm. . . . .	119
5.20	The drain current behind exit slit is measured by scanning photon energy with the undulator gap is 55 mm. . . . .	120
5.21	The photon flux measured and simulated in the beamline at the sample position. . . . .	121
A.1	The front-end drawing of the BL3 beamline. The exit gate valve is installed to isolate the vacuum from the storage ring. Top view (a) and side view (b), are shown. The radiation source from U60 and bending magnet are passed through to the front-end. . . . .	131
A.2	The photo of the front chamber of the BL3 beamline front-end. The image shows that the components are installed and aligned with the optical axis. . . . .	132
A.3	The photo of the front-end of the BL3 beamline connected to the bending magnet port number 3. . . . .	133

## LIST OF FIGURES (Continued)

<b>Figure</b>		<b>Page</b>
A.4	The diagram of vacuum system of the BL3 beamline. . . . .	135
A.5	The drawing of the BL3 beamline. The drawing is shown the PEEM branchline (top) and the ARPES branchline (bottom).When the M2Cy mirror is out of the optical axis, the monochromatic beam is passed to the PEEM. On the other hand, when the M2Cy mirror is in the optical axis, the monochromatic beam is passed to the ARPES.	135
A.6	The block diagram of the interlock system for the BL3 beamline. . .	137
A.7	The diagram of interlock of the BL3 beamline on the touch screen monitor. . . . .	137

## LIST OF ABBREVIATIONS

$a$	major axis of ellipse
$a_{ij}$	coefficients for the mirror surfaces
$a_1, a_2, a_3$	spacing parameters
A	ampere
A	antiferromagnetic axis
	angstrom
$\alpha$	(1) twiss parameter, (2) incident angle of mirror and grating, (3) acceptance angle of the electron beam
$b$	minor axis of ellipse
B	magnetic field amplitude
$B_0$	peak magnetic field
$B_y$	magnetic field in the horizontal plane
$\beta$	(1) twiss parameter, (2) reflection angle of mirror, (3) diffraction angle of grating
$c$	speed of light in vacuum (= 2.99792458 108 m s <sup>-1</sup> )
°C	degree Celcius
$d$	(1) grating groove spacing, (2) slit width of electron energy analyzer and (3) sample thickness
$D$	diameter
DM	demagnification
$dx/ds, dy/ds$	divergence of the electron moving around the ideal orbit
$D$	diameter
DM	demagnification
$dx/ds, dy/ds$	divergence of the electron moving around the ideal orbit
$\left. \frac{d\dot{N}}{d\Omega} \right _{\psi=0}$	spectral angular flux density
$\Delta E/E$	resolution

## LIST OF ABBREVIATIONS (Continued)

$\Delta s_1$	slit width of the entrance slit
$\Delta s_2$	slit width of the exit slit
$\Delta V$	voltage difference between the inner and outer hemispheres of electron energy analyzer
$e$	electron charge (1.602176 10 <sup>-19</sup> C)
<i>etal.</i>	et alia (and other)
$eV$	electron-Volt
$E_e$	electron energy
$E_b$	binding energy of electron
$E_{kin}$	kinetic energy of electron
$E_{analysis}^k$	kinetic energy of the electron inside the analyzer
$E_p$	pass energy of electron
<i>varepsilon</i>	emittance of electron beam
<i>varepsilon<sub>c</sub></i>	critical photon energy
$F$	optical path function
$GeV$	gigaelectron volts
$\gamma$	(1) relativistic factor, (2) twiss parameter
$h$	Plank constant
$I$	(1) electron beam current, (2) intensity of transmitted X-ray, (3) photo current
$I_0$	intensity of incident X-ray
$I_e$	total electron yield
$J$	Bessel function
$k$	order of diffraction
$keV$	kiloelectron volts
$kW$	kilowatts

## LIST OF ABBREVIATIONS (Continued)

$K$	magnetic field strength
$K_{2/3}, K_{5/3}$	modified Bessel function of the second kind
$L$	(1) undulator length, (2) length of the sine-bar
$\lambda$	photon wavelength
$\lambda_n$	the $n$ th harmonic wave length of undulator
$\lambda_u$	period length of undulator
$\lambda_w$	period length of wiggler
m	meter
mm	millimeter
$m_0$	electron rest mass
mA	milliampere
$\mu$	absorption coefficient
n	harmonic number of undulator
N	groove density of grating
$N_0$	constant lines groove density
$\pi$	Pi (= 22/7)
$\pi\varepsilon$	ellipse area in phase space
$\phi$	(1) included angle of grating, (2) rotating angle of grating
$\Phi$	work function of the spectrometer
$r$	source distance
$r'$	image distance
$R$	(1) major radius of mirror, (2) linear displacement
$R_1, R_2$	inner and outer hemisphere of curvature of analyzer
$\rho$	(1) bending magnet radius, (2) minor radius of mirror
s	second
SX	soft X-ray

**LIST OF ABBREVIATIONS (Continued)**

$\sigma_u$	electron beam size
$\sigma_{u'}$	electron beam divergence
$\sigma_\Psi$	root-mean-square divergence
$\sigma_s, \sigma_z$	effective electron beam sizes
$\sigma'_s, \sigma'_z$	effective electron beam divergences
$\sigma_r, \sigma'_r$	diffraction limited of undulator
$\Sigma_x, \Sigma_z$	effective photon beam sizes
$\Sigma'_x, \Sigma'_z$	effective photon beam divergences
T	tesla
$\theta$	(1) observation angle, (2) incident angle of mirror, (3) deviation angle of grating
U60	undulator of 60 mm of period length
VUV	vacuum ultra violet

# CHAPTER I

## INTRODUCTION

Synchrotron light/radiation is an electromagnetic wave emitted from a relativistic charge particle moving in a curved motion. The first observation of “man-made” synchrotron light was reported by scientists at the General Electron Research Laboratory in US in 1947 (Elder et al., 1947). Synchrotron light is an unwanted phenomenon for the community of high-energy or nuclear physicists since it was considered as an obstructor for accelerating high-energy charged particles. Not until the middle of 1960s, a small group of solid state physicists has demonstrated the usefulness of synchrotron radiation from the accelerator for the high-energy physics research in a parasite mode (Codling, 1997). Thereafter, the salient properties of synchrotron light such as high brightness, well collimated and continuously spectra are well accepted by scientists in many different research areas. The demand for beamtime of synchrotron light has rapidly increased, resulting in several new projects around the world to build dedicated synchrotron light sources, which are known as second generation light sources. Since the beginning of 1980s, many scientists around the world have benefited from the excellent properties of synchrotron light from the second generation light sources. At present, many advanced synchrotron research facilities are now operating their third generation light sources, which utilize insertion devices such as undulators and wigglers to produce synchrotron light with much higher intensity and brightness. Meanwhile many advanced facilities are now developing the fourth-generation light sources, which are know as free-electron lasers covering from infrared to X-ray energy spec-

trum.

The first Thai synchrotron light source is known as the Siam Photon Source, installed at the Siam Photon Laboratory of the Synchrotron Light Research Institute (Public Organization). The light source is a modified source of the original SORTEC machine, which was previously located in Tsukuba in Japan. The modifications transform the SORTEC light source designed solely for the lithographic research to a new light source suitable for general purposes such as imaging, lithography, spectroscopy and scattering/diffraction experiments. The storage ring of the Siam Photon Source has been upgraded from 1.0 to 1.2 GeV to extend high-energy region of the synchrotron light spectra generated by the bending magnets. In addition, a superconducting wavelength shifter is planned to be installed in the storage ring to provide hard X-rays. At present, the brightest synchrotron light of the Siam Photon Source is generated by a planar undulator (U60) with a period length of 60 mm and a number of periods of 41. This U60 produces light in VUV (vacuum ultraviolet) and SX (soft X-rays) regions.

Figure 1.1 shows calculated spectra of synchrotron light generated by the bending magnets of the storage ring, the U60 planar undulator and from a 6.4-Tesla superconducting wavelength shifter of the Siam Photon Source. The flux density of synchrotron light from the U60 undulator is almost 4 orders of magnitude higher than that produced from the bending magnet. It is also interesting to point out that the U60 light spectra cover all K-edge of important light elements such as C (284.2 eV), N (409.9 eV) and O (543.1 eV), and L-edge of important metals starting from light element Na up to 3d transition metal Ni (Williams, 2001). The U60 may be considered as the most valuable light. It will be used for as many as possible research areas and various measurement techniques. At the initial stage, four different experimental stations are installed for different kinds of mea-

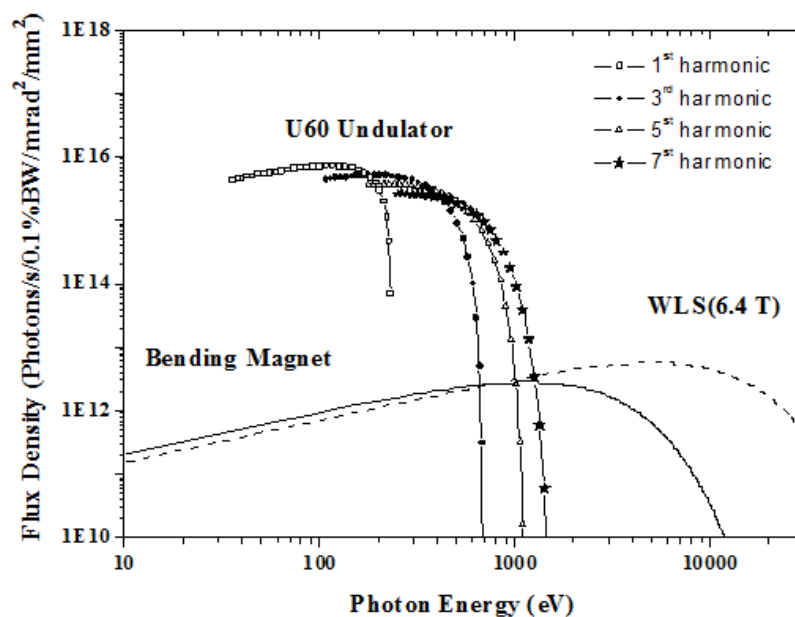


**Figure 1.1** Calculated spectra of synchrotron light of the Siam Photon Source: The spectra are generated from the bending magnet of the storage ring, the U60 planar undulator and the 6.4-Tesla superconducting magnet wavelength shifter.

surement techniques, i.e. angle-resolved photoemission spectroscopy (ARPES), X-ray photoelectron spectroscopy (XPS), X-ray absorption spectroscopy (XAS) and photoemission electron microscopy (PEEM). To make the most uses of the U60 light, a beamline to deliver light from the U60 to the experimental station must be carefully designed and constructed. Thus, the main goal of this thesis work is to design and construct a synchrotron light beamline to utilize the U60 light for the above mentioned experiments.

# CHAPTER II

## SYNCHROTRON LIGHT

This chapter provides the background necessary for designing an optical beamline to deliver light from the light source to the experimental station. It is crucial to know the characteristics of the light source such as dimensions and angular distribution of emitting light. These parameters can be obtained once the characteristics of the electron beam and the magnetic field are known. Thus, understanding of the electron beam optics is necessary. Brief mathematic formulas for the electron beam will be given. For light optics, the optical path function will be mentioned in details as it is necessary for both analytical considerations and ray tracing simulations for the design of a beamline.

It is also worth to emphasize the salient properties of synchrotron light, which can be summarized as the followings:

***Continuous spectrum:*** The spectrum of synchrotron light emitted from a bending magnet or a wiggler is continuous. The spectral range may cover from the infrared to X-rays, depending on the electron energy and the magnetic field. Undulator light exhibits a strong interference peak at certain photon energy. However, the position of the peak can be adjusted by changing the gap of the undulator. Thus, synchrotron light becomes a tunable light source.

***High flux and high brilliance:*** The flux from emitted radiation is very high and many order of magnitudes compared with conventional X-ray tubes. This is due to the facts that the electron beam source has very small beam size and very low divergence.

***Low emittance and high collimation:*** Electron beam optics is well-established technology. In principle, an electron beam can nowadays be controlled to be as small as nano-meter diameter. The photon beam has a small source size and low angular divergence. So the photon beam can be focused down to  $1 \mu\text{m}$ .

***Polarization:*** The emitted radiation from the bending magnet has linear polarization in the plane of the storage ring. Except above and below this plane, the bending magnet radiation is elliptically polarized. And it is suited for the dichroism experiment, e.g. investigating magnetic materials (Winick, 1994).

***Pulse time structure:*** The electrons are stored in the storage ring as a group of bunches. The bunching is caused by the RF cavity. In the optical beamline, when an electron bunch passes we can see continuous synchrotron radiation. Since the electron in the storage ring is filled with some electron bunches, the synchrotron radiation is emitted from each bunch as pulse (Winick, 1994).

## 2.1 Synchrotron radiation source

In the design of the beamline optics for the synchrotron radiation source, the parameters of the electrons in the storage ring must be known, because the photon beam size and divergence are crucially affected by the position of electron beam (Winick, 1994). Now, in a coordinate system as shown in figure 2.1, the electrons are assumed to be located at a point  $P(x,y)$  in an  $x$ - $y$  plane along the ideal orbit. The direction of the electron motion  $s$  is perpendicular to the two orthogonal  $x$  and  $y$  directions. The two derivatives, namely  $dx/ds$  and  $dy/ds$  are the divergence of the electron moving around the ideal orbit. The distribution of the electron density may be approximated to be a Gaussian distribution, which can be characterized by four standard deviations  $\sigma_x$ ,  $\sigma_{x'}$  and  $\sigma_y$ ,  $\sigma_{y'}$  (corresponding to the beam size and beam divergence in the direction  $x$  and  $y$ , respectively). Here,

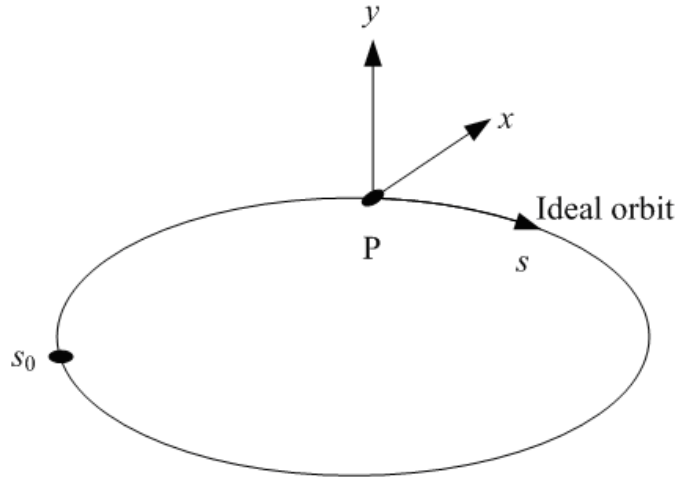


**Figure 2.1** The electron beam coordinate system in the storage ring.

the concept of the electron beam circulating around the storage ring is given only in a macroscopic view. However, the actual electron beam motion has its own betatron oscillation in the transverse direction of the ideal orbit. The details of the electron beam as a phase ellipse gives an average view of the electron beam at each point. The ellipse shows the electron beam contour where the electron beam width is a minimum (Duke, 2000). The generalized coordinates  $u$  and  $u'$  are used to represent the phase ellipses for both the  $x - x'$  and  $y - y'$  planes that can be described by

$$\varepsilon = qu^2 + ru'^2. \quad (2.1)$$

By comparing with the general equation for an ellipse with the origin at the center with major and minor axes or  $a$  and  $b$ , respectively;

$$\frac{u^2}{a^2} + \frac{u'^2}{b^2} = 1 \quad (2.2)$$

We obtain that the ellipse has the semi-major and semi-minor axes of lengths

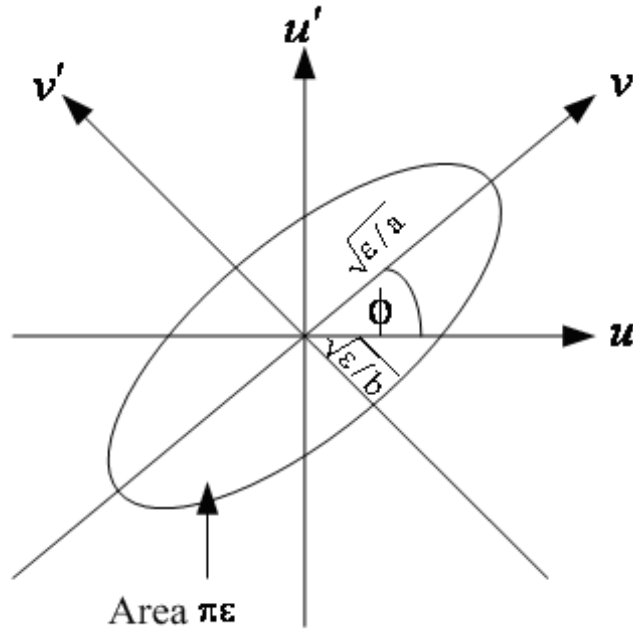


**Figure 2.2** Parameter of the phase space ellipse.

$2\sqrt{\epsilon/a}$ ,  $2\sqrt{\epsilon/b}$  and area  $\pi\epsilon$  with the condition  $ab = 1$ . The area  $\pi\epsilon$  is called the beam emittance. In order to provide a rigid the relation between the phase ellipse and beam dimension, the equation of the tilted ellipse is needed. The equation of an ellipse tilted through an angle of  $\phi$  relative to the  $u$ ,  $u'$  frame can be described by (Sands, 1970)

$$\epsilon = qv^2 + rv'^2. \quad (2.3)$$

The equation transformed from the  $v$ ,  $v'$  frame to the  $u$ ,  $u'$  frame is given by

$$\begin{aligned} v &= u\cos\phi + u'\sin\phi \\ v' &= -u\sin\phi + u'\cos\phi \end{aligned} \quad (2.4)$$

Putting the equation 2.4 into 2.3 leads to the general equation for the following phase space ellipse;

$$\varepsilon = \gamma u^2 + 2\alpha uu' + \beta u'^2 \quad (2.5)$$

$$\gamma = r \cos^2 \phi + q \sin^2 \phi \quad (2.6)$$

$$\beta = r \sin^2 \phi + q \cos^2 \phi \quad (2.7)$$

where

$$\left. \begin{aligned} 2\alpha &= (q - r) \sin 2\phi \\ \tan 2\phi &= \frac{-2\alpha}{\beta - \gamma} \end{aligned} \right\}, \quad (2.8)$$

and

$$\beta\gamma = 1 + \alpha^2. \quad (2.9)$$

The parameters  $\alpha$ ,  $\beta$  and  $\gamma$  are called the Twiss parameters. The beam size and angular distribution of the beam are considered to be the quantities defined as a root-mean-square value, which are given by

$$\left. \begin{aligned} \sigma_u &= \sqrt{\varepsilon_u \beta_u} \\ \sigma_{u'} &= \sqrt{\varepsilon_{u'} / \beta_{u'}} \end{aligned} \right\}. \quad (2.10)$$

### 2.1.1 Bending magnet

In the bending magnet, electrons move in a circular trajectory. The emitted radiation is intense, with a very narrow angular divergence of about  $\gamma^{-1}$  around the trajectory plane. The radius of curvature of the electron trajectory in the

bending magnet is given by (Peatman, 1997)

$$\rho[m] = \frac{3.3E_e[GeV]}{B[T]}, \quad (2.11)$$

where  $B$  is the magnetic field amplitude, and  $E_e$  is the energy of electron. The radiation from the bending magnet has a continuous spectrum distribution with the critical photon energy  $\varepsilon_c$  which in practical unit is

$$\varepsilon_c[keV] = 0.665E_e^2[GeV]B[T]. \quad (2.12)$$

The spectral angular flux density in a practical unit (photon per second per milliradian<sup>2</sup> per 0.1% bandwidth), is given by

$$\left. \frac{d\dot{N}}{d\Omega} \right|_{\psi=0} = 1.33 \times 10^{13} E_e^2[GeV] I[A] \left(\frac{\omega}{\omega_c}\right)^2 K_{2/3}^2\left(\frac{\omega}{2\omega_c}\right) \quad (2.13)$$

The most common method for estimating the vertical opening angle is to assume that the angular distribution is of a Gaussian shape and symmetric to  $\psi = 0$ . Then the root-mean-square divergence  $\sigma_\psi$  is (Kim, 1995)

$$\sigma_\psi = \left(\frac{2\pi}{3}\right)^{1/2} \frac{1}{\gamma} \left(\frac{\omega}{\omega_c}\right) \frac{\int_{\omega/\omega_c}^{\infty} K_{5/3}(u) du}{K_{2/3}^2(\omega/2\omega_c)}. \quad (2.14)$$

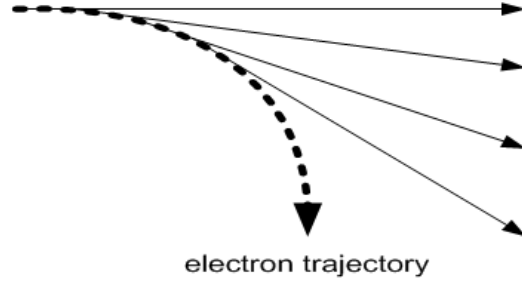
The total power emitted by the electron beam of current  $I$  is given by

$$P[kW] = 88.46 \frac{E_e^4[GeV] I[A]}{\rho[m]} \quad (2.15)$$

## 2.1.2 Insertion devices

### 2.1.2.1 Undulator

(a) Top view



(b) Side view

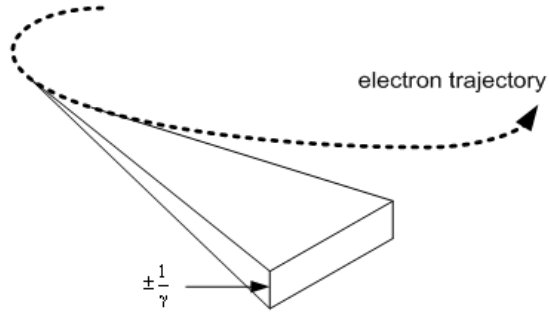


**Figure 2.3** Emission of synchrotron radiation from bending magnet. (a) Top view and (b) side view.

The undulator is an insertion device which consists of the periodic structure of static dipole magnets (Clarke, 2004). The radiation emitted by electrons at the various poles in the periodic magnet. The shape of the radiation is like a pencil. The  $n^{\text{th}}$  harmonic wavelength ( $\lambda_n$ ) of the undulator radiation on its axis can be obtained from the following equation; (Attwood et al., 1993)

$$\lambda_n \left[ \overset{0}{A} \right] = \frac{\lambda_u}{2n\gamma^2} \left[ 1 + \frac{K^2}{2} + \gamma^2\theta^2 \right] = \frac{1.3056 \lambda_u [mm]}{nE^2 [GeV]} \left[ 1 + \frac{K^2}{2} + \gamma^2\theta^2 \right], \quad (2.16)$$

where  $\gamma$  is the ratio of the electron energy to the electron rest mass,  $\theta$  is the observation angle with respect to the unperturbed orbit and  $K$  is the magnetic

field strength parameter, which is defined as (Attwood et al., 1993)

$$K = \frac{eB_0\lambda_u}{2\pi m_0 c} = 0.09337\lambda_u [mm] B_0 [T], \quad (2.17)$$

where  $B_0$  is the peak magnetic field, and corresponding photon energy,  $\varepsilon_n$  is expressed by

$$\varepsilon_n [keV] = 9.498 \frac{n E^2 [GeV]}{\lambda_u [mm] \left[1 + \frac{K^2}{2} + \gamma^2 \theta^2\right]}. \quad (2.18)$$

The effective sizes ( $\sigma_x, \sigma_z$ ) and divergences ( $\sigma'_x, \sigma'_z$ ) of the electron beam in the horizontal and the vertical directions and the diffraction limited ( $\sigma_r, \sigma'_r$ ) are used to calculate the effective sizes ( $\Sigma_x, \Sigma_z$ ) and divergences ( $\Sigma'_x, \Sigma'_z$ ) of the photon beam in the central cone. The effective sizes and divergences can be obtained from the following equation; (Shin, 1993)

$$\begin{aligned} \Sigma_x &= \sqrt{\sigma_x^2 + \sigma_r^2}, & \Sigma_z &= \sqrt{\sigma_z^2 + \sigma_r^2} \\ \Sigma'_x &= \sqrt{\sigma'^2_x + \sigma'^2_r}, & \Sigma'_z &= \sqrt{\sigma'^2_z + \sigma'^2_r} \end{aligned} \quad (2.19)$$

where

$$\left. \begin{aligned} \sigma_x &= \sqrt{\varepsilon_x \beta_x} \\ \sigma'_x &= \sqrt{\frac{\varepsilon_x}{\beta_x}} \\ \sigma_z &= \sqrt{\varepsilon_z \beta_z} \\ \sigma'_z &= \sqrt{\frac{\varepsilon_z}{\beta_z}} \\ \sigma_r &= \frac{1}{2\sqrt{2\pi}} \sqrt{\lambda L} \\ \sigma'_r &= \sqrt{\frac{\lambda}{2L}} \end{aligned} \right\}. \quad (2.20)$$

The peak angular flux density of the  $n^{th}$  harmonics in practical unit of

photon per second per milliradian<sup>2</sup> per 0.1% bandwidth is given by (Kim, 1995)

$$\left. \frac{d\dot{N}}{d\Omega} \right|_{\theta=0} = 1.74 \times 10^{14} N^2 E_e^2 [GeV] I[A] F_n(K), \quad n = 1, 3, 5, \dots \quad (2.21)$$

where

$$F_n(K) = \frac{n^2 K^2}{(1 + K^2/2)} \left[ J_{(n+1)/2} \left( \frac{nK^2}{4(1 + K^2/2)} \right) - J_{(n-1)/2} \left( \frac{nK^2}{4(1 + K^2/2)} \right) \right]^2. \quad (2.22)$$

The total power of the undulator radiation in practical unit is given by

$$P[kW] = 0.63 E_e^2 [GeV] B_0^2 [T] I[A] L[m]. \quad (2.23)$$

The thermal power of the undulator radiation from the high energy storage ring may be as strong as about 10 kilowatts per solid angle. To prevent the heat load problem on the inner wall of vacuum tubes and valves along the beamline, water-cooled mask was installed at the front-end of the beamline. Normally, most of the flux from the undulator radiation is concentrated in the central cone, so heat load effect on the optical elements is limited in the central cone of the undulator radiation.

### 2.1.2.2 Wavelength shifter and multipole Wiggler

The wavelength shifter (WLS) is an insertion device. It has a strong magnetic field more than that in the storage ring bending magnet (Clarke, 2004), and so the critical photon energy is increased up to a specific requirement of the beamline.

The multipole wiggler (MPW) is like several identical wavelength shifters aligned one after another in a straight section of a storage ring. Furthermore, if the magnetic field, which only deflects in the horizontal plane, is sinusoidal, with

period length  $\lambda_w$  , then

$$B_y(s) = -B_0 \sin\left(\frac{2\pi s}{\lambda_w}\right), \quad (2.24)$$

where  $B_0$  is the peak magnetic field.

The magnetic field strength parameter is defined same as equation 2.17, and the critical photon energy is given by (Sands, 1970)

$$\varepsilon_c[\text{keV}] = 0.655 E_e^2[\text{GeV}] B_0[\text{T}]. \quad (2.25)$$

### 2.1.3 The Siam photon source

The Siam photon Source (SPS) is the first synchrotron radiation source in Thailand. The layout of storage ring of the SPS which is operated at an electron beam energy of 1.2 GeV, is shown in Figure 2.4.

## 2.2 Optical path

In the VUV and SX regions, the conventional refraction type of the optical elements such as lenses used for focusing visible light cannot be used because of a very high absorption coefficient for all materials in these photon energy regions. Thus, the grazing incident reflection type of the optical elements is used. When the grazing angles are used to reflect the beam by mirrors of various shapes, the resolving powers critically depend on the mirror surface quality leading to the aberrations from a perfect image. The aberrations result from differences in the possible optical paths from one point to another through some geometrical surfaces.

In 1657, P. de Fermat provided the principle of least time to explain the

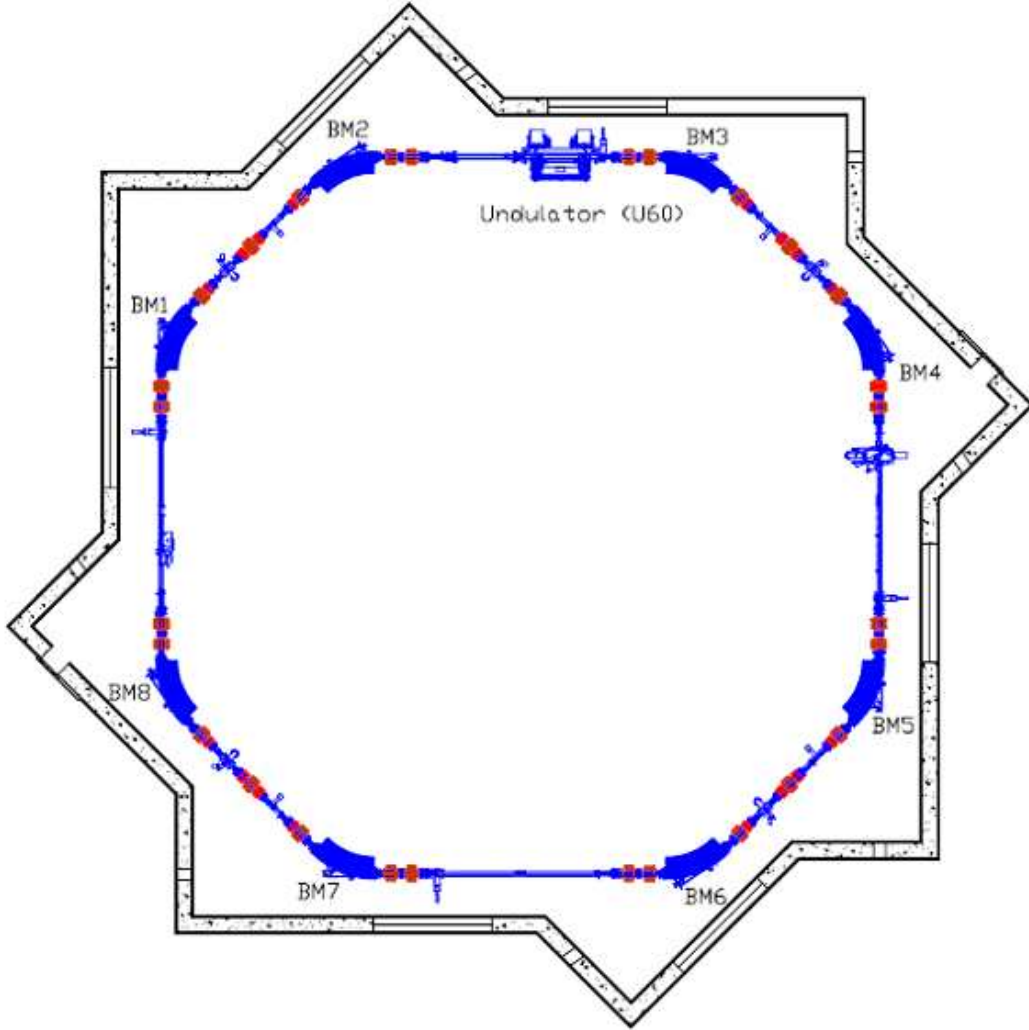


**Figure 2.4** The layout of the storage ring of SPS.

phenomena of refraction and reflection. The Fermat's principle states that a light ray from point  $A$  to point  $B$  and its optical path length are stationary. In Figure 2.5, the image at point  $B$  is formed by light rays from the point  $A$  impinging on an optical surface  $P(\xi, \omega, l)$ . The optical path function  $F$ , can be expressed as

$$F = \overline{AP} + \overline{PB}. \quad (2.26)$$

All paths through the mirror surface  $P(\xi, \omega, l)$ , which lead to a focus, must be fulfill

**Table 2.1** Summary of SPS storage ring's main parameters.

Parameters	Data
Operating electron beam energy	1.2 GeV
Circumference	81.3 m
Length of straight section	5.2 m $\times$ 4
Lattice	Double CityplaceBend Achromat (DBA)
Lattice symmetry	Four fold
Electron beam current	150 mA
RF frequency	118.080 MHz
Harmonic number	32
Natural chromaticity ( $\xi_x, \xi_y$ )	-8.56032, -6.64667
Betatron tune ( $\nu_x, \nu_y$ )	4.75580, 2.83703
Natural emittance	95.81 nm-rad
Momentum compaction factor	0.01828
Number of bending magnet	8
Bending magnet field	1.44 T
Bending radius	2.78 m
Critical energy from bending magnet	1.379 keV
Total power from bending magnet	6.599 kW

the following relations (Peatman, 1997).

$$\frac{\partial F}{\partial \omega} = 0 \quad (\text{meridional focus}) \quad (2.27)$$

$$\frac{\partial F}{\partial \ell} = 0 \quad (\text{sagittal focus}) \quad (2.28)$$

The general form of the surface of an optical element can be expressed by the following equation

$$\xi = \sum_{i=0}^{\infty} \sum_{j=0}^{\infty} a_{ij} \omega^i l^j, \quad a_{00} = a_{10} = 0, \quad j = \text{even}. \quad (2.29)$$

The  $a_{ij}$  coefficients for different surfaces are given in Table 2.1. In the polar

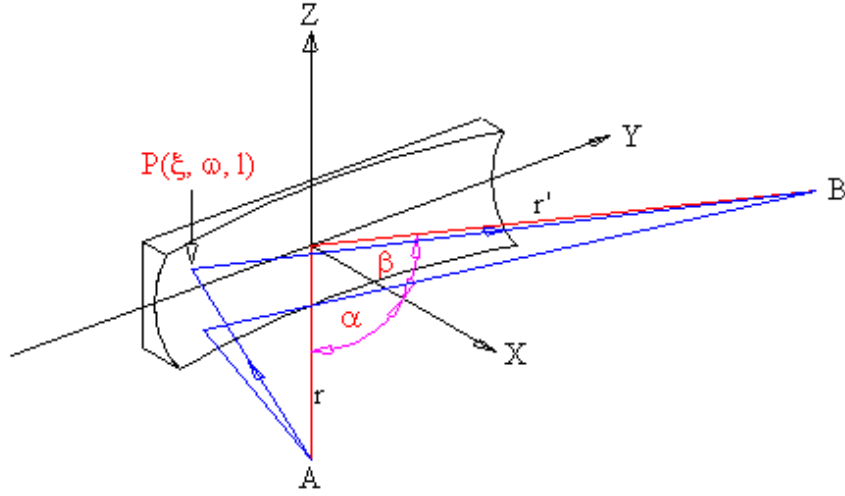


**Figure 2.5** Rays from the source  $A$  incident on a surface  $P(\xi, \omega, l)$  and form an image at  $B$ .

coordinate, the distance of  $\overline{AP}$  and  $\overline{PB}$  can be expressed as

$$\overline{AP} = \sqrt{(\xi - r \cos \alpha)^2 + (w - r \sin \alpha)^2 + (l - z)^2} \quad (2.30)$$

$$\overline{PB} = \sqrt{(\xi - r' \cos \alpha)^2 + (w - r' \sin \alpha)^2 + (l - z')^2}. \quad (2.31)$$

Substituting equations (2.29), (2.30) and (2.31) into equation (2.26), the light path function is then expressed into a power series of  $w$  and  $l$  as the following

$$\begin{aligned} F = & F_{000} + wF_{100} + \frac{1}{2}w^2F_{200} + \frac{1}{2}l^2F_{020} + \frac{1}{2}w^3F_{300} + \frac{1}{2}wl^2F_{120} + \frac{1}{8}w^4F_{400} \\ & + \frac{1}{4}w^2l^2F_{220} + \frac{1}{8}l^4F_{040} + lF_{011} + wlF_{111} + \frac{1}{2}wF_{102} + \frac{1}{4}w^2F_{202} + \frac{1}{2}w^2lF_{211} + \dots, \end{aligned} \quad (2.32)$$

where the important  $F_{ijk}$  terms are given below.

$$\begin{aligned}
F_{000} &= r + r' \\
F_{100} &= Nk\lambda - (\sin \alpha + \sin \beta) \\
F_{200} &= \left( \frac{\cos^2 \alpha}{r} \right) + \left( \frac{\cos^2 \beta}{r'} \right) - 2a_{20}(\cos \alpha + \cos \beta) \\
F_{020} &= \frac{1}{r} + \frac{1}{r'} - 2a_{02}(\cos \alpha + \cos \beta) \\
F_{300} &= \left[ \frac{T(r, \alpha)}{r} \right] \sin \alpha + \left[ \frac{T(r', \beta)}{r'} \right] \sin \beta - 2a_{30}(\cos \alpha + \cos \beta) \\
F_{120} &= \left[ \frac{S(r, \alpha)}{r} \right] \sin \alpha + \left[ \frac{S(r', \beta)}{r'} \right] \sin \beta - 2a_{12}(\cos \alpha + \cos \beta) \\
F_{400} &= \frac{4T(r, \alpha)}{r^2} \sin^2 \alpha - \frac{T^2(r, \alpha)}{r} + \frac{4T(r', \beta)}{r'^2} \sin^2 \beta - \frac{T^2(r', \beta)}{r'} \\
&\quad - 8a_{30} \left[ \frac{1}{r} (\sin \alpha \cos \alpha) + \frac{1}{r'} (\sin \beta \cos \beta) \right] - 8a_{40}(\cos \alpha + \cos \beta) + 4a_{20}^2 \left[ \frac{1}{r} + \frac{1}{r'} \right]
\end{aligned} \tag{2.33}$$

$$F_{100} = Nk\lambda - (\sin \alpha + \sin \beta) \text{ (grating equation)} \tag{2.34}$$

$$F_{200} = \left( \frac{\cos^2 \alpha}{r} \right) + \left( \frac{\cos^2 \beta}{r'} \right) - 2a_{20}(\cos \alpha + \cos \beta) \text{ (meridional focus)} \tag{2.35}$$

$$F_{020} = \frac{1}{r} + \frac{1}{r'} - 2a_{02}(\cos \alpha + \cos \beta) \text{ (sagittal focus)} \tag{2.36}$$

$$F_{300} = \left[ \frac{T(r, \alpha)}{r} \right] \sin \alpha + \left[ \frac{T(r', \beta)}{r'} \right] \sin \beta - 2a_{30}(\cos \alpha + \cos \beta) \text{ (primary coma)} \tag{2.37}$$

$$F_{120} = \left[ \frac{S(r, \alpha)}{r} \right] \sin \alpha + \left[ \frac{S(r', \beta)}{r'} \right] \sin \beta - 2a_{12}(\cos \alpha + \cos \beta) \text{ (astigmatic coma)} \tag{2.38}$$

$$\begin{aligned}
F_{400} &= \frac{4T(r, \alpha)}{r^2} \sin^2 \alpha - \frac{T^2(r, \alpha)}{r} + \frac{4T(r', \beta)}{r'^2} \sin^2 \beta - \frac{T^2(r', \beta)}{r'} \\
&\quad - 8a_{30} \left[ \frac{1}{r} (\sin \alpha \cos \alpha) + \frac{1}{r'} (\sin \beta \cos \beta) \right] - 8a_{40}(\cos \alpha + \cos \beta) + 4a_{20}^2 \left[ \frac{1}{r} + \frac{1}{r'} \right] \\
&\text{(spherical aberration)}
\end{aligned} \tag{2.39}$$

$$\begin{aligned}
F_{220} &= \frac{2S(r, \alpha)}{r^2} \sin^2 \alpha + \frac{2S(r', \beta)}{r'^2} \sin^2 \beta - \frac{T(r, \alpha)S(r, \alpha)}{r} - \frac{T(r', \beta)S(r', \beta)}{r'} \\
&+ 4a_{20}a_{02} \left[ \frac{1}{r} + \frac{1}{r'} \right] \\
&- 4a_{22}(\cos \alpha + \cos \beta) - 4a_{12} \left[ \frac{1}{r}(\sin \alpha \cos \alpha) + \frac{1}{r'}(\sin \beta \cos \beta) \right]
\end{aligned} \tag{2.40}$$

$$F_{040} = 4a_{02}^2 \left[ \frac{1}{r} + \frac{1}{r'} \right] - 8a_{04}(\cos \alpha + \cos \beta) \tag{2.41}$$

$$F_{011} = - \left( \frac{z}{r} + \frac{z'}{r'} \right) \tag{2.42}$$

$$F_{111} = - \left( \frac{z \sin \alpha}{r} + \frac{z' \sin \beta}{r'} \right) \tag{2.43}$$

$$F_{102} = \frac{z^2 \sin \alpha}{r^2} + \frac{z'^2 \sin \beta}{r'^2} \tag{2.44}$$

$$F_{202} = \left( \frac{z}{r} \right)^2 \left[ \frac{2 \sin^2 \alpha}{r} - T(r, \alpha) \right] + \left( \frac{z'}{r'} \right)^2 \left[ \frac{2 \sin^2 \beta}{r'} - T(r', \beta) \right] \tag{2.45}$$

$$F_{211} = \frac{z}{r^2} \left[ T(r, \alpha) - \frac{2 \sin^2 \alpha}{r} \right] + \frac{z'}{r'^2} \left[ T(r', \beta) - \frac{2 \sin^2 \beta}{r'} \right] \tag{2.46}$$

...

where  $T(r, \alpha) = \left( \frac{\cos^2 \alpha}{r} - 2a_{20} \cos \alpha \right)$  and  $S(r, \alpha) = \left( \frac{1}{r} - 2a_{02} \cos \alpha \right)$  and in the same way for  $T(r', \beta)$  and  $S(r', \beta)$ .  $N$  is a groove density of the grating in an unit of lines per millimeter, and  $k$  is diffraction order, which is an integer.

**Table 2.2** The coefficients of  $a_{ij}$  for toroid, paraboloid and ellipsoid surfaces.

$a_{ij}$	Toroid	Paraboloid	Ellipsoid
$a_{02}$	$\frac{1}{2\rho}$	$\frac{1}{4r' \cos \theta}$	$\frac{1}{4f \cos \theta}$
$a_{04}$	$\frac{1}{8\rho^3}$	$\frac{\sin^2 \theta}{64r'^3 \cos^3 \theta}$	$\frac{b^2}{64f^3 \cos^3 \theta} \left[ \frac{\sin^2 \theta}{b^2} + \frac{1}{a^2} \right]$
$a_{12}$	0	$-\frac{\tan \theta}{8r'^2}$	$\frac{\tan \theta}{8f^2 \cos \theta} (e^2 - \sin^2 \theta)^{1/2}$
$a_{20}$	$\frac{1}{2R}$	$\frac{\cos \theta}{4r'}$	$\frac{\cos \theta}{4f}$
$a_{22}$	$\frac{1}{4R^2 \rho}$	$\frac{3 \sin^2 \theta}{32r'^3 \cos \theta}$	$\frac{\sin^2 \theta}{16f^3 \cos^3 \theta} \left[ \frac{3}{2} \cos^2 \theta - \frac{b^2}{a^2} \left( 1 - \frac{\cos^2 \theta}{2} \right) \right]$
$a_{30}$	0	$-\frac{\sin \theta \cos \theta}{8r'^2}$	$\frac{\sin \theta}{8f^2} (e^2 - \sin^2 \theta)^{1/2}$

Ideally, an optical system is aberration-free when all the  $F_{ijk}$  terms vanish, which is always not the case for VUV and SX optics. This is due to the grazing

incidence geometry employed. In most beamline optics designs, the first seven terms are considered to suppress high-order aberrations.

## 2.3 Optical components

For hard X-ray, crystals are the most efficient dispersers. In the spectral range of the VUV to soft X-ray, the mechanically ruled reflection gratings have been used with various degrees of success. And mirrors are possible to use as focusing elements. The mirror shapes such as spherical, cylindrical, toroidal and etc are available.

### 2.3.1 Mirrors and reflective coating

The most important property of the mirror is reflectivity. The reflectivity of the mirror depends on the grazing angle and coating materials. Thus, the reflectivity can be increased when the grazing angle decreases. In addition, the material must be suitable for ultra-high vacuum.

At an angle of incidence, the reflectivity of the optical element with a negligible surface roughness can be described by Fresnel's equation. For an absorbing medium with the electric field vector of the light perpendicular ( $R_s$ ) and parallel ( $R_p$ ) to the plane of incidence, the complex reflection coefficient are respectively given below

$$R_s = \frac{[(a - \cos\theta)^2 + b^2]}{[(a + \cos\theta)^2 + b^2]} \quad (2.47)$$

$$R_p = \frac{R_s[(a - \sin\theta \tan\theta)^2 + b^2]}{[(a + \sin\theta \tan\theta)^2 + b^2]}, \quad (2.48)$$

where  $\theta$  is the incidence angle with respect to the normal line of surface,

$$a = \sqrt{\frac{1}{2}\{[(n^2 - k^2 - \sin^2\theta)^2 + 4n^2k^2]^{1/2} + (n^2 - k^2 - \sin^2\theta)\}} \quad (2.49)$$

$$b = \sqrt{\frac{1}{2}\{[(n^2 - k^2 - \sin^2\theta)^2 + 4n^2k^2]^{1/2} - (n^2 - k^2 - \sin^2\theta)\}} \quad (2.50)$$

where  $n$  and  $k$  are the real and imaginary parts of the complex index of refraction.

### 2.3.2 Focusing properties of single mirror

For the beamline design, the mirror configurations are the most important factor. The relation of the source distance ( $r$ ), the image distance ( $r'$ ) and the incidence angle ( $\theta$ ) for a toroid (sphere), parabola and ellipse are given below.

#### 2.3.2.1 Toroid : For the special case of a sphere, $\rho = R$ .

A toroidal mirror is commonly used in the beamlines, because the number of optical elements in a beamline can be reduced and commercially available. Form equations 2.35 and 2.36, all paths through the mirror surface  $P(\xi, \omega, l)$ , which lead to a focus, must be fulfilled the following relations  $\frac{\partial F}{\partial \omega} = \frac{\partial F}{\partial l} = 0$ , which lead to

$$\frac{1}{R} = \left(\frac{1}{r} + \frac{1}{r'}\right) \frac{\cos\theta}{2} \quad (2.51)$$

$$\frac{1}{\rho} = \left(\frac{1}{r} + \frac{1}{r'}\right) \frac{1}{2\cos\theta}. \quad (2.52)$$

#### 2.3.2.2 Parabola

A parabolic mirror is a specially shaped object, which functions due to the

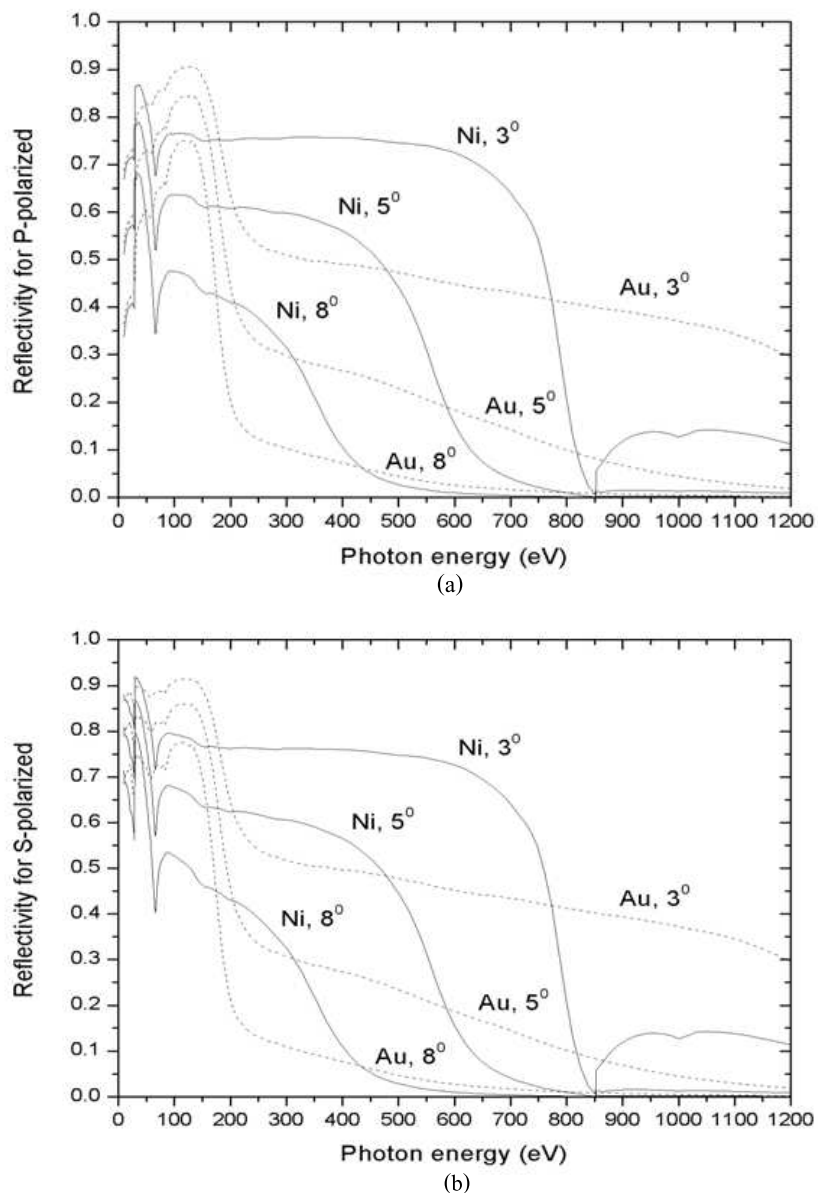


**Figure 2.6** The calculated reflectivity for nickel and gold with the grazing angles as a function of photon energies (a) P-polarized and (b) S-polarized.

geometric properties of the paraboloidal. When the incidence angle to the inner surface of the collector equals the angle of reflection, then the parallel waves of the light coming in to a parabolic mirror are focused at point  $F$ . The location of

the pole of the mirror surface  $P(\xi, \omega, l)$ , is given by

$$\left. \begin{aligned} X_0 &= a \tan^2 \theta \\ Y_0 &= 2a \tan \theta \end{aligned} \right\}, \quad (2.53)$$

where

$$a = r' \cos^2 \theta, \quad (2.54)$$

and the equation for a paraboloid is

$$y^2 + z^2 = 4a \cdot x. \quad (2.55)$$

### 2.3.2.3 Ellipse

Ellipsoidal mirrors have two connection foci. Light from one focal point is passed through the other after reflection. Ellipsoidal mirrors collect a much higher fraction of the total emitted light than a spherical mirror. Thus, they are also efficient over a much broader spectral range and they exhibit no chromatic aberration. In contrast, surfaces are difficult to manufacture, making them less than perfect and more expensive. The location of the pole of the mirror surface  $P(\xi, \omega, l)$ , is given by

$$\left. \begin{aligned} X_0 &= a \left(1 - \frac{Y_0^2}{b^2}\right)^{1/2} \\ Y_0 &= \frac{r \cdot r' \sin 2\theta}{2d} \end{aligned} \right\}, \quad (2.56)$$

where

$$\left. \begin{aligned} a &= \frac{1}{2}(r + r') \\ b &= (a^2 - d^2)^{1/2} \\ d &= \frac{1}{2}(r^2 + r'^2 - 2r \cdot r' \cos 2\theta)^{1/2} \end{aligned} \right\}, \quad (2.57)$$

and the equation for an ellipse is

$$\frac{x^2}{a^2} + \frac{y^2}{b^2} + \frac{z^2}{c^2} = 1. \quad (2.58)$$

### 2.3.3 Kirkpatrick - Baez systems

A Kirkpatrick – Baez system is a combination of two mirrors, which independently focus the object in two orthogonal planes. At the same time, they form a stigmatic focus in a common focal plane. Figure 2.8 shows the arrangement of the KB system. For our purpose we use two cylindrical mirrors in the configuration but curvature of vertical focusing mirror can also be adjustable.

To achieve a focused beam, it is necessary to satisfy the focus equations at the center of the first and second mirrors, given by

$$\left. \begin{aligned} \frac{1}{r_1} + \frac{1}{r'_1} &= \frac{2}{R_1 \cos \theta_1} \\ \frac{1}{r_2} + \frac{1}{r'_2} &= \frac{2}{R_2 \cos \theta_2} \end{aligned} \right\}, \quad (2.59)$$

where  $r_1$ ,  $r'_1$ ,  $r_2$  and  $r'_2$  are described in figure 2.8,  $R_1$  and  $R_2$  are the mirror curvatures and  $\theta_1$  and  $\theta_2$  are the angles of incidence for the first and second mirrors respectively.

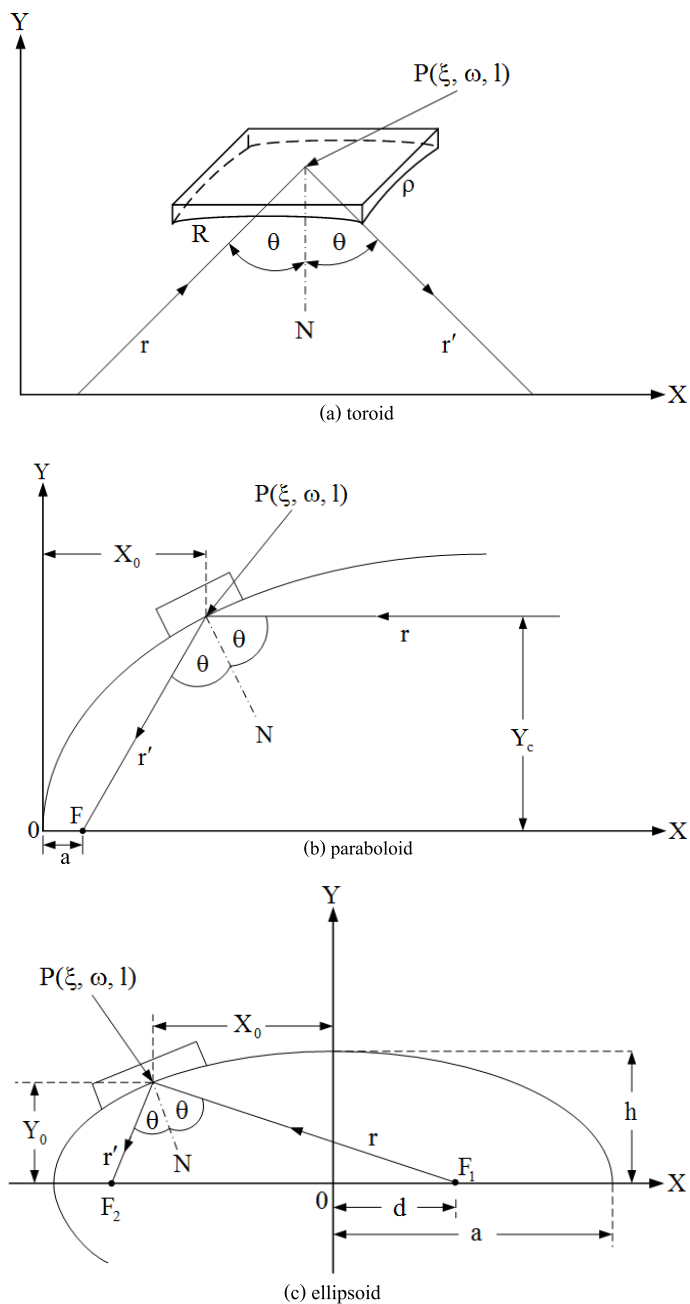


**Figure 2.7** The conventional definitions of the mirror configurations (a) toriod (b) paraboloid and (c) ellipsoid.

### 2.3.4 Varied lines space plane grating (VLSPG)

Light of wavelength  $\lambda$  incidents on a surface of the grating at an angle  $\alpha$  and is diffracted by a grating groove spacing of  $d$  along an angle of  $\beta$ . These angles are measured from the grating normal, which represents the dashed line perpendicular

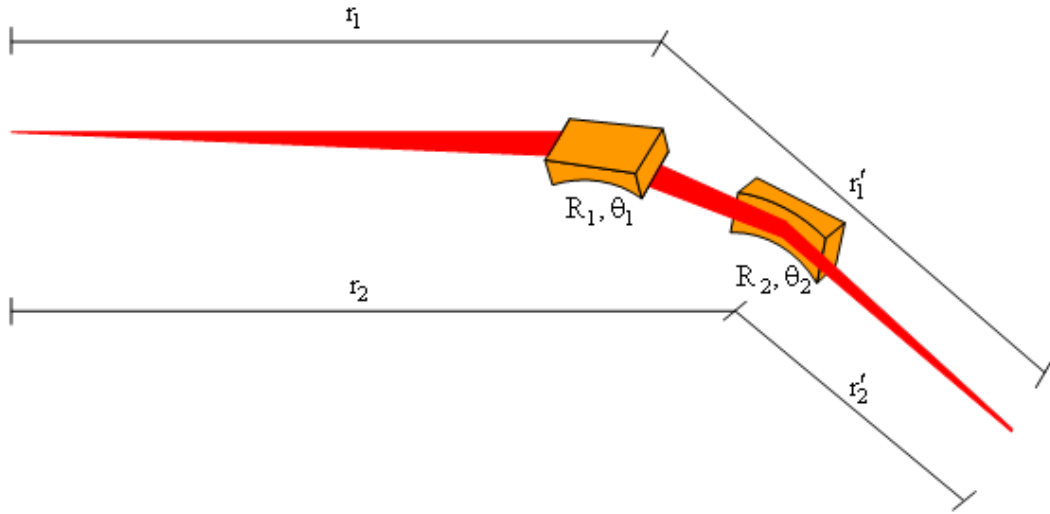


**Figure 2.8** The Kirkpatrick-Baez optical system.

to the surface of grating at its center in Figure 2.9. The sign convention for these angles depends on whether the light is diffracted on the same side or the opposite side of the grating as the incident light. The order of diffraction  $k$  is negative order when the angle  $\beta$  is bigger than the zero order light. These relationships are expressed by the grating equation

$$\left. \begin{aligned} 2\cos\theta \sin\phi &= \sin\alpha + \sin\beta = Nk\lambda \\ \theta &= \frac{\alpha - \beta}{2} \\ \phi &= \frac{\alpha + \beta}{2} \end{aligned} \right\} \quad (2.60)$$

where  $N = 1/d$  is the groove density in a practical unit of lines per millimeter, and  $\phi$  is the included angle of the grating.

For a plane grating, the major terms of the optical aberrations and the resolution,  $\Delta\lambda/\lambda$  or  $\Delta E/E$  which are called defocus, coma, astigmatic and spherical aberrations, respectively. The contribution of different types of the optical

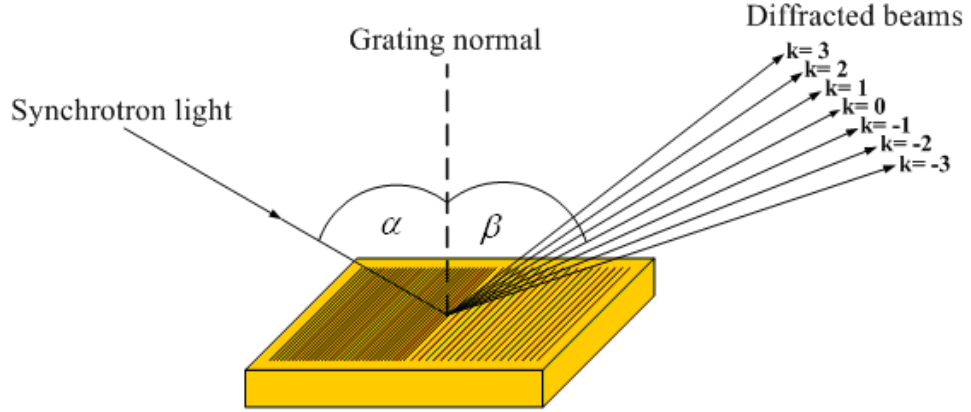


**Figure 2.9** A diffraction grating showing the diffraction orders.

aberrations to the resolution, which are given by

$$\left. \frac{\Delta\lambda}{\lambda} \right|_{Defocus} = \frac{\omega}{N(\omega)k\lambda} \left( \frac{\cos^2\alpha}{r} + \frac{\cos^2\beta}{r'} + N_0k\lambda a_1 \right) \quad (2.61)$$

$$\left. \frac{\Delta\lambda}{\lambda} \right|_{Coma} = \frac{3\omega^2}{2N(\omega)k\lambda} \left( \frac{\sin\alpha\cos^2\alpha}{r^2} + \frac{\sin\beta\cos^2\beta}{r'^2} + \frac{2}{3}N_0k\lambda a_2 \right) \quad (2.62)$$

$$\left. \frac{\Delta\lambda}{\lambda} \right|_{Astigmatic} = \frac{l^2}{2N(\omega)k\lambda} \left( \frac{\sin\alpha}{r^2} + \frac{\sin\beta}{r'^2} \right) \quad (2.63)$$

$$\left. \frac{\Delta\lambda}{\lambda} \right|_{Spherical} = \frac{\omega^3}{2N(\omega)k\lambda} \left\{ \frac{\cos^2\alpha}{r^3} (4\sin^2\alpha - \cos^2\alpha) + \frac{\cos^2\beta}{r'^3} (4\sin^2\beta - \cos^2\beta) + 2N_0k\lambda a_3 \right\} \quad (2.64)$$

,and

$$N(\omega) = N_0(1 + a_1\omega + a_2\omega^2 + a_3\omega^3 + \dots), \quad (2.65)$$

where  $N(\omega)$  is the groove density in the general case. For a constant lines grating,  $a_1 = a_2 = a_3 = 0$  then  $N(\omega) = N_0$ .

It is clear that these resolutions cannot be zero for all wavelengths. However, it is possible to minimize these resolutions by making the different types of optical aberrations vanishing at certain photon energy.

The spacing parameters  $a_1$  and the exit arm length  $r_2$  of VLSPG can be calculated by taking two values of photon energy ( $E_1, E_2$ ) chosen to make the defocus term vanishing.

$$a_1 = \frac{-1}{N_0 k \lambda_1} \left( \frac{\cos^2 \alpha_1}{r_1} + \frac{\cos^2 \beta_1}{r_2} \right) \quad (2.66)$$

$$r_2 = r_1 \frac{\lambda_2 \cos^2 \beta_1 - \lambda_1 \cos^2 \beta_2}{\lambda_1 \cos^2 \alpha_2 - \lambda_2 \cos^2 \alpha_1} \quad (2.67)$$

The spacing parameters  $a_2$  and  $a_3$  can be calculated by the coma and spherical terms vanishing at photon energies  $E_3$  and  $E_4$  respectively

$$a_2 = \frac{-3}{2N_0 k \lambda} \left( \frac{\sin \alpha \cos^2 \alpha}{r_1^2} + \frac{\sin \beta \cos^2 \beta}{r_2^2} \right) \quad (2.68)$$

$$a_3 = \frac{-1}{2N_0 k \lambda} \left\{ \frac{\cos^2 \alpha}{r_1^3} (4 \sin^2 \alpha - \cos^2 \alpha) + \frac{\cos^2 \beta}{r_2^3} (4 \sin^2 \beta - \cos^2 \beta) \right\}. \quad (2.69)$$

Furthermore, the tangent error of the grating  $\sigma_{te}$  and the slit width of both entrance and exit slits are also important factor that limits the resolution of the

monochromator section. The resolution defined by tangent error is given by

$$\left. \frac{\Delta\lambda}{\lambda} \right|_{Tangent\ error} = \frac{2 \cdot 2.35\sigma_{te}\cos\beta}{N_0k\lambda}, \quad (2.70)$$

where  $\sigma_{te}$  is the root-mean-square (rms) tangent error of the grating.

The slit limited resolution can be directly derived from the grating equation. The resolution of the slit limited are given by

$$\left. \frac{\Delta\lambda}{\lambda} \right|_{Entrance} = \frac{1}{N_0k\lambda} \frac{\Delta s_1}{r} \cos\alpha \quad (2.71)$$

$$\left. \frac{\Delta\lambda}{\lambda} \right|_{Exit} = \frac{1}{N_0k\lambda} \frac{\Delta s_2}{r'} \cos\beta, \quad (2.72)$$

where  $\Delta s_1$  and  $\Delta s_2$  are the slit widths of the entrance and exit slits, respectively.

## 2.4 Synchrotron radiation based measurement techniques

The continuous spectrum of synchrotron radiations can be used to reveal information of materials with atomic size up to biological cells, therefore providing possibility to explore many different kinds of material systems in many research areas such as physics, chemistry, materials science, crystallography, biology, medicine, geosciences, archeology and art history.

Energy, momentum, position and time are the parameters corresponding to three measurement techniques as spectroscopy, scattering or diffraction and microscopy.

(1) *Spectroscopy techniques* are used to study for the identification of samples that are emitted or absorbed by them and normally use to analyze chemical bonding.

- *Low photon energy spectroscopy techniques* such as photo emission spectroscopy (PES), angle-resolved photo emission spectroscopy (ARPES) and infrared spectroscopy (IR). Infrared and far-infrared (photon energy below 1 eV) are suited to investigate vibration and excitation mode. The VUV photon energy is in the range of 10 – 100 eV that is matched to study surface sciences thereby investigating electron – electron correlation in solids.

In 1998, E. Kukk and co-workers studied two dimension mapping of electron emission following Cl 2p excitation in the HCl molecule by ARPES. They were able to record two dimensional picture of electron emission from a diatomic molecule, hydrogen chloride, over a comprehensive energy range. The locations and intensities of emission lines identify processes such as excitation to unoccupied molecular orbitals, excitation to Rydberg orbitals, and ionization into the continuum. Diagonal lines indicate the absorption of X-rays by electrons in valence molecular orbitals rather than deep inside the chlorine atom (Kukk et al., 1998).

In 2004, D. Talbayev and co-workers studied spin interaction in magnetic oxides by FTIR. The parent compound for many of the Colossal MagnetoResistance (CMR) is lanthanum manganese oxide ( $\text{LaMnO}_3$ ). These CMR materials have been instrumental in enabling recent advances in magnetic storage devices. This study explain how the spins are “canted” relative to the crystal structure, and provide values for the interaction strength between different spins in the material (Talbayev and Zhou, 2004).

- *X-ray spectroscopy techniques* such as X-ray Photoemission Spectroscopy (XPS), X-ray Absorption Spectroscopy (XAS) and X-ray Magnetic Circular Dichroism (XMCD). XPS is used to measure chemical state, electronic state and the elemental composition. XAS is used to determine the local geometric ,elec-

tronic structure, element-, oxidation-state-, and symmetry-specific.

In 2004, P. Wernet et al., studied the structure of water by XAS. For 20 years, it has been commonly accepted that liquid water also forms a semi-tetrahedral structure. This study probed how chemical bonding perturbs the local valence electronic structure. From the data obtained, they concluded that liquid water consists mainly of structures with two strong hydrogen bonds, in contrast to the four bonds found in the tetrahedral structure of ice (Wernet et al., 2004).

(2) *Scattering or diffraction techniques* are used to produce the scattering or diffraction patterns when X-rays are scattered from the samples.

- *X-ray diffraction technique* such as protein crystallography (PX) is the most powerful technique for determining a three-dimensional picture of the density of electrons.

In 2000, P. Cramer et al., studied enzyme structure helps unravel mysteries of DNA by PX. Before a cell can begin to differentiate, the genetic information within the cell's DNA must be copied onto complementary strands of RNA. RNA polymerase II (pol II) is an enzyme that, by itself, can unwind the DNA double helix, synthesize RNA, and proofed the result. When combined with other molecules that regulate and control the transcription process, pol II is the key to successful interpretation of an organism's genetic code. However, the size, complexity, scarcity, and fragility of pol II complexes have made analysis of these macromolecules by PX a formidable challenge (Cramer et al., 2000).

In 2004, Y. Jiang et al., studied a membrane protein structure that causes of all communication between a cell and its environment that is mediated by them. They are critical in a variety of biological functions, including photosynthesis, vision, neural transmission, pathogenesis, and drug resistance. Membrane proteins control the electrochemical potentials that generate nerve impulses, transducer the

signaling functions of hormones, and even generate adenosine triphosphate (ATP) – the cell’s source of energy. Work on the voltage-dependent potassium channel, awarded the 2003 Nobel prize for chemistry (Jiang et al., 2003).

- *X-ray scattering techniques* such as small angle X-ray scattering (SAXS), wide angle X-ray scattering (WAXS) and grazing incidence small angle X-ray scattering (GISAXS). These techniques are used for investigations of the nanoscale structures. The results are informed of shapes, averaged particle sizes and distributions.

In 2003, H. Sinn et al., studied transport properties of molten aluminum oxide using high-resolution inelastic X-ray scattering. The transport properties of high-temperature oxide melts are of considerable interest for a variety of applications, including modeling the Earth’s mantle, optimizing aluminum production, confining nuclear waste, and investigating the use of aluminum in aerospace propulsion (Sinn et al., 2003).

(3) *Microscopy techniques* are used to view the interior structure of samples that cannot be seen by normal eyes.

- *X-ray microscopy techniques* such as photo emission electron microscopy (PEEM), scanning transmission X-ray microscopy (STXM). These techniques are matched to the imaging of the biological cells and surface sciences.

In 2004, C.A. Larabell et al., studied CAT scan of single cell using TXM. X-ray tomography is the first high-throughput imaging technology that generates images of whole, hydrated cells at better than 60 nm resolution (Larabell and Le Gros, 2004).

- *Infrared microscopy techniques* such as Raman microscopy. This technique is used to characterize vibrational frequencies as specific to symmetry of molecules and chemical bonds.

In 2002, L.M. Miller et al., studied misfolded protein structure in Alzheimer's disease using infrared microscope. Alzheimer's disease is characterized by the death of nerve cells in particular regions of the brain. The brain shrinks as gaps develop in the temporal lobe and hippocampus, which are responsible for storing and retrieving new information. Infrared imaging is used to determine their structures within brain tissue. At the same time, it is also used to study the health of the nerve cells surrounding the plaques and tangles in the brain tissue (Miller et al., 2002).

Furthermore, the BL3 beamline is designed for the surface science experiments. The most widely used techniques to study chemical properties of surface on solid materials are photoemission spectroscopy (PES) and photoemission electron microscopy (PEEM).

### 2.4.1 Angle-Resolved Photoemission Spectroscopy (ARPES)

PES is one of the most widely used techniques to study chemical, electronic, and structure properties of the solid materials. The technique is a modern application of the photoelectric effect originally observed by H. Hertz and later explained in 1905 by Albert Einstein. When the photon beam is on a sample, an electron can absorb the energy of the photon and then escape from the material with maximum kinetic energy, which is given by the following equation

$$E_{kin} = h\nu - E_b - \phi_{sample} \quad (2.73)$$

where  $h\nu$  is the monochromatic photon energy,  $E_b$  is the binding energy of the electron and  $\phi_{sample}$  is the sample work function. But the measured value is the

kinetic energy of the electron inside the analyzer ( $E_{analyzer}^k$ ), as illustrated in figure 2.10. If the work function of the analysis is  $\phi_{analyzer}$ , the kinetic energy of the electron in the analyzer is given by

$$E_{analyzer}^k = h\nu - E_b - \phi_{analyzer} \quad (2.74)$$

ARPES is a technique which directly measures electronic structure of solid surfaces and of bulk solids. By measuring the kinetic energy and angular distribution of the photoelectrons that emitted from a sample illuminated with sufficiently-high-energy photons, the electronic states as a function of both the energy and momentum inside a material can be revealed. The spectrum of the photoelectrons as a function of energy is called energy distribution curve (EDC), representing the density of electronic ground states (DOS). Furthermore, the photoelectron

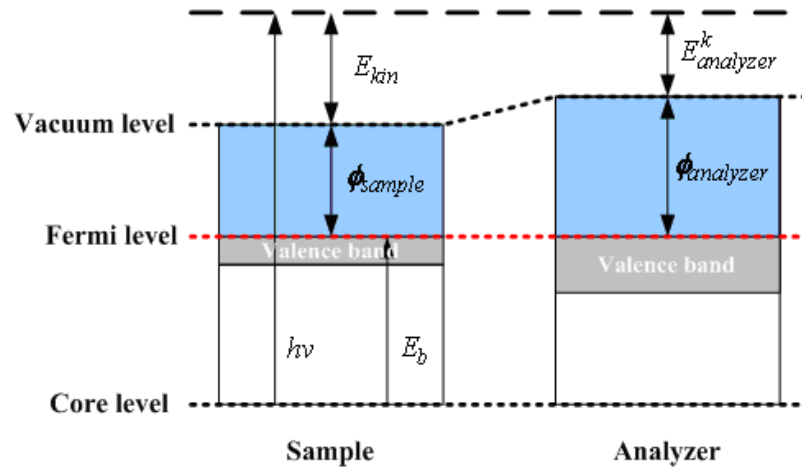


**Figure 2.10** Schematic diagram of the sample-analyzer work function in a photoemission system.

mean free path moving in solid materials is fairly short. Because the escaping depth depends on the kinetic energy of the photoelectron, this means that the photoemission technique can be very surface sensitive.

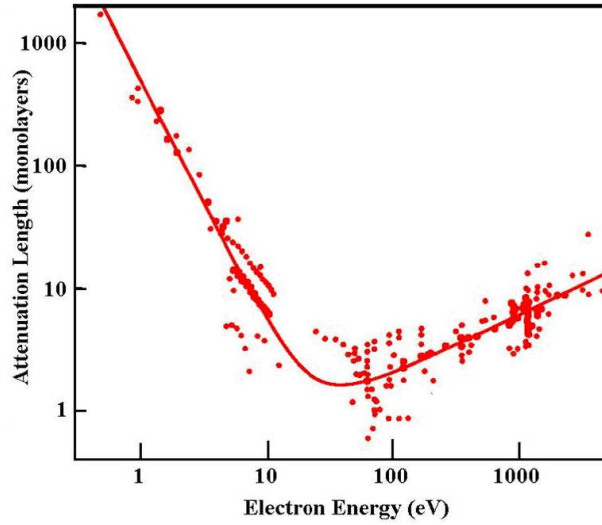


**Figure 2.11** Universal curve of electron mean free path (Briggs and Seah, 1990).

## 2.4.2 X-ray photoelectron spectroscopy (XPS)

“X-ray” in the term XPS refers energy range of incident photons. In conventional UPS (UV Photoelectron Spectroscopy), helium discharge lamp is usually used as a light source which emits He I and He II radiation of energy 21.2 eV and 42.4 eV, respectively. The atoms absorbing the UV photons are ionized and then emit electrons from valence levels. Similarly in conventional XPS, X-ray tube is usually used as a source. The most commonly used X-ray sources are Al and Mg anode tubes emitting Al  $K_{\alpha}$  and Mg  $K_{\alpha}$  characteristic radiation at 1487 eV and 1254 eV, respectively. However, in contrast, the atoms absorbing the X-ray photons are ionized and then emit electrons from core levels. The binding energies of photoelectrons can be written as the following equation:

$$E_{binding} = E_{photon} - E_{kinetic} - \Phi \quad (2.75)$$

where  $E_{binding}$  is the binding energy of the electron,  $E_{photon}$  is the incident-photon energy,  $E_{kinetic}$  is the kinetic energy of the emitted electron measured by the in-

strument and  $\Phi$  is the work function of the spectrometer.

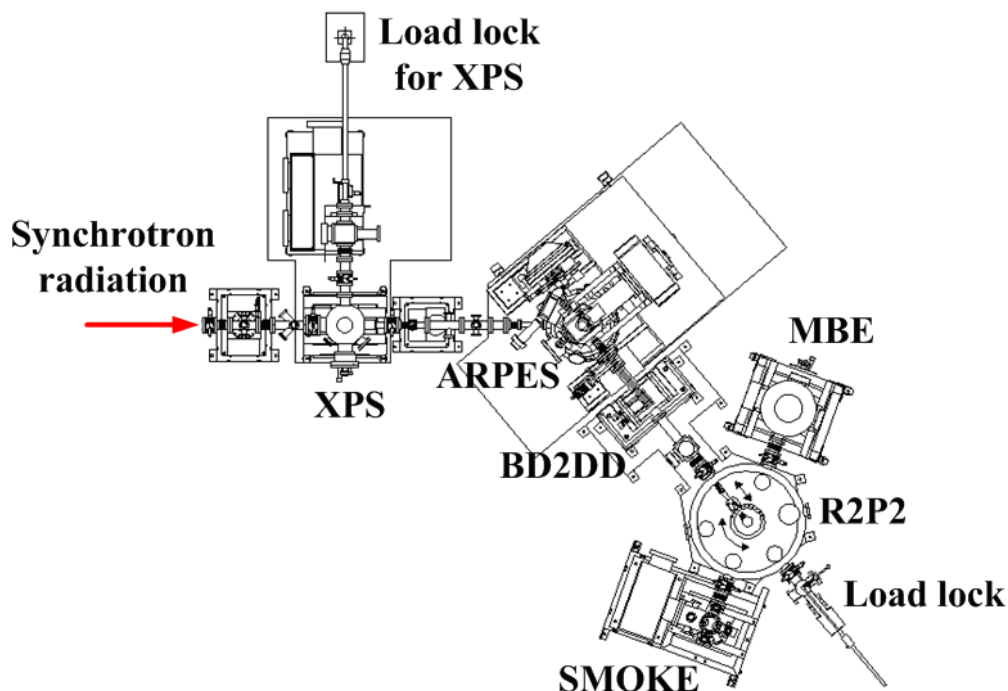


**Figure 2.12** The layout of the end station of ARPES with in situ system.

The BL3.2a beamline is designed for PES using synchrotron light in the energy range between UV and X-ray while UV discharge lamp can also be used as an additional light source. The PES system consists of two main chambers: 1) analysis and 2) preparation chambers. The system is connected to the molecular beam epitaxy system (MBE) and surface-magneto-optic-Kerr-effect system (SMOKE) with a load lock chamber and a R2P2 radial transporter, as shown in figure 2.12. In addition, a separated X-ray photo spectroscopy (XPS) is located in front of the PES which is used mainly for chemical analysis.

The load lock chamber is used to load samples. The load lock chamber is equipped with a turbo-molecular pump (TMP) and a scroll pump. The pressure in the load lock chamber is about  $10^{-7}$  Torr. Samples can then be moved to the R2P2 radial transporter by a magnetic coupling linear transfer and moved again

by a BD2DD sample transporter to the analysis chamber. A grabbler can be used to hold samples from the BD2DD sample transporter and to insert the samples into the sample holder on the manipulator of the analysis chamber.

The sample preparation chamber is mounted on the top of analysis chamber, as shown in figure 2.13. The vacuum between the preparation and analysis chamber can be separated by the UHV gate valve in the middle. The long manipulator is mounted on top of the preparation chamber. The sample preparation chamber has a 3 kV ion gun, a mini electron beam heater and an ion sputtering gun. The base pressures of the preparation and analysis chamber after baking are approximately  $2 \times 10^{-10}$  and  $1 \times 10^{-10}$  Torr, respectively.

The analysis chamber is equipped with a LEED, an ARUP10 energy analyzer and an ALPHA 110 hemispherical analyzer (Thermal VG Scientific), a UV discharged lamp and a 5 kV electron gun. The LEED is used for determining surface crystal structures of samples. The chamber is also equipped with a surface sensitive AES.

#### **2.4.2.1 Electron Energy analyzer**

An electron spectrometer or an electrostatic electron analyzer has been developed for measuring electron energy spectra of the surface analysis techniques. It is constructed for operating in UHV. In the case of the electrostatic electron analyzer, there are some different configurations, for measuring photoelectron; a concentric hemispherical analyzer (CHA) has been proven to be the most suitable. The best energy resolution of an electrostatic electron analyzer has been developed in the range of sub meV (Liu et al., 2008)

The concentric hemispherical analyzer (CHA) consists of a retarded grid, a hemispherical deflector with entrance and exit slits, electrostatic lens and electron detector as a channeltron or a microchannel plate electron detector. The

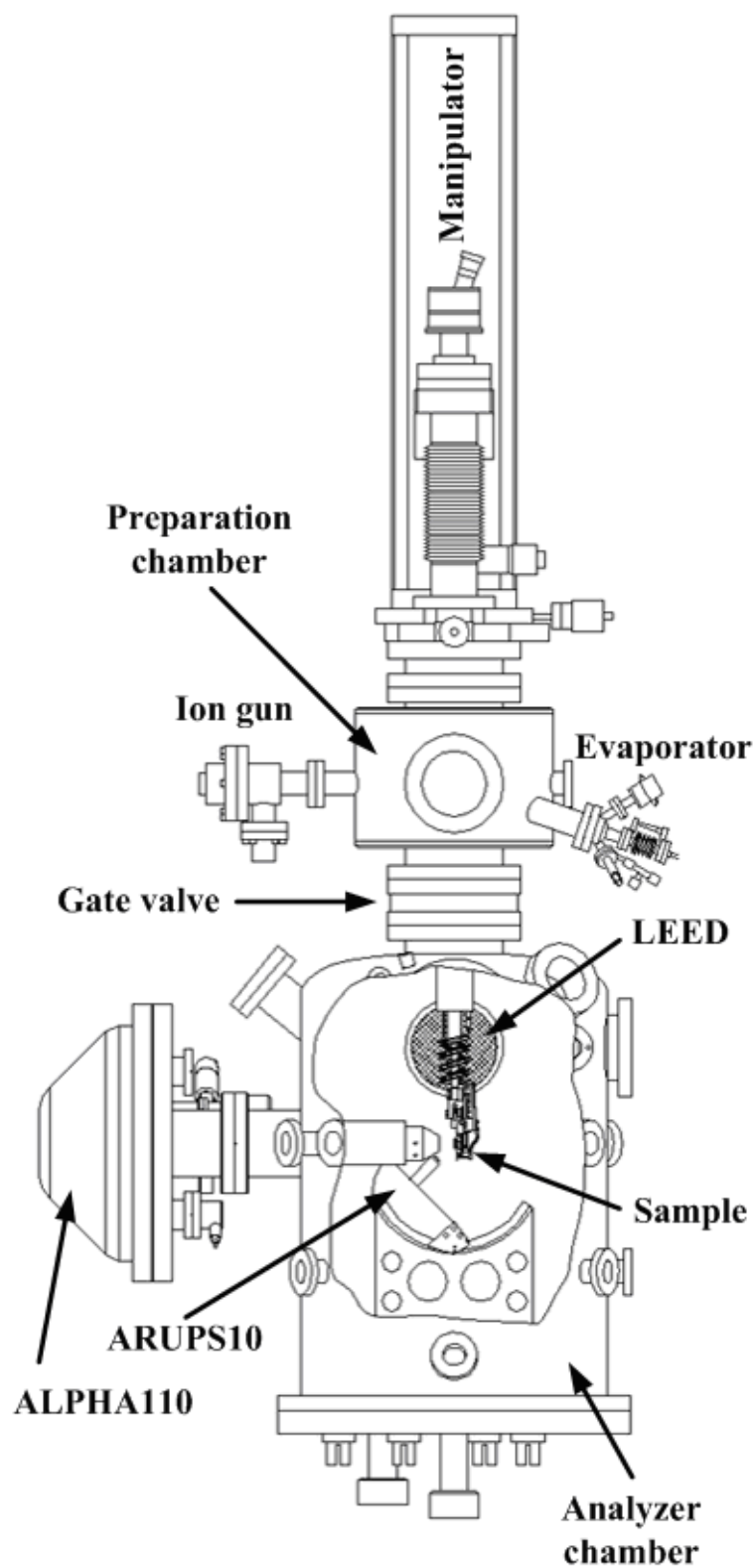
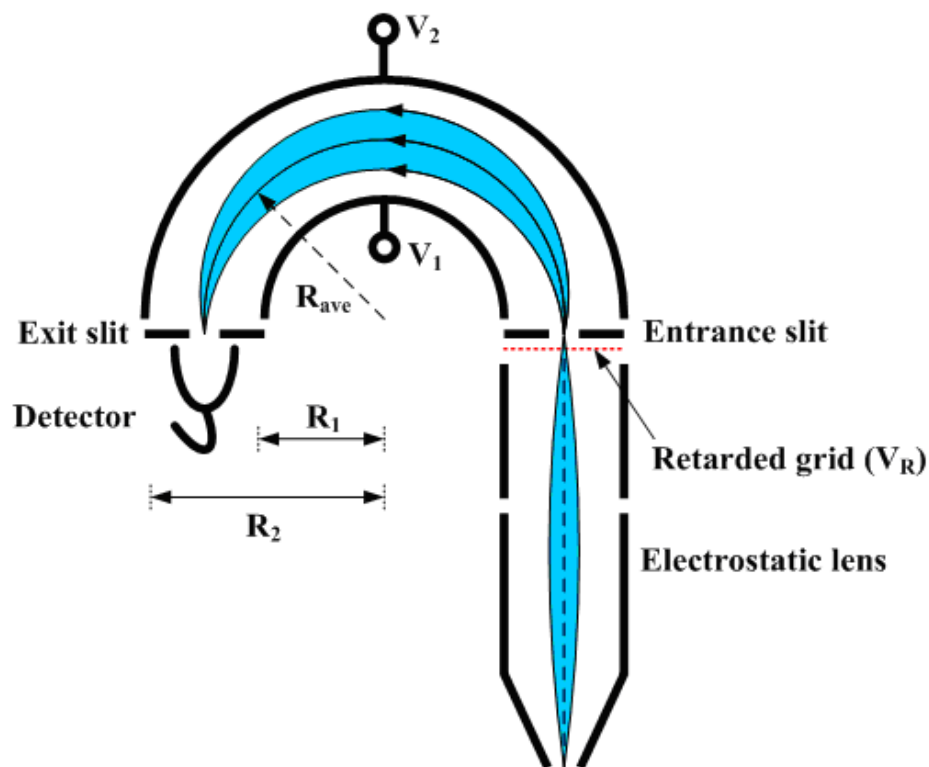


Figure 2.13 Diagram of the PES system at Beamline 3.2a.



**Figure 2.14** A cross section of the conventional concentric hemispherical analyzer (CHA).

hemispherical deflector consists of two concentric hemispherical electrodes with the inner and outer hemisphere of curvature  $R_1$  and  $R_2$ , respectively. The inner and outer hemisphere are applied with the voltages  $V_1$  and  $V_2$  while  $V_1$  is higher than  $V_2$ . In the case of CLAM2 analyzer, the voltages are applied for the inner and outer spherical sectors are the same in magnitude but opposite in polarity, i.e.  $V_1 = -V_2$ .

The voltage  $V(r)$  between the two hemispheres at radius  $r$  can be obtained by solving the spherical coordinates of the Laplace's equation (Kenneth, 1998).

The voltage is given by

$$\begin{aligned}
 V[r] &= V[R_{ave}] + 2k_R \left( \frac{R_{ave}}{r} - 1 \right) \cdot \Delta V \\
 k_R &= \frac{R_1 R_2}{R_2^2 - R_1^2} \\
 V[R_{ave}] &= k_R \cdot \Delta V
 \end{aligned} \tag{2.76}$$

where  $k_R$  is the analyzer constant,  $R_{ave}$  is the average radius,  $\Delta V$  is the voltage difference between the inner and outer hemispheres and  $V[R_{ave}]$  is the voltage along the center between the inner and outer hemisphere surfaces.

When the photoelectrons with specified kinetic energy in the range of so-called pass energy ( $E_p$ ) are focused by electrostatic lens and passed through the analyzer at the center of entrance slit with the normal angle, the photoelectrons will travel along the region between the inner and outer hemisphere surfaces and will pass through the exit slit. If the photoelectrons have kinetic energy out of range of  $E_p$ , they will get deviated to either the outer or inner spherical sector. The pass energy ( $E_p$ ) can be written as

$$E_p = e \cdot k_R \cdot \Delta V \tag{2.77}$$

where  $e$  is the charge of the electron.

Figure 2.15 shows the energies of photoelectrons when emitting from the conducting sample, accelerating and decelerating before passing through the entrance slit with retarded grid voltage,  $V_R$ . The photoelectrons with the kinetic energy as written in equation 2.78 can pass through the exit slit.

$$E_k^F = e \cdot V_R + E_p + W_A \tag{2.78}$$

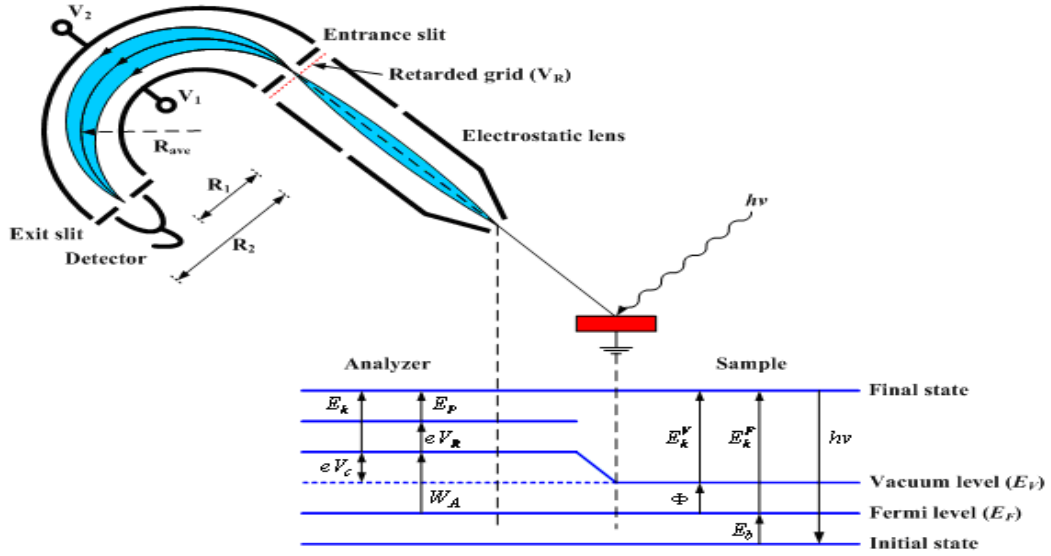


**Figure 2.15** The diagram shows energy levels at the conducting sample and the electron analyzer in a PES measurement.

where  $W_A$  is the work function of analyzer.

Normally, the energy analyzer has two mode can be operated. The constant analyzer energy (CAE) mode is used for UPS, XPS and PES which utilize synchrotron radiation. In this mode, the passing energy ( $E_p$ ) is fixed and the energy spectra are obtained by varying retarded voltage ( $V_R$ ). The energy resolution ( $\Delta E$ ) (Damascelli, 2004) is given by

$$\Delta E = E_p \left( \frac{d}{2R_{ave}} + \frac{\alpha^2}{4} \right) \quad (2.79)$$

where  $d$  is slit width and  $\alpha$  is the acceptance angle of the electron beam. The pass energy of the CAE mode of the CLAM2 spectrometer can be selected from the values of 0.1, 0.25, 0.5, 1, 2.5, 5 and 10 eV.

And the constant retard ratio (CRR) mode is used to measure the photoelectron for AES. In this mode, the pass energy ( $E_p$ ) is varied relative to the retarded voltage ( $V_R$ ) and the ratio between the passing energy and retarded

voltage is kept constant. The CRR constant is given by

$$CRR = \frac{E_k}{E_P} = \frac{V_R}{E_P} + 1 \quad (2.80)$$

This CCR constant of the CLAM2 spectrometer can be selected from the values of 1, 2, 4, 10, 20, 40 and 100.

The CLAM2 electrostatic electron energy analyzer is used in this work. It is installed in the XPS chamber.

### 2.4.3 Photoemission Electron Microscopy (PEEM)

PEEM using UV lamp has been developed since the early 1930s to study thin film and surface properties of various materials. However, PEEM results were not impressive. This was due to a lack of spectroscopy capability. Not until the year 1994, B.Tonner *et al* combined the synchrotron radiation spectroscopy with the full-field imaging of PEEM, which was later called X-PEEM. In X-PEEM, X-rays impinging on sample cause the emission of photoelectrons and secondary electrons. These electrons are accelerated by high voltage and focused to produce a magnified intermediate image by an objective lens. Then the series of the projection lenses are used to magnify the intermediate image further and form a final image on a CCD camera, as shown in figure 2.16.

#### 2.4.3.1 Contrast mechanism

Different contrast mechanisms in X-PEEM are shown in figure 2.17. In mode of magnetic contrast, the orientation of magnetic moments are probed by magnetic linear and circular dichroism effects. Topographical contrast is obtained from the distortion of the extraction field at surface topographical features. Elemental contrast is obtained by tuning the X-ray energy to characteristic absorption

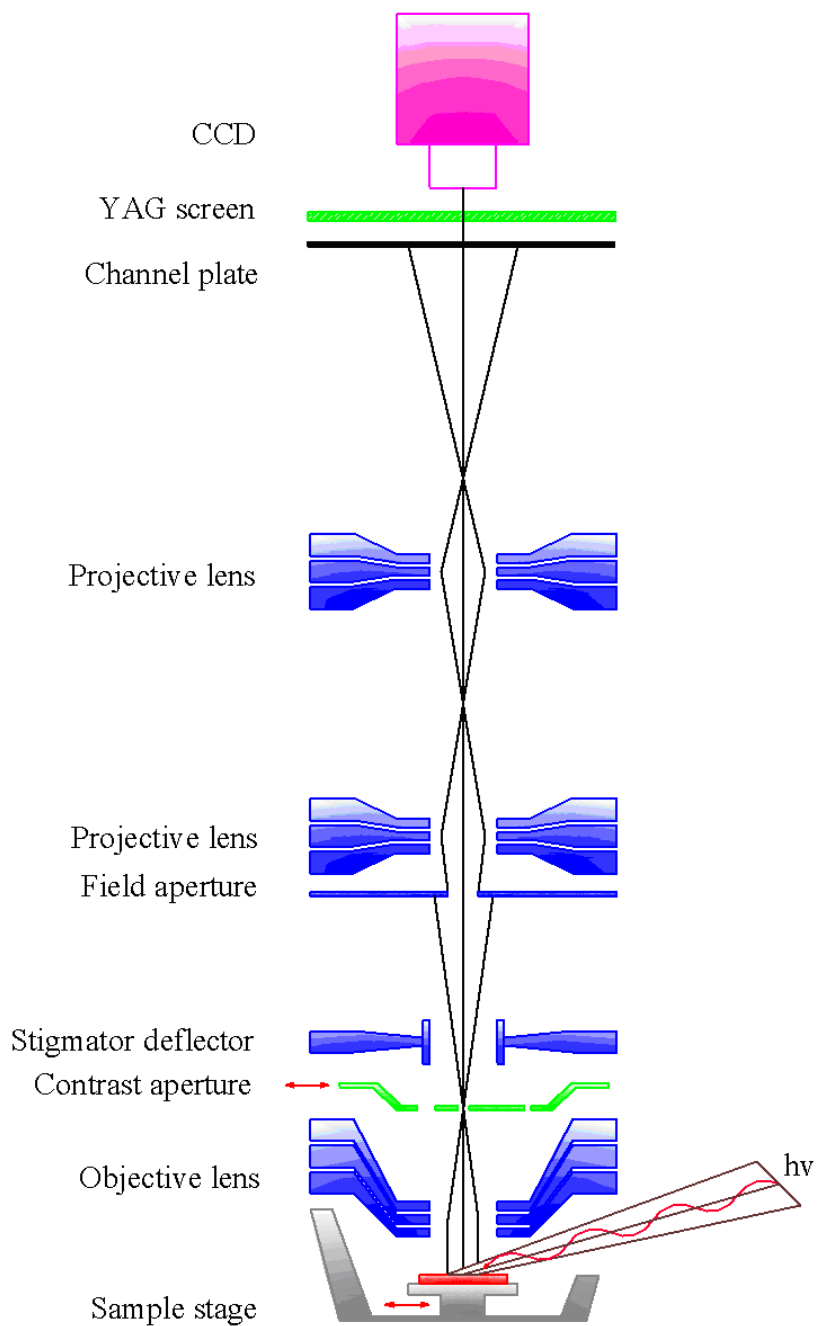


**Figure 2.16** schematic diagram of X-PEEM.

edges.

### Magnetic contrast

The circularly polarized X-rays are used to probe the angle ( $\theta$ ) between the

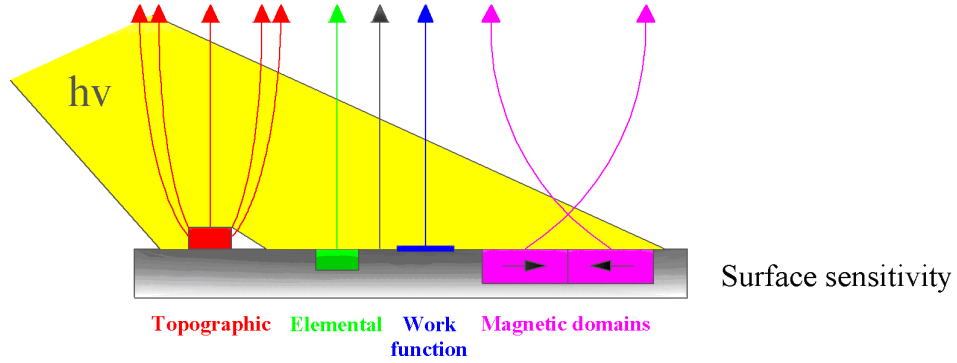


**Figure 2.17** Contrast mechanism of X-PEEM.

magnetization direction ( $M$ ) and the photon spin ( $\sigma$ ). This technique is called X-ray magnetic circular dichroism (XMCD) which is used for studying the magnetic moment of ferromagnetic materials. The XMCD intensity can be written as:

$$I_{XMCD} \sim |M| \cos\theta(M, \sigma) \quad (2.81)$$

The magnetic contrast image depends on the angle ( $\theta$ ). The maximum intensity can be observed when the direction of the photon spin and the magnetization are parallel or anti-parallel.

Another type of dichroism is the X-ray magnetic linear dichroism (XMLD) which is used for studying the antiferromagnetic materials. The XMLD is used for probing the angle ( $\theta$ ) between the antiferromagnetic axis ( $A$ ) and the vector of electric field ( $E$ ). The XMLD intensity can be written as:

$$I_{XMLD} \sim |M^2| [3\cos^2\theta(A, E) - 1] \quad (2.82)$$

The maximum intensity can be observed when the vector of electric field ( $E$ ) and the antiferromagnetic axis ( $A$ ) are parallel or perpendicular.

### **Topographic contrast**

Topographic contrast is a combination of primary and secondary contrast mechanisms. The primary contrast is caused by simple shading effects when the incident angle of radiation with respect to the surface normal is large. The topographic features can be “brightness-side” and “shadow-side” when the incident photon fluxes are high and low respectively. The secondary contrast is caused by deviations in electric field where the surface is rough. The deviations in electric field are called micro-fields and depending on the shape of the topographic features. The electric field lines are either spreaded out or concentrated when the observed electron intensity is low or high, respectively.

### **Work function contrast**

When the incident photon energy is chosen to be close to the work function of the sample, such as UV light, the intensity of photoelectrons can vary largely, depending on the small differences in work function. Thus the variation of the work function on the surface of the sample results in the variation of the intensity of photoelectron yield.

### **Elemental contrast**

In X-PEEM, elemental contrast is gained by tuning the X-ray energy close to the characteristic absorption edges of elements. Since the transitions satisfy the selection rule, at the absorption edges, X-ray absorption is increased because of strong resonance due to the transitions from the occupied states to unoccupied states. Furthermore, the intensity in the magnified image is proportional to the number of secondary electrons.

## 2.4.4 X-ray absorption spectroscopy (XAS)

X-ray absorption spectroscopy involves the excitation of core electrons to a continuum state. The absorption edge occurs only at certain energies of each element. The X-ray absorption spectrum can be separated into two regions: near edge and extended regions which are called X-ray absorption near-edge structure (XANES) and extended X-ray absorption fine structure (EXAFS), respectively. Information from analyzing spectra can be the chemical environment of the element (chemical shift), spin state, distance to the nearest neighbor and so on. In the conventional XAS, operation modes can be transmission, fluorescence yield and total electron yield.

### Transmission mode

In this mode, the intensity of incident X-ray ( $I_0$ ) and the intensity of transmitted X-ray ( $I$ ) are measured by using ionization chambers. The absorption coefficient ( $\mu$ ) can be written as.

$$\mu = \frac{1}{\rho d} \ln\left(\frac{I_0}{I}\right) \quad (2.83)$$

where  $\rho$  is the mass density and  $d$  is the sample thickness. The experimental setup for the transmission mode is relatively simple. However, there are disadvantages that the sample must be thin enough to allow incident X-ray to be transmitted, low surface sensitive and very homogenous.

### Fluorescence yield mode

Absorption of X-ray make electrons in atoms get to excited states. To return to the ground state, the atoms give out Auger electrons or fluorescent light through the non-radiation or radiation decay channel respectively. In radiation decay channel, the intensity of fluorescence is proportional to the number of core

hole created by the absorption process. Fluorescence has large penetration depth and hence XAS in the fluorescence yield mode is a bulk sensitive technique (surface sensitive may be obtain by a complicated grazing incident setup). In this mode, the advantage is that there is no limitation on the sample thickness. However, elements with core level(s) below 2 keV may be difficult to be measured due to low fluorescence yield. Also, it is very sensitive for a very dilute sample. However, it has some difficulties for dense samples due to the self absorption effect.

### **Total electron yield mode**

In this mode, the X-rays absorbed produce photoelectrons by excitation of core electrons to a continuum state. Auger electrons are also produced in the non-radiated channel. The photoelectron and Auger electrons inelastically scatter with other electrons in the sample causing secondary electrons which dominate the total electron yield (TEY) intensity which is written by

$$I_e = I_0 \mu d \quad (2.84)$$

where  $I_e$  is the total electron yield,  $I_0$  is the incident intensity,  $\mu$  is the absorption coefficient and  $d$  is the electron escaping depth. The tuneability of synchrotron light enhances the performance of X-PEEM, allowing XAS measurement to be possible. The XAS with X-PEEM collects and images secondary electrons that emit from a sample surface under photon irradiation, and then uses magnetic lenses column to magnify the field of view defined by the objective lens. By varying the photon energy, nano/micro X-ray absorption spectra can be extracted from a sequence of images. The advantage of the total electron yield mode is the ability to select probed depth. This mode provides both surface and bulk sensitivity.

The BL3 beamline is expected to deliver photons with energy between 40

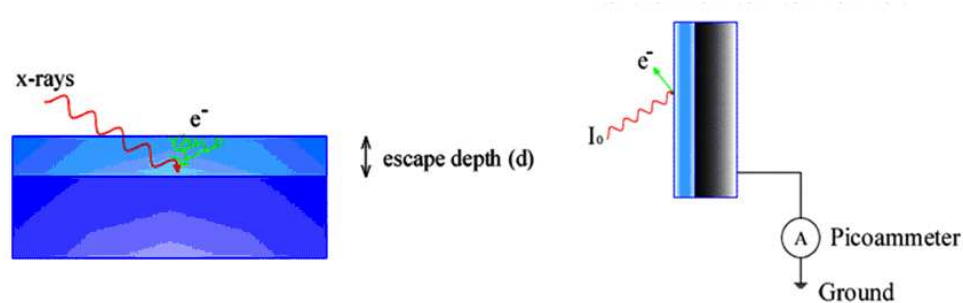


**Figure 2.18** The total electron yield mode of recording in XAS.

and 1040 eV. This photon energy range covers all K-edge of important elements in organic specimens (C, O, N), and L-edge of element from nitrogen atom through nickel atom. This energy range allows us to look into many interesting processes, e.g. chemical dynamics, polymers and catalysis.

BL3 has photons with energy in the range of 40–1040 eV. Thus XPS using synchrotron light can also be performed at BL3. Information from measured spectra can be about contamination, composition of a material, chemical state, the density of electronic states and *etc.* A combination of X-PEEM and imaging energy analyzer allows us to get images at a specified electron energy, called “imaging XPS.”

## 2.5 Beamline

Generally, a synchrotron-radiation beamline consists of four functional sections. The first section provides the synchrotron radiation source as bending or insertion device. The second section, which immediately connects to the port of bending magnet but is still inside a concrete shielding wall, is called the front-end. The main front-end components include of masks, a heat absorber (ABS), a bremsstrahlung shutter (BS), a photon beam position monitor (BPM) and vacuum gate valves.

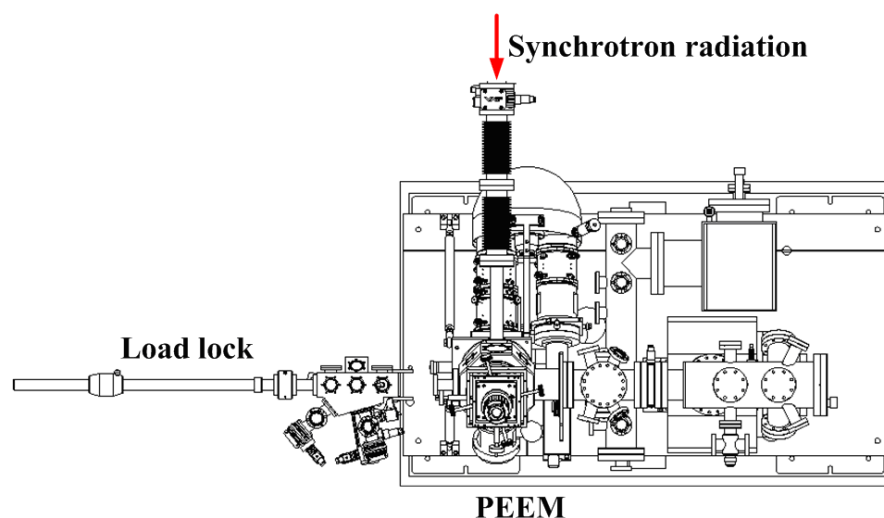


**Figure 2.19** The layout of the PEEM end station at Beamline 3.2b.

Mask is the first front-end component to interact with the synchrotron beam. This component allows a part of the synchrotron beam to go through downstream components and also protects the downstream components from thermal damage.

A heat absorber is a water-cooled photon shutter. Its function is to adjust the transmission of the synchrotron beam.

A bremsstrahlung shutter is used for providing radiation shielding. In the case of BL3, the heat absorber and the bremsstrahlung shutter are in one unit. This component completely intercepts the synchrotron beam via a fast-acting mechanism in order to isolate the downstream components and also acts as a safety device to protect the safety shutter from the direct synchrotron beam impingement. That is, this component must be first closed and last opened.

Beam position monitor is a tungsten wire system, in vertical and horizontal position. It is placed in the fringes of the synchrotron beam to detect the position of the synchrotron beam. When the tungsten wire is swept by the synchrotron beam, the photoelectrons are generated. This causes a microampere level photocurrent

that can be measured.

Vacuum gate valves are used for vacuum isolation of different sections in the front-end.

The design of the front-ends must also satisfy the beamline requirements. It means that the front-end are configured to meet the following requirements:

1. Ensure personal safety.
2. Maintain the storage ring vacuum integrity.
3. Collimate the photon beam. And the photon beam cannot hit unprotected vacuum parts which do not have a cooling unit
4. Withstand the full power of the photon beam and bremsstrahlung during beam injection in the case of vacuum failure.

The third section has the first optical element as the pre-focusing mirror, which contains optical elements to monochromatize the photon beam. The fourth section is the experiment stations where actual scientific measurements are performed.

### **2.5.1 Photon-energy scanning mechanism**

To change the incidence and diffraction angles of the grating, it can be done by rotating the grating until that the desired photon energy is obtained. The grating can be rotated by a sine-bar. This sine-bar is driven by a DC stepping motor which is controlled by an in-house Labview program. A linear encoder is necessary to guarantee the reproducibility of the linear movement of the photon energy scanning mechanism. The ND281B Heidenhain linear encoder scale is used for high accuracy linear motion with the resolution of 0.01 micrometer. The three

VLSPGs are installed on the rotation plate. The grating rotation diagram is shown in figure 2.20.

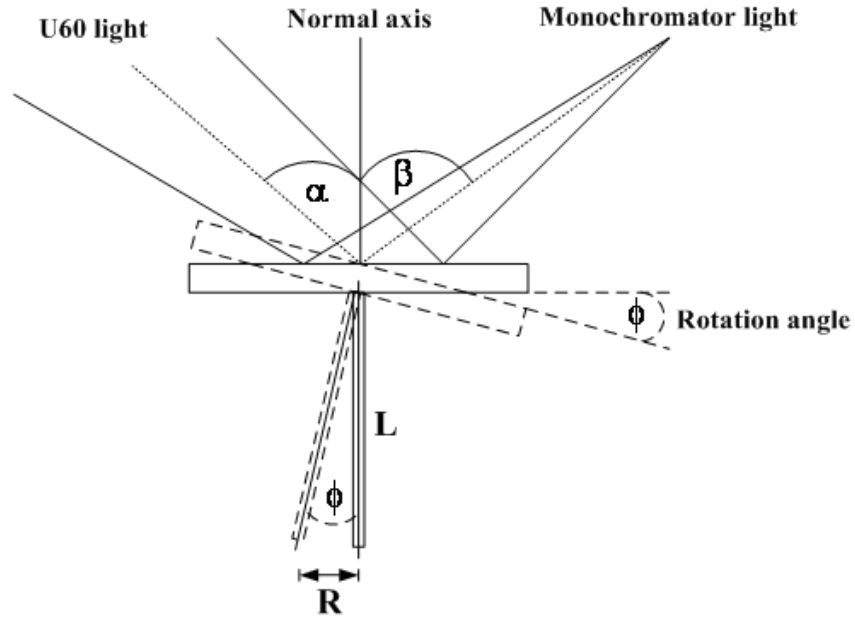


**Figure 2.20** The sine-bar for the grating rotation of the BL3 beamline.

(The grating equation for a constant included angle monochromator is given by)

$$2 \sin \phi \cos \theta = Nk\lambda \quad (2.85)$$

where  $\theta = \frac{\alpha - \beta}{2}$  is the deviation angle and  $\phi = \frac{\alpha + \beta}{2}$  is the rotation angle. These values relate to the normal axis of the surface of the grating or the included angle, for the BL3 beamline. The VLSPG monochromator is operated in the constant included angle geometry with an included angle of  $167.5^\circ$  and  $172.5^\circ$  for the low and high photon energy ranges, respectively. In the case of zero order light,  $\theta$  is the incidence and reflection angles:  $83.75^\circ$  and  $86.25^\circ$  for the low and high photon

energy ranges, respectively.

The grating rotation is moved by a linear motion as shown in figure 2.27, the relationship between the linear displacement ( $R$ ) and the rotating angle ( $\phi$ ) is written by

$$R = L \sin \phi \quad (2.86)$$

where  $L$  is the length of the sine-bar. The relationship between the linear displacement and the photon wavelength can be solved by substituting equation 2.86 into equation 2.85 as the following:

$$\lambda = \left( \frac{2 \cos \theta}{LNk} \right) \cdot R \quad (2.87)$$

Thus, the relationship between the linear displacement and the photon energy can be written as:

$$E[eV] = \left( \frac{hcLNk}{2 \cos \theta} \right) \cdot \frac{1}{R[mm]} \quad (2.88)$$

where  $h$  is the plank's constant,  $c$  is the speed of the light and  $k$  is the diffraction order.

## 2.5.2 Photodiode detector

The photodiode, which is developed by International Radiation Detectors Inc (IRD), has been used at the BL3 beamline. The photodiode is a silicon p-n junction but it is unlike common p-n junction diodes. The AXUV series photodiodes do not have a doped dead-region in the front and have zero surface recombination resulting in near theoretical quantum efficiencies (R. Korde, 1987).

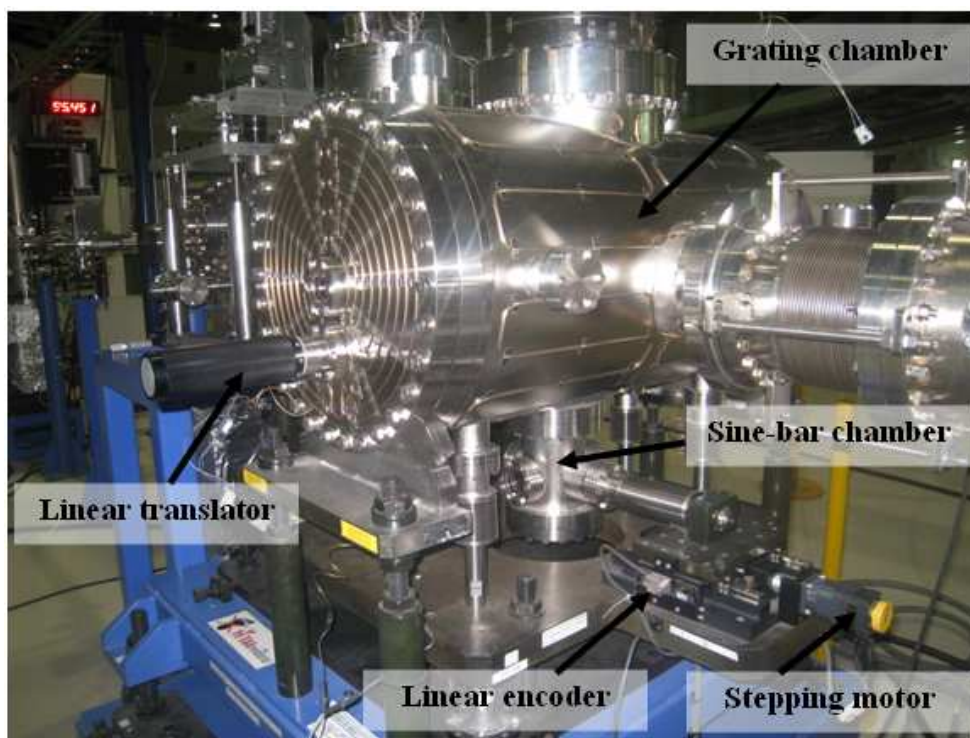


**Figure 2.21** The picture of the grating chamber. The grating is rotated by a sine-bar which is driven by a DC stepping motor. The linear encoder is installed outside the chamber.

These series photodiodes can be operated in air, in gas ambient like helium, argon, nitrogen, and under vacuum below than  $10^{-10}$  Torr. The operation temperature is in the range of  $-200^{\circ}\text{C}$  to  $70^{\circ}\text{C}$  and it can be baked up to  $200^{\circ}\text{C}$  in the vacuum. To avoid the contribution of the photoemission current to the photogenerated current, the signal is connected the p-region and n-region as anode and cathode or ground of the diode, respectively. The model AXUV100A12, which has the specifications of 40 nanometer filter thickness and the band pass 17 - 80 in the range of nanometers, is used at the BL3 beamline.

### 2.5.2.1 Quantum efficiency

The electron-hole pairs (the carrier) are created when the silicon photodiode is exposed by photons with energy higher than 1.12 eV or the wavelength less than 1100 nm. These carriers are separated by the p-n junction electric field. And a

current proportional to the quantity of the electron-hole pairs are created to flow through an external circuit. The photon energy in the range of VUV, with the wavelength shorter than 350 nm (R. Korde, 1987), will create more than one electron-hole pair.

The AXUV photodiode has no surface dead region. This means that no carrier recombination can occur in the n-type doped region and at the silicon dioxide interface. The AXUV photodiode also has a very thin, radiation-hard, silicon dioxide passive junction, protective entrance window. This word is so long. Please break it into shorter sentences. Figure 2.22 shows the quantum efficiency spectrum of AXUV100Al2 model.

The photocurrent can be written as

$$I = \frac{d(ne)}{dt} = e \frac{dn}{dt} \quad (2.89)$$

And the quantum efficiency ( $QE$ ) can be written as:

$$QE = \frac{dn/dt}{Flux[phs/s]} \quad (2.90)$$

Substituting  $\frac{dn}{dt}$  in the equation 2.89 to the equation 2.90, the photon flux in the unit of photons per second can be written as a function of the photo current in the unit of ampere from the photodiode as the following:

$$Flux[phs/s] = \frac{I[Amp]}{e \cdot QE} \quad (2.91)$$

Where  $e$  is a charge of the electron and  $I$  is the photo current.

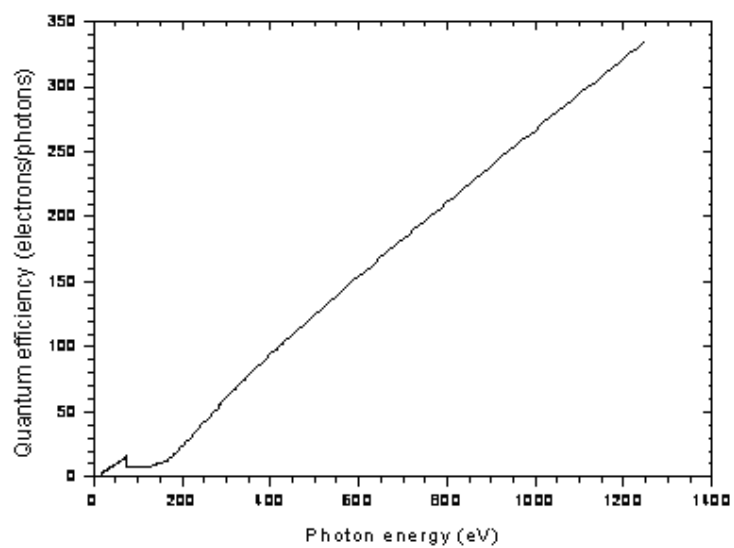


**Figure 2.22** The quantum efficiency of the AXUV100A12 photodiode corresponding to the photon energy.

# CHAPTER III

## DESIGN CONSIDERATIONS

This chapter will be explained the conditions of beamline design of the BL3 beamline. The typical requirements for designing beamline are available photon energy range, beam sizes, flux, resolution or resolving power. The BL3 beamline design consideration should satisfy the following requirements

1. Length of the beamline is limited by the wall of the experimental hall as show in figure 3.1. The new wall of the experimental hall that close to the BL3 is longer than the old wall about 12 meters. That means the length of the BL3 beamline can be designed longer than the BL4 beamline which is possible to design the micro- beam. The source of the BL3 beamline is an undulator which has a small photon source size that can be de-magnified as a micro-beam corresponding to a field of view of the PEEM image.
2. The source of the BL3 is a planar Hallback type undulator (U60), which has 41 periods and a period length of 60 mm as shown in figure 3.2, placed in the 1<sup>st</sup> straight section of the SPS storage ring. The minimum photon energy of  $\tilde{40}\text{eV}$  is limited by the minimum undulator gap of 26.5 mm, corresponding to an effective deflection parameter K of 3.0631 and the peak magnetic field of 0.5467 Tesla. The electron beam size and the emittance at the middle of U60 are the followings:  $\sigma_x = 1.218$  mm,  $\sigma_y = 0.05$  mm,  $\varepsilon_x = 95.51$  nm·rad and  $\varepsilon_y = 0.3015$  nm·rad. Main parameters of the undulator are shown in table 3.1. The undulator has been designed for the energy range of 1<sup>st</sup> to 7<sup>th</sup> harmonics. The storage ring is planned to operate at a current 150 mA.

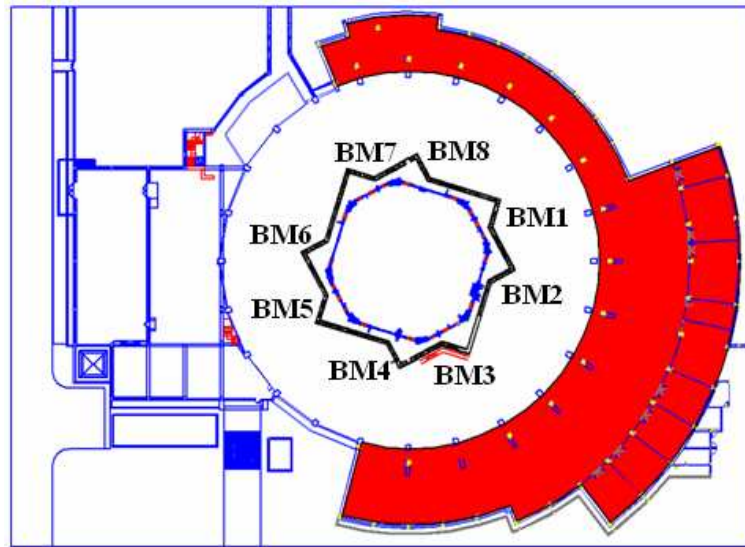


**Figure 3.1** The experimental hall layout (shade area is the new extension area).



**Figure 3.2** U60, the first undulator to be installed at the Siam Photon Laboratory.

3. Photon source sizes and divergences of the undulator source are mainly limited by the sizes and divergences of the electron beam circulating in the storage ring. The photon source size and divergence for the photon energy

**Table 3.1** Parameters for the Undulator (U60) of the SPS.

Parameters	Data
Configuration	Pure Permanent Magnet (PPM) symmetric
Magnet material	VACODUM
Period length ( $\lambda_u$ )	60 mm
Minimum & maximum gap	26 & $\geq 200$ mm
Operated minimum & maximum gap	26.5 & 100 mm
Total length of magnetic assemblies ( $L$ )	2510 mm
Number of full size poles	81
Number of periods ( $N$ )	41
Peak magnetic field ( $B_0$ )	0.54674 T
Peak magnetic field strength ( $K$ )	3.06306
Minimum photon energy	$\sim 40$ eV
(Gap 26.5 mm, Electron beam 1.2 GeV)	

40 eV are shown in figure 3.3 and 3.4, respectively. The situation is even worst when 1) a large source size or/and 2) high demagnification is/are the condition(s). This is the case for the optical system of the BL3 PEEM-branchline at the Siam Photon Laboratory. The horizontal source size of the BL3 is very large,  $\sim 2.8$  mm FWHM as shown in figure 3.3. The beam size on the sample for PEEM is required to be less than or equal to the maximum field-of-view of PEEM,  $< 150$  micron. Thus, a large demagnification is required to make a small beam spot on the sample. The horizontal photon source size is also constant in the energy range of interest, except for the vertical photon source size and both direction of divergences as shown in figure 3.5 and 3.6, respectively.

**Table 3.2** Parameters for the photon source size and divergences of the undulator of the SPS.

Parameters	Data
RMS photon source size (H $\times$ V) [ $\mu m$ ]	1219 $\times$ 45 - 33
RMS photon source divergence (H $\times$ V) [mrad]	113 - 83 $\times$ 80 - 23

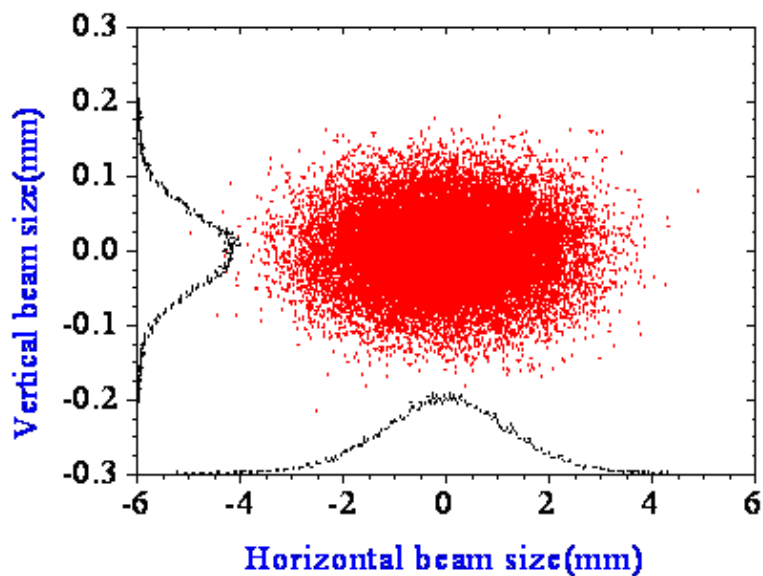


**Figure 3.3** Image of the photon source size of 60 mm period undulator for photon energy 40 eV.

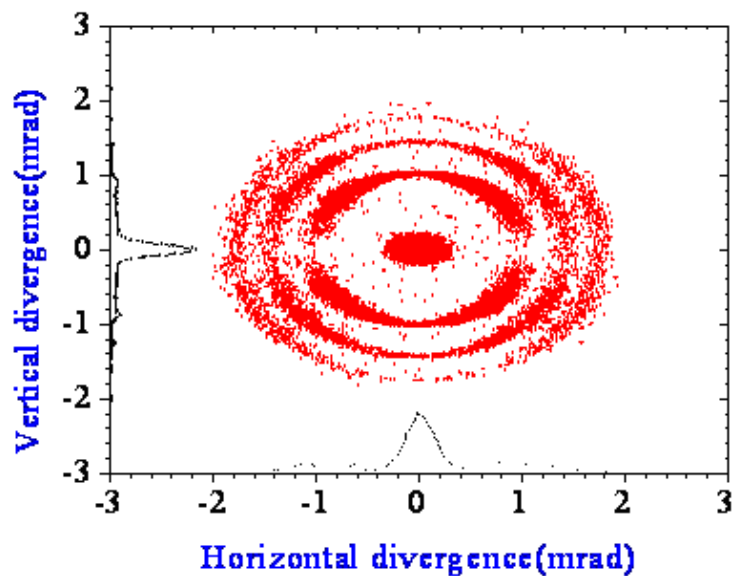


**Figure 3.4** Image of the photon source divergence of 60 mm period undulator for photon energy 40 eV.

4. The photon flux of the U60 undulator shows in the first till a seventh harmonics at the SPS. The U60 undulator light covers an energy range of 40–207

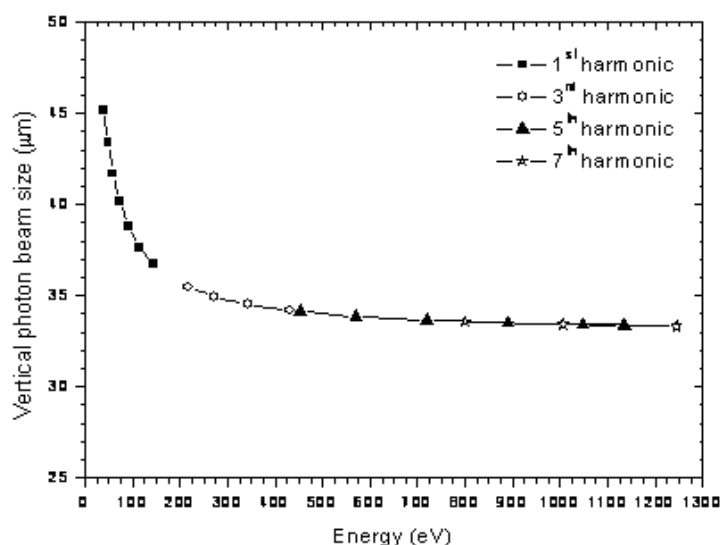


**Figure 3.5** The vertical photon source size in the energy range of interest.

eV in the first harmonics corresponding to the undulator gap of 26.5 to 100 millimeters. But the beamline is designed to deliver a photon energy of the first harmonic of the U60 undulator in the range of 40 to 160 eV. Moreover, the third till the seventh harmonics, the undulator light covers up to 1.2 keV of X-ray energy. The U60 undulator flux simulation with an opening angle of 0.2 mrad and 1 mrad in the vertical and horizontal directions, respectively shows the maximum photon flux is  $10^{14}$  photons/second/0.1% band width, as shown in Figure 3.7.

So, flux at a sample position should be higher than  $10^9$  photons per second for all energies range.

5. The resolving power of the all gratings is designed at 10000.
6. The vertical beam focused by the pre-focusing mirror will be focused at the entrance slit and the focused image is a virtual source of the monochromator section. Then this virtual source is used for mirrors in the monochromator

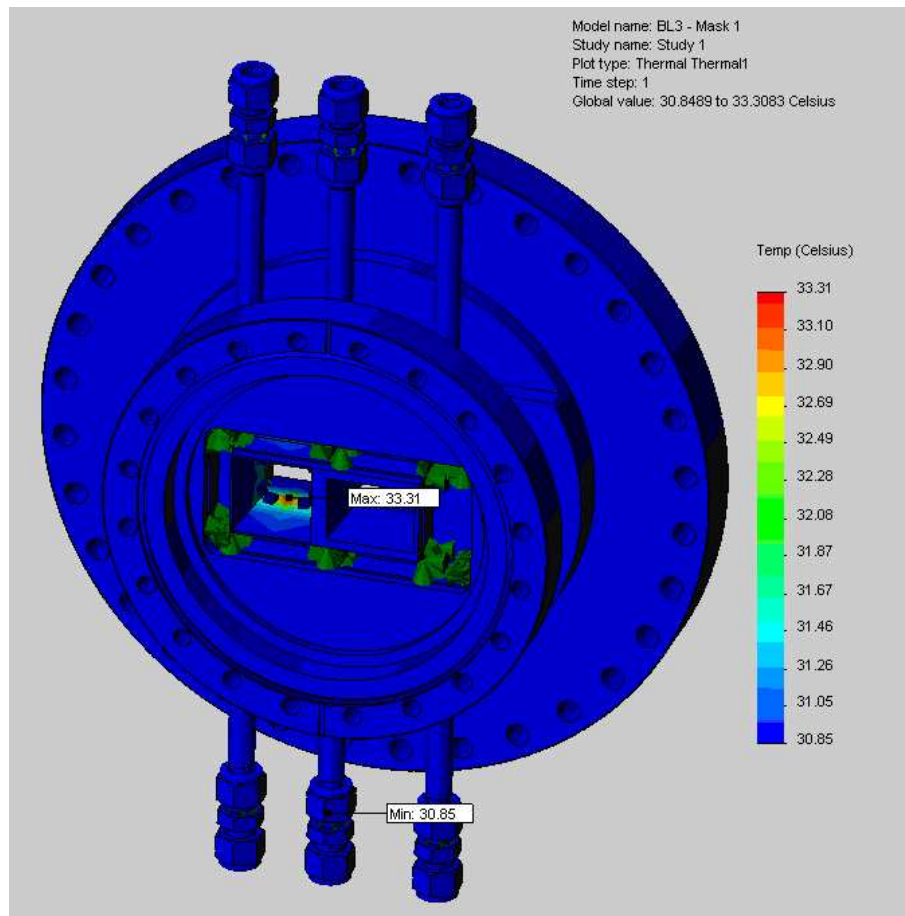


**Figure 3.6** The divergences of the photon source in the energy range of interest.

section and focused at the exit slit. Furthermore, the advantage of this design will be used to check the location of the vertical focused at the slits.

- The power delivered by the undulator depends on the peak photon energy of the undulator, as shown in figure 3.8. And this is chosen by changing the undulator gap that thus the magnetic field strength parameter ( $K$ ). At minimum gap of the undulator at 26.5 mm, the maximum total power is 67 W when the electron current in the storage ring is 100 mA. The power distribution is a Gaussian approximation, with a maximum power density of 50 W/mrad<sup>2</sup>, as shown in Figure 3.9.

Thus, part of radiation power is absorbed by the front-end slits. The opening

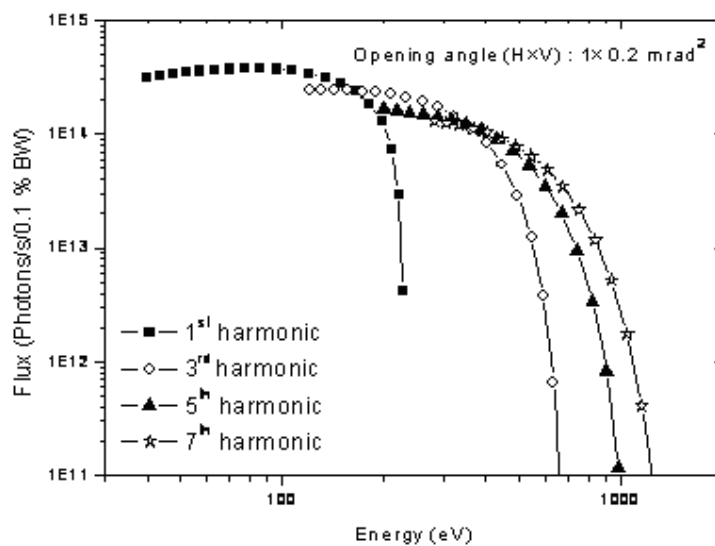


**Figure 3.7** Shows the calculated photon flux of 60 mm period undulator. Current in SPS storage ring is assumed to be 100 mA.

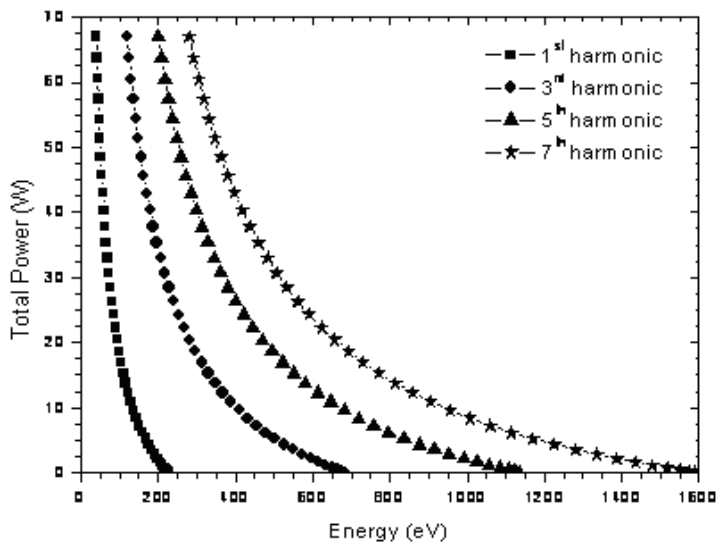


**Figure 3.8** The power delivered by the undulator in function of the peak energy. Current in the storage ring is 100 mA.

angle aperture of the front-end slits is  $\pm 0.1$  mrad and  $\pm 0.5$  mrad in the vertical and horizontal directions, respectively corresponding to the front-

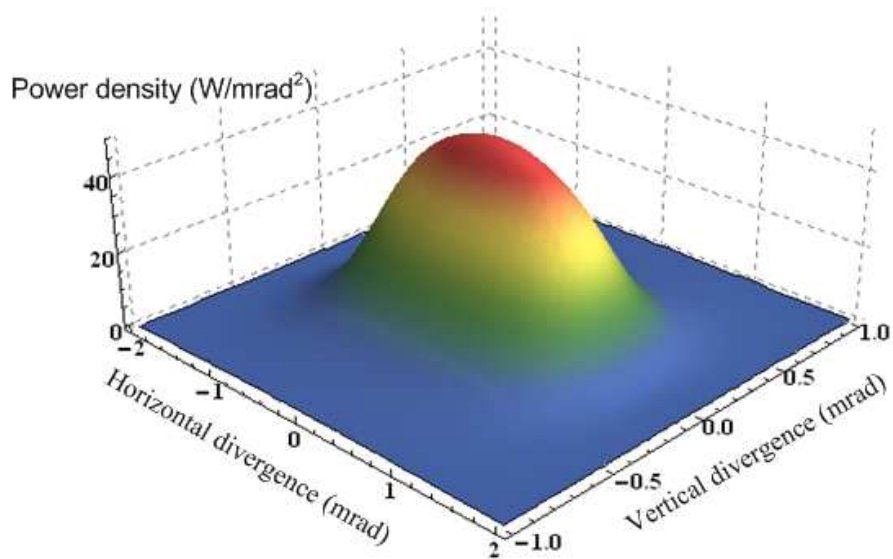


**Figure 3.9** Angular power density delivered by the U60 undulator with current in the storage ring 100 mA.

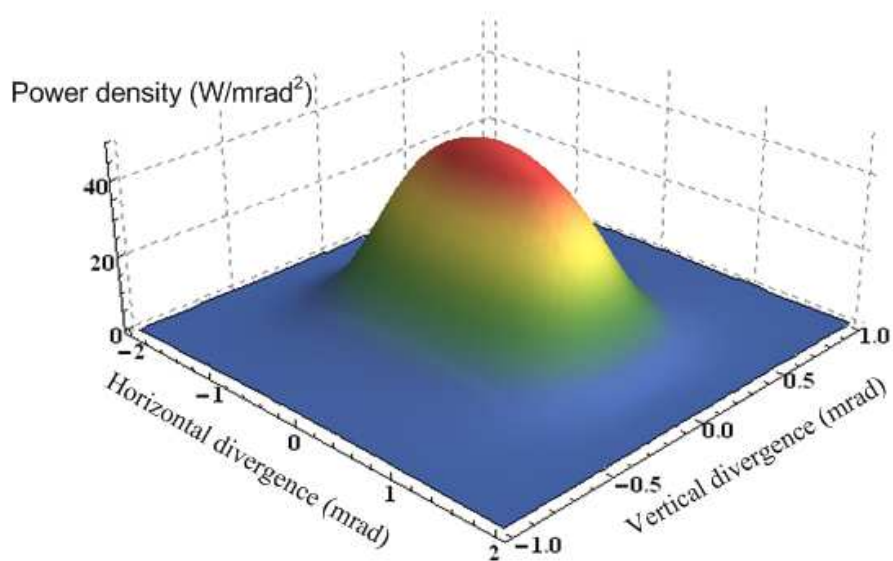


**Figure 3.10** Angular power density delivered by the U60 undulator with current in the storage ring 100 mA.

end slit width of 1.4 mm and 11 mm at 6 meters from the undulator source position. This limited opening angle reduces to 24 W the maximum power incoming to the beamline optics, the front-end slits absorbing 43 W with a

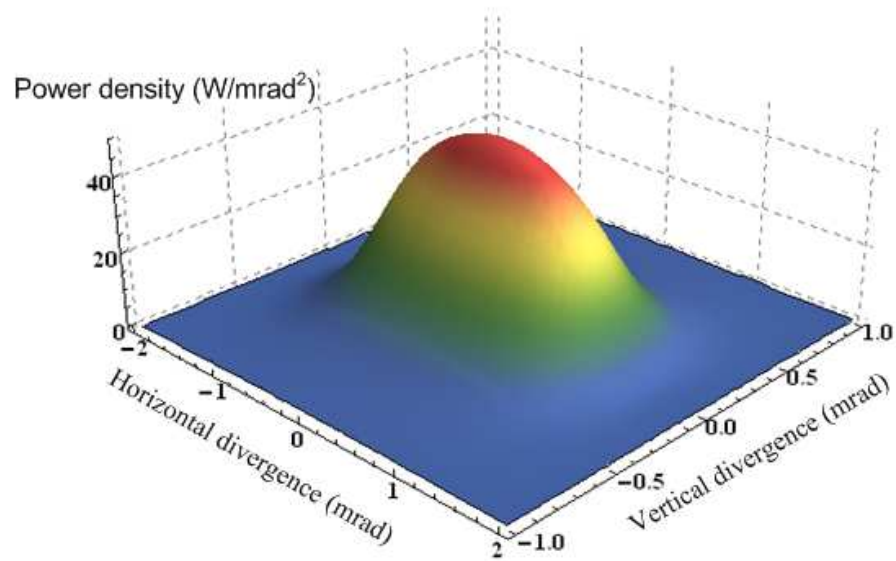


**Figure 3.11** Angular power density delivered by the U60 undulator with current in the storage ring 100 mA.

current of 100 mA in the storage ring.

8. The base pressure of the BL3 beamline should be lower than  $5 \times 10^{-10}$  Torr or in the range of the UHV are required:
  - PEEM and PES are the surface techniques.
  - To protect contamination of the optical surfaces.
  - To be consistent with the storage ring vacuum.
9. Existing mechanical parts from BL4 will be used as many as possible. So the size of the new mirrors should be fitted to the old mirror holders. Furthermore, the cost of the beamline will be reduced.

# CHAPTER IV

## OPTICAL DESIGN AND RESULTS

This chapter explains the optical design of BL3, the first undulator beamline at the Siam Photon Laboratory, and the simulation software used for ray tracing. The beamline is designed to deliver photons generated by a planar Hall-back type undulator (U60) to the end station for PEEM and ARPES experiments in time-sharing mode. The undulator has 41 periods and a period length of 60 mm, placing in the 1<sup>st</sup> straight section of the SPS storage ring. The optics is designed considering characteristics of the undulator source such as the source size, divergence, flux and power. The focal length of pre-focusing mirror which is the most important element of the beamline optics is simulated by ray-tracing method using SHADOW VUI. The simulation shows that the focal length agrees well with calculations in the vertical direction, but differs significantly in the horizontal direction. The effects on the horizontal beam size from the specification of the undulator source as well as the figure of the pre-focusing mirror are provided in this chapter. Next, the varied-line-space plane grating (VLSPG) with aberration correction is explained. Finally, post-focusing mirror optimization for PEEM and ARPES experiments is discussed.

### 4.1 Optical layout

The BL3 optical layout is consisted of a pre-focusing system, a monochromator system and two post-focusing systems, as illustrated in figure 4.1. The design employs a varied-line-spacing plane-grating monochromator which covers

photon energy between 40-160 eV, and 220-1040 eV. The monochromator has two branchlines (post-focusing systems) downstream for PEEM and PES experimental stations, operating in a time-sharing mode. The post-focusing system for PEEM branchline employs two cylindrical mirrors (M2V and M2H) arranging in the K-B configuration to suppress optical aberrations. Due to the space limitation of the experimental hall and cost considerations, a toroidal mirror is used as a pre-focusing mirror (M0).

**Table 4.1** Summary of the BL3 optical elements descriptions.

Optical element	Distance from source (mm)	Description
M0 (Toriodal mirror)	8940	Pre-focusing mirror
Entrance slit (S1)	13410	Optimize beamline resolution
M1/1 (Spherical mirror)	17910	Use for high photon energy (172.5 deviation angle)
M1/2 (Spherical mirror)	18576.12	Use for low photon energy (167.5 deviation angle)
VLSPGs	1897.22	Select the energy G1 : Eph 40–160 eV G2 : Eph 220–520 eV G3 : Eph 440–1040 eV
Exit slit (S2)	22410	Optimize beamline resolution
M2Cy (Cylindrical mirror)	23510	Deflect beam to ARPES branch
M2T (Toriodal mirror)	29560	Post-focusing mirror for ARPES branch.
M2V (Cylindrical mirror)	25645	Post-focusing mirrors for PEEM branch arranging in
M2H (Cylindrical mirror)	26145	the KB configuration

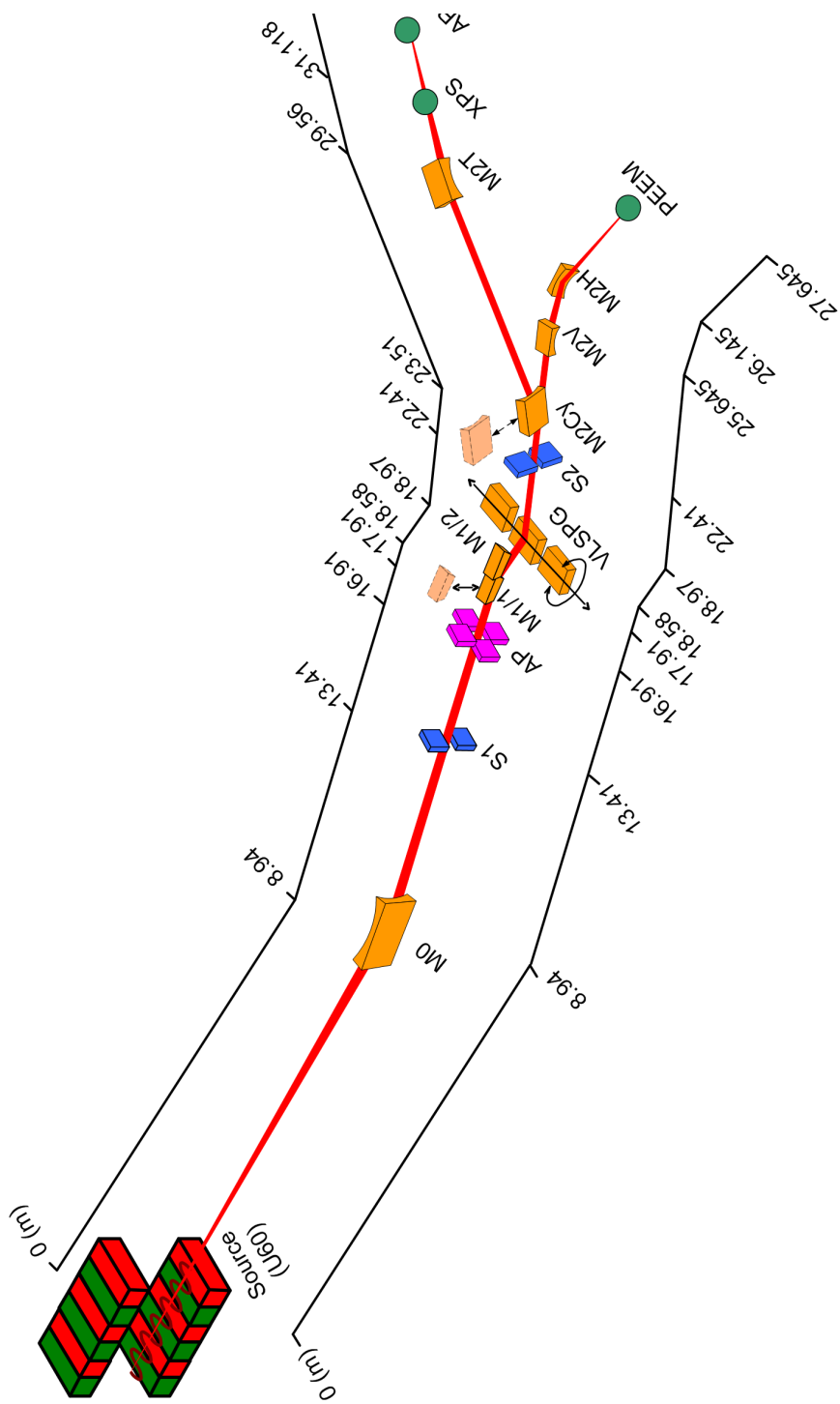
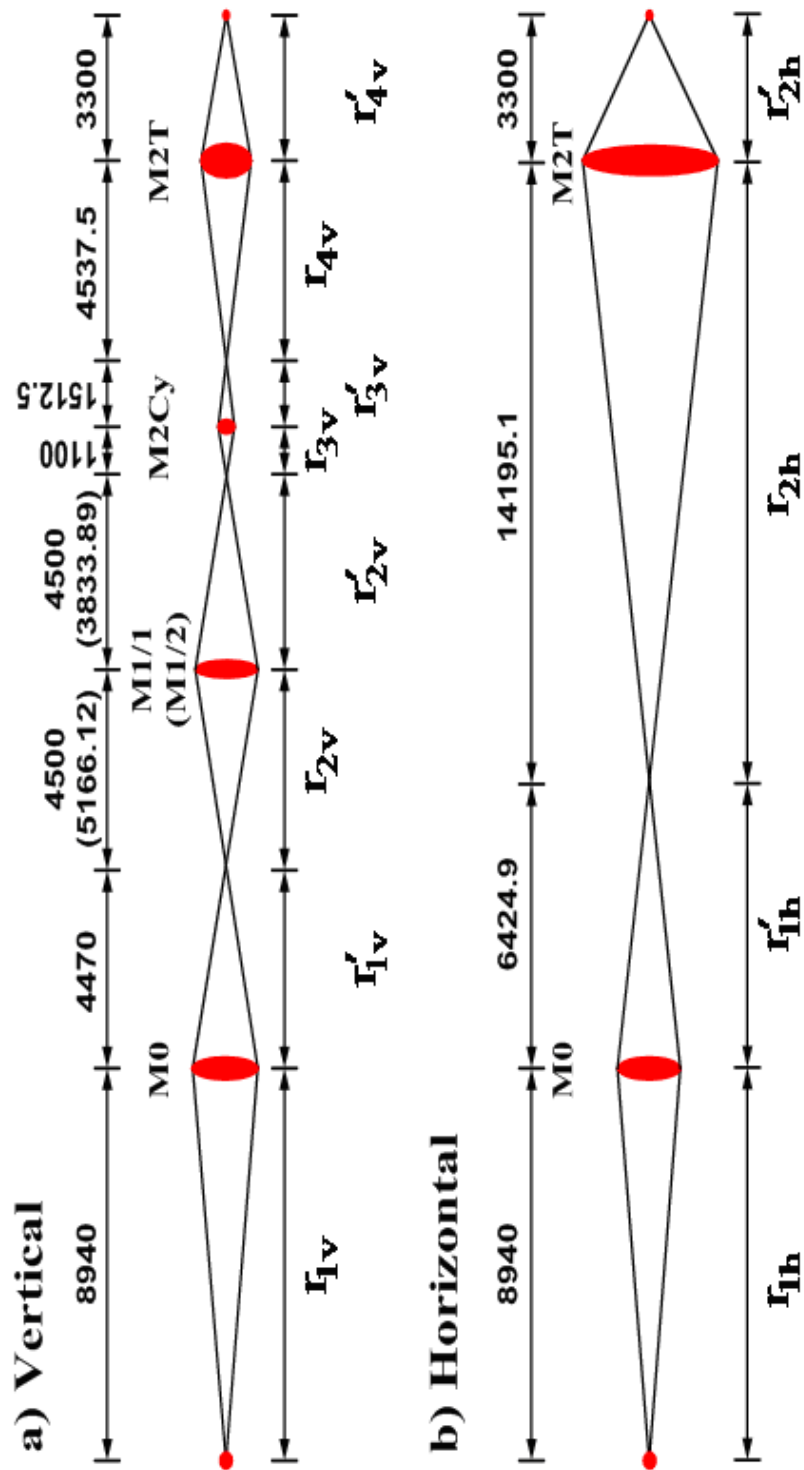
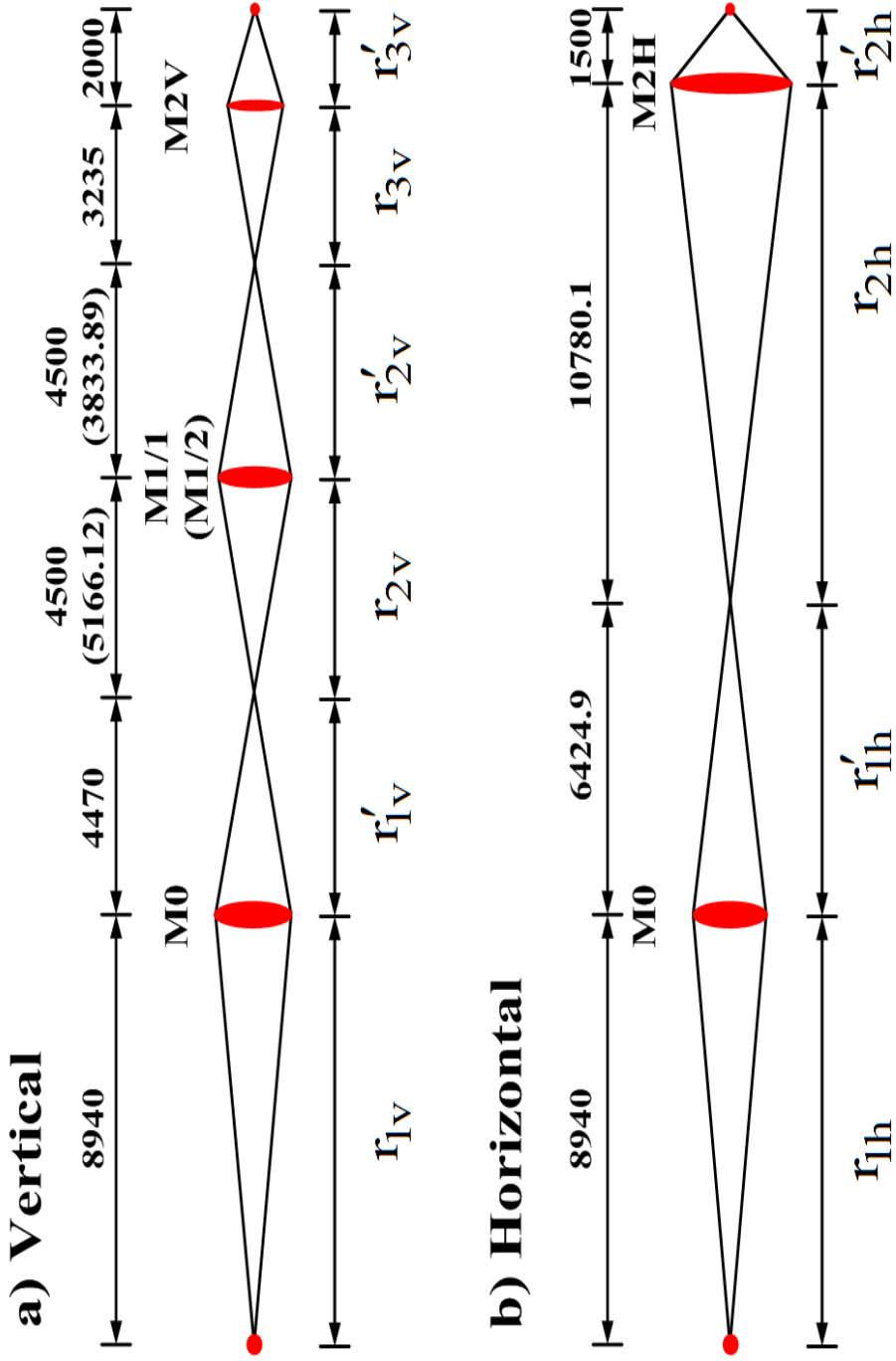


Figure 4.1 The optical layout of the BL3 beamline.



**Figure 4.2** The schematic diagram of the focusing optical element in the BL3 beamline for ARPES branchline a) in the vertical direction b) in the horizontal direction.



**Figure 4.3** The schematic diagram of the focusing optical element in the BL3 beamline for PEEEM branchline a) in the vertical direction b) in the horizontal direction.

## 4.2 Pre-focusing mirror

Reflection optical elements with grazing incidence, as illustrated in figure 4.4, are normally employed in VUV (vacuum ultraviolet) region. Consequently, focusing properties of mirrors in VUV light are severely effected by optical aberrations due to the grazing incident geometry. The situation is even worst when either 1) a large source size or 2) high demagnification is used. This is the case for the optical system of the BL3 PEEM branchline. The horizontal source size of the BL3 is very large:  $\sim 2.8$  mm FWHM. The beam size on the sample for PEEM is required to be equal to the maximum field-of-view of PEEM of about 500 microns. Thus, a large demagnification is required to make the beam spot small on the sample.

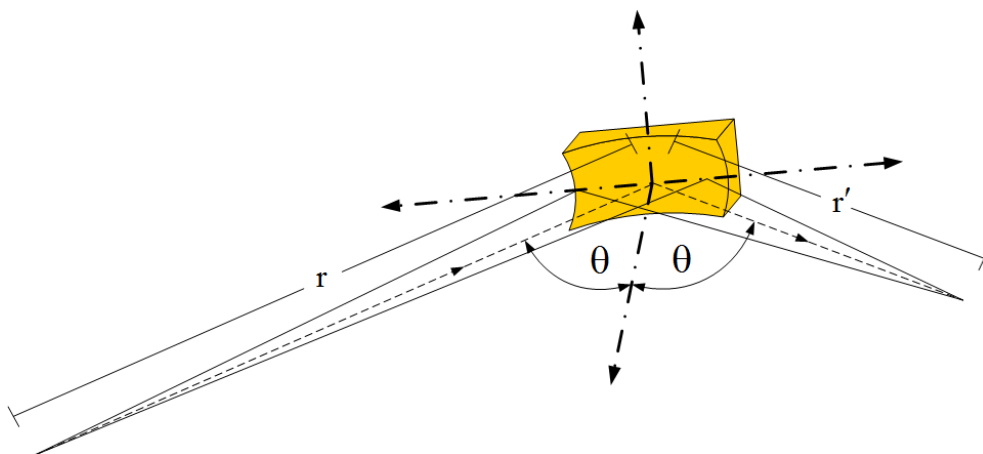


**Figure 4.4** Reflection mirror with grazing incident geometry.

### 4.2.1 Meridional focusing of pre-focusing mirror (M0)

M0 deflects the photon beam  $6^\circ$  horizontally. The meridional focusing of M0 deviates from the calculation. In BL3, a U60 undulator is an extended source with 41 periods and a period length of 60 mm. The horizontal FWHM of the beam

is  $\sim 2.8$  mm. Thus, the radius of curvature for the required focusing position must be obtained only from ray tracing simulations.

Initially, the meridional focusing of the pre-focusing mirror (M0) is designed for the collimated beam. From equation 1.36, the radius of curvature of M0 is 341,639 mm when the source distance is 8,940 mm, the image distance is infinity and the incidence angle is  $87^\circ$ . The ray tracing result shows that the beam is not collimated as shown in figure 4.5.

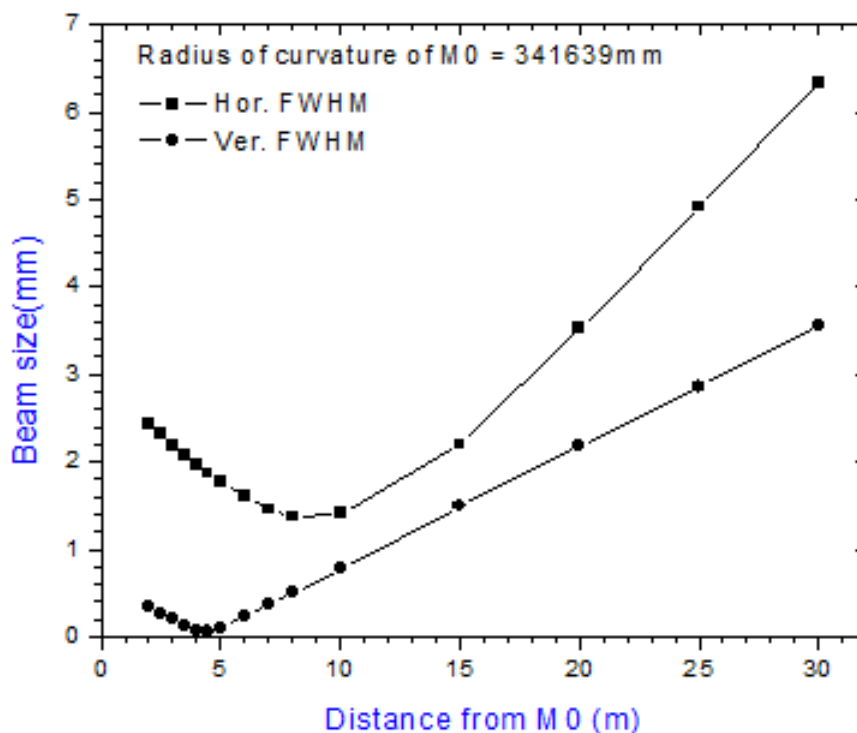


**Figure 4.5** The focusing property of M0. The sagittal focusing of M0 is agreed with the calculation (circle) but the meridional focusing of M0 is shown the divergence beam (square).

The sagittal focusing agrees with the calculation and the ray tracing result, and the beam has the focal point at the position that is expected. In contrast, the meridional focusing deviates from the calculation result, and the beam has a focal point that is not the collimated beam. This is the effect due to the large source size and the high demagnification.

Then, the relationship between the focal point and the radius of curvature of M0 is calculated by the ray tracing simulation as illustrated in figure 4.6. This relationship is used to optimize the horizontal beam size of the beamline.

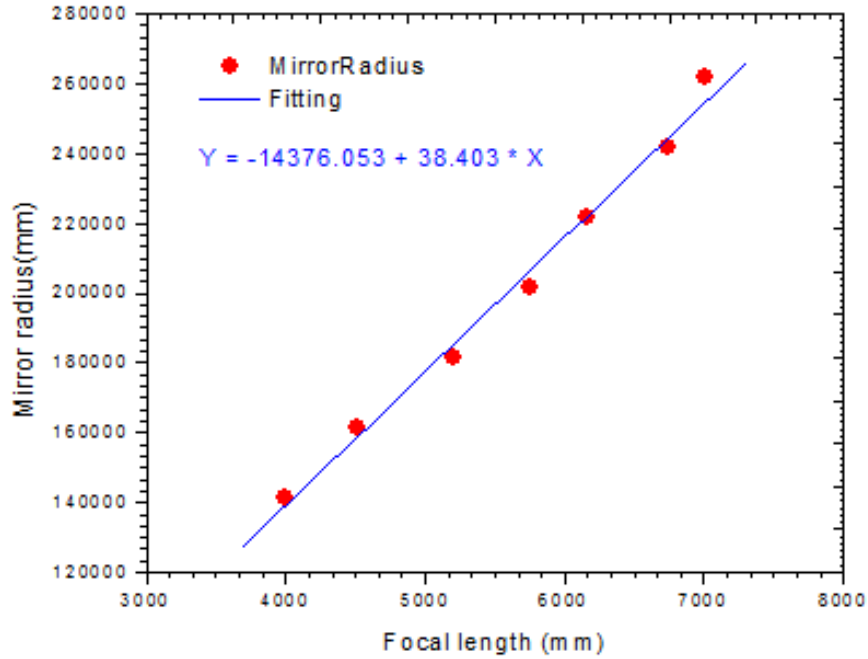


**Figure 4.6** The relation between the focal point and the radius of curvature of M0.

The relationship between focal point and the radius of curvature of M0 from the ray tracing simulation is linearly fitted. From the fitting, the equation of the line is given by

$$Y = -14376.053 + 38.403 \cdot X \quad (4.1)$$

where  $X$  is the focal point of M0, and  $Y$  is the radius of curvature of M0.

The total optical length of the PEEM branchline is 27,645 mm. The design considers the source distance of M0 and the image distance of M2H. The source distance of M0 is limited by three front-end chambers. The U60 undulator is placed in the straight section where the length from the center of U60 to the port of bending magnet number 3 is about 5000 mm. The image distance of the M2H

is limited by the working space of the PEEM branchline.

From the diagram shown in figure 4.3, the horizontal demagnification of the beamline which optimizes the radius of curvature of the pre-focusing mirror (M0) can be written by

$$DM_H = \frac{r'_{1h}}{r_{1h}} \times \frac{r'_{2h}}{r_{2h}}. \quad (4.2)$$

The equation 4.2 is used to calculate the image distance ( $r'_{1h}$ ) or the focal point of M0. The equation 4.1 to calculate the radius of curvature of M0 are shown in table 4.1.

**Table 4.2** Summary of the Radius of curvature of M0 depend on the demagnification.

Demagnification	Focal point (mm)	Radius of curvature of M0
8	7345.4	267709
8.5	7091.4	257955
9	6854.4	248853
9.5	6632.7	240340
10	6424.9	232360
11	6046.1	217812
12	5709.5	204886
15	4892.3	173503
20	3950.0	137316

The proper radius of curvature of M0 can be obtained from ray tracing simulations. The demagnification in the horizontal direction is optimized considering the beam size on the sample for PEEM required to be less than or equal to the maximum field-of-view of PEEM of 500 microns. Various images of the horizontal demagnifications at the sample position are optimized by simulation, as shown in illustrated 4.7.

The optimum horizontal demagnification of BL3 was found to be about 10. Furthermore, the images at the focal point of M0 from the calculation using equation of 2.35 and from the simulation are shown for comparison in figure 4.8

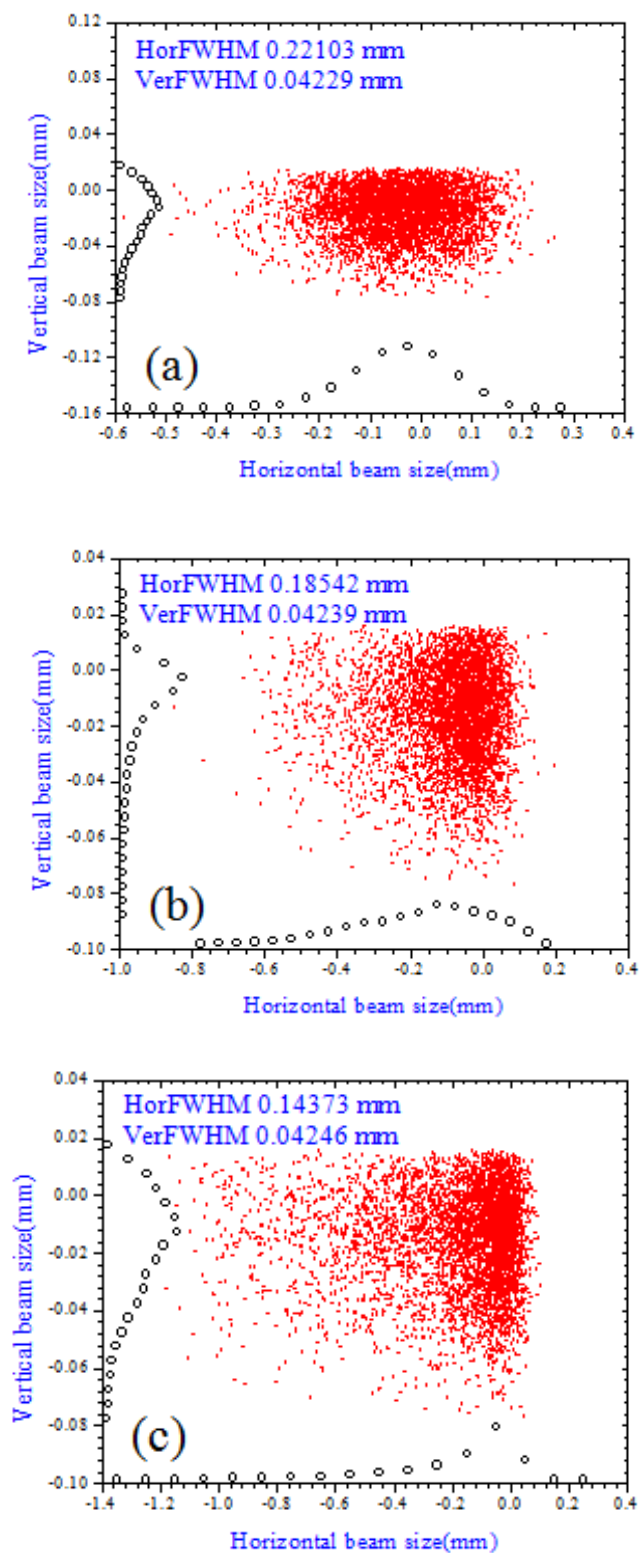


**Figure 4.7** The images of the photon energy 40 eV at sample position which are optimized by simulation, a) demagnification is 10, b) demagnification is 15 and c) demagnification is 20.

and 4.9, respectively.

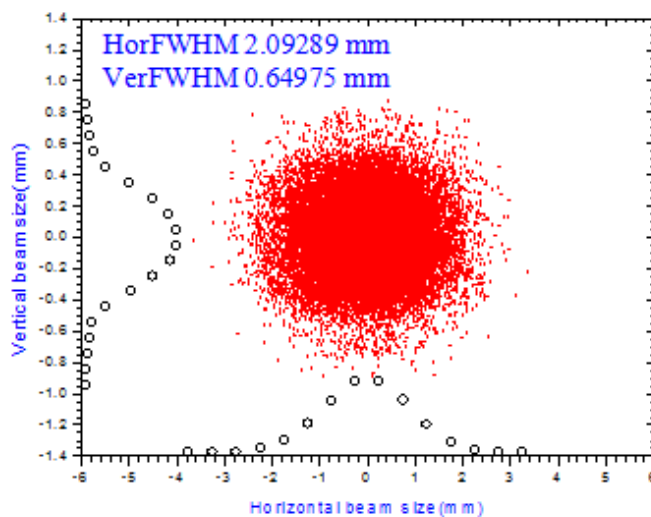


**Figure 4.8** Image of the photon energy 40 eV of the expected focusing position of M0 using the calculated radius of 142858 mm with demagnification 10.

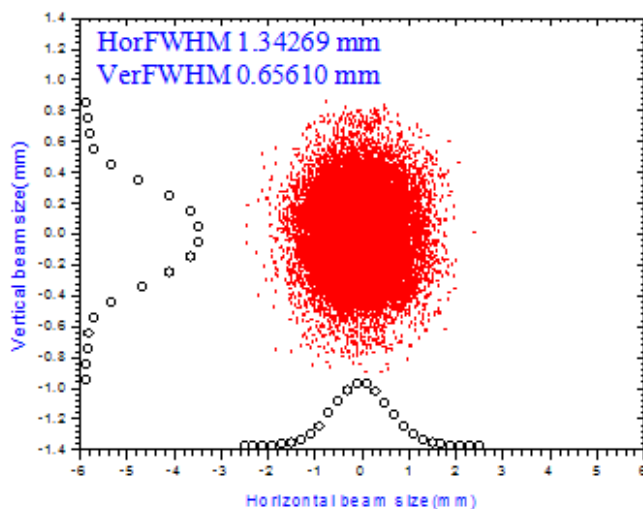


**Figure 4.9** Image of the photon energy 40 eV of the expected focusing position of M0 using the optimized radius of 232360 mm from simulations with demagnification 10.

The images at the sample position from the calculation and the simulation are shown in figure 4.10 and 4.11, respectively, for a comparison.

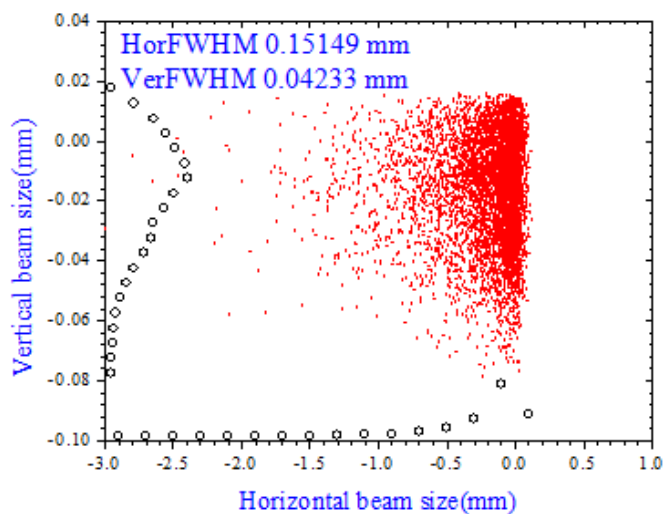


**Figure 4.10** Image at sample position using the calculated radius of 142858 mm with demagnification 10 for photon energy 40 eV.

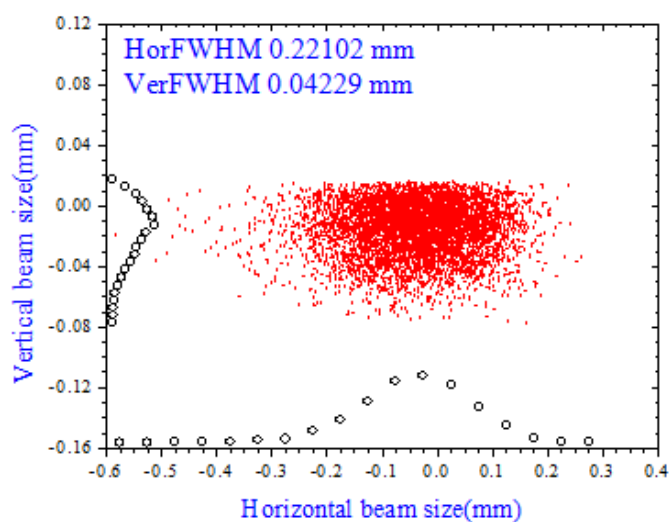


**Figure 4.11** Image at sample position using the optimized radius of 245299.4 mm from simulations with demagnification 10 for photon energy 40 eV.

#### 4.2.2 Sagittal focusing of pre-focusing mirror (M0)

The pre-focusing system employs a water-cooled toroidal mirror, M0, to deflect the light beam  $6^\circ$  horizontally and sagittally focusing the beam onto the entrance slit, S1, of the monochromator. Due to a small vertical beam size, the focusing properties in this direction do not deviate from calculations. A demag-

nification of 2 is chosen for M0 for flux optimization. M0 is 8,940 mm from the source and S1 is 4,470 mm from M0, as illustrated in figure 4.12.

From equation 2.36, the radius of curvature of M0 is 311.9 mm when the source distance is 8,940 mm, the image distance is 4,470 mm and the incidence angle is  $87^\circ$ .

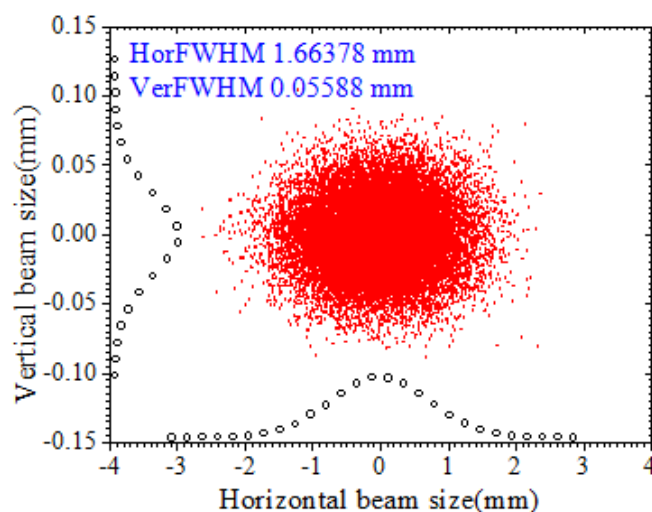


**Figure 4.12** The image of the pre-focusing mirror (M0) of the sagittal focus the beam onto the entrance slit (S1) for photon energy 40 eV.

Deriving from figure 3.3, the vertical FWHM of the beam source is 0.11238 mm and from figure 4.12, the vertical FWHM of the focused beam is 0.05588 mm. The simulation result of the sagittal focusing of pre-focusing mirror (M0) agrees with the calculation corresponding to the demagnification of 2.

The footprint of the pre-focusing mirror M0 is illustrated in figure 4.13. This explains the dimension and optical active area of the M0 mirror. Further specifications of the pre-focusing mirror M0 are given in table 4.3.

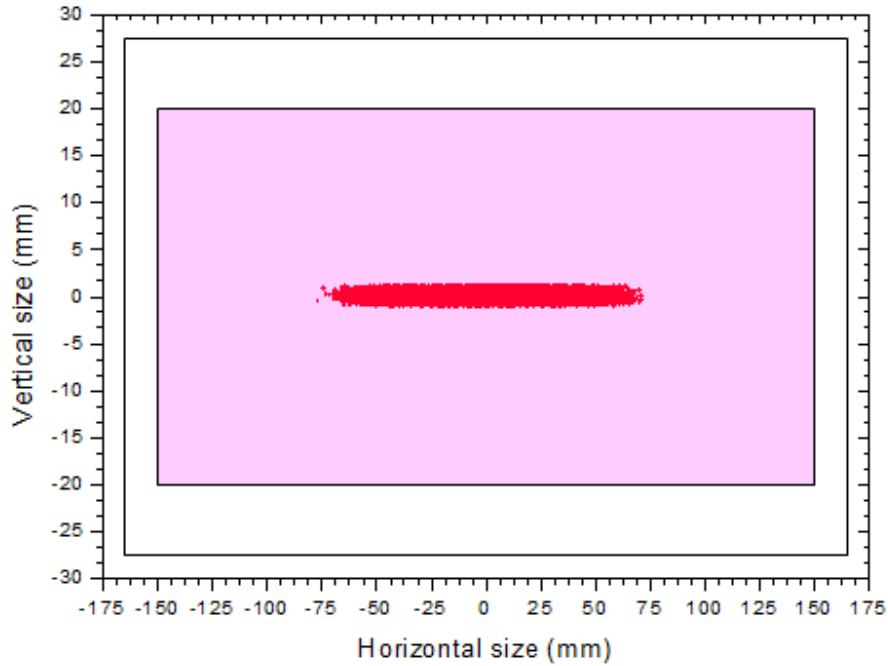


**Figure 4.13** The footprint of the pre-focusing mirror (M0) for photon energy 40 eV and opening angle  $0.2 \times 1 \text{ mrad}^2$  in vertical and horizontal, respectively. The shade rectangular and the transparent rectangular are represented the optical active area and the dimension of M0, respectively.

**Table 4.3** Summary of the specifications of M0.

Features/Properties	Specifications
Material	Si
Dimensions	Length = 330 mm Width = 55 mm Thickness = 40 mm
Optical active area	$300 \times 40 \text{ mm}^2$
Coating	50 nm Au
Geometry	Radius tangential R = 232360 mm $\pm$ 2% Radius sagittal R = 311.9 mm $\pm$ 5%
Slope Error	Tangential: $\leq 1 \text{ arcsec rms}$ Sagittal: $\leq 2 \text{ arcsec rms}$
Surface Roughness	$\leq 0.5 \text{ nm rms}$

### 4.3 Monochromators

Varied line-spacing plane grating (VLSPG) monochromator is adopted because of the ease to obtain high resolving power by choosing proper line-space-

variation coefficients of a grating and the simplicity of its energy scanning mechanism. The VLSPG monochromator is employed in the BL3 beamline operating in the constant-included-angle geometry with included angles of  $167.5^\circ$  and  $172.5^\circ$  for the low and high photon energy ranges, respectively as shown in figure 4.14. The optics of the VLSPG monochromator consists of the entrance slit (S1), the exit slit (S2) and two exchangeable spherical focusing mirrors (M1/1 and M1/2) with constant included angles, and three exchangeable VLSPG gratings necessary to cover two photon energy ranges of 40–160 eV and 220–1040 eV. For the low photon energy range, a grating with groove density  $N_0$  (the density at the middle of the grating) of 600 lines/mm is used. Two gratings with  $N_0$  of 1200 and 2400 lines/mm are used for the high photon energy range. Because the monochromator is optimized for 220–1040 eV, the demagnification of the focusing spherical mirror M1/1 is chosen to be 1.0 to minimize the optical aberrations. Switching to 40–160 eV range is made by moving M1/1 upward, allowing the beam to travel to the second focusing spherical mirror, M1/2. The entrance slit is illuminated by the reflected light from the pre-focusing mirror (M0), which can be treated as a source for the monochromators section. An X-Y aperture (Ap) inserted between the entrance slit (S1) and the two exchangeable focusing spherical mirrors (M1/1 and M1/2) are used to reduce coma and aberrations to obtain the highest resolution. The total lengths of the monochromator are 9,014 and 9,012 mm for the  $167.5^\circ$  and  $172.5^\circ$  included-angle configurations, respectively. The VLSPG gratings are selected by linear translation mechanism, and the photon energy scanning is made by grating rotation. The orders of diffraction are chosen the first positive (inside order) to give the maximum dispersion. As illustrated in figure 4.15, the light source of the grating is a virtual light located at the back side of the grating. A convergent synchrotron beam hits the VLSPG grating. The convergent beam is

reflected from the upstream two exchangeable focusing spherical mirrors (M1/1 and M1/2). The incidence angles as well as the diffraction angle at point 1 and point 2 are not significantly different. This makes photons with a broad energy bandwidth pass through the exit slit (S2). To solve this problem, the equation 2.34 is used to minimize the  $F_{100}$  term, and the groove density of the grating must be varied along the  $\omega$  direction (the same direction as the beam) perpendicular to the groove line. This is a feature of VLSPG grating that the line spacing is varied to compensate the differences of the incidence angle and the diffraction angle at both ends of the grating.

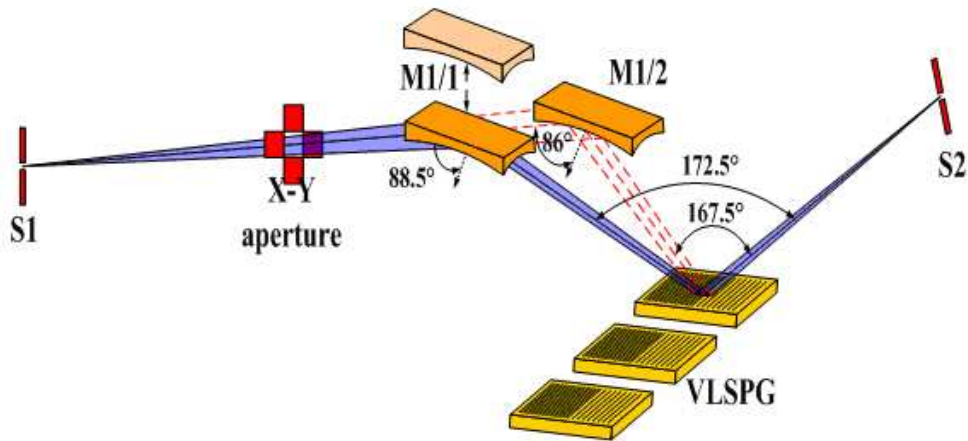


**Figure 4.14** The diagram of the BL3 monochromator section that consist of entrance slit (S1), X-Y aperture, two exchangeable focusing spherical mirrors (M1/1 and M1/2), VLSPG gratings and exit slit (S2).

The line-space variation coefficients are defined by a groove density function of  $N(\omega) = N_0(1 + a_1\omega + a_2\omega^2 + a_3\omega^3 + \dots)$ . The coefficient  $a_1$ ,  $a_2$  and  $a_3$  and the exit arm length ( $r_2$ ) of the grating are determined by minimizing the aberrations with procedures given elsewhere (Songsiriritthigul et al., 2001). For the monochromator of BL3, the photon energies of  $E_1$ ,  $E_2$ , are chosen to satisfy the

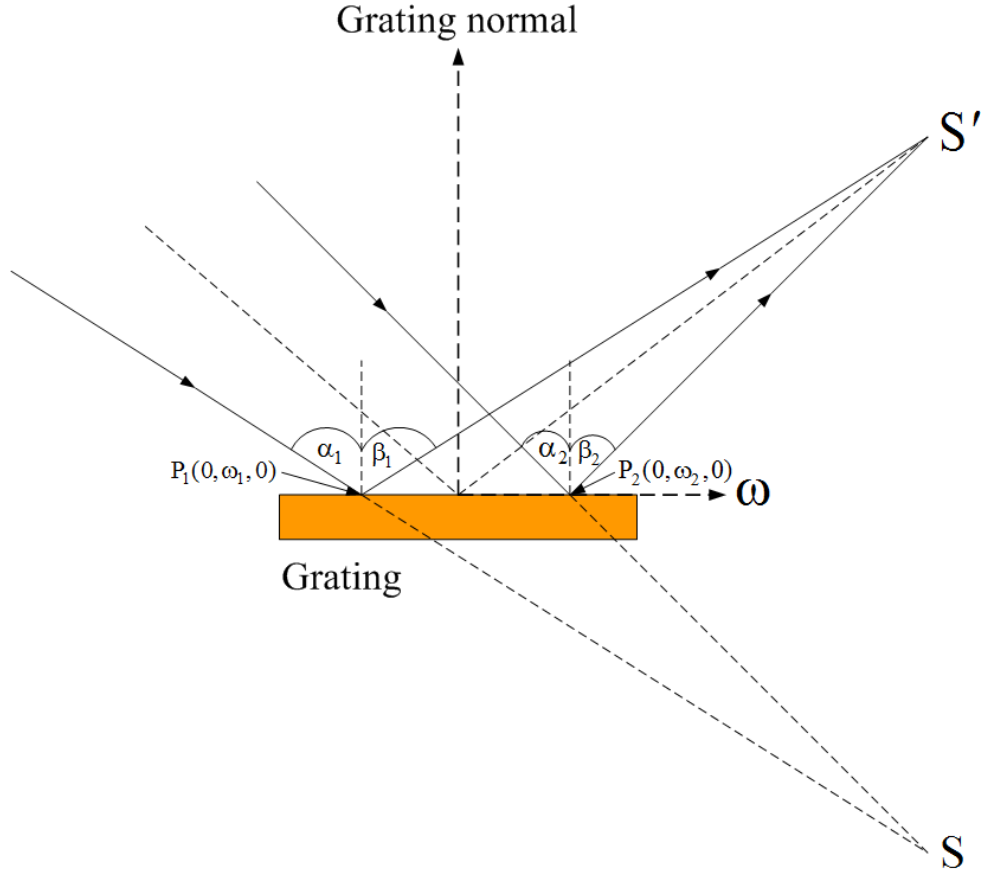


**Figure 4.15** The convergent synchrotron beam hit on VLSPG. It should be noted that the differences of incidence angles and diffraction angles at point 1 and 2 are small different.

condition  $F_{200}(E_1) = F_{200}(E_2) = 0$  for the coefficient  $a_1$  and the exit arm length ( $r_2$ ). And the photon energies of  $E_3$  and  $E_4$  are chosen to satisfy the condition  $F_{300}(E_3) = 0$  and  $F_{400}(E_4) = 0$  for the coefficient  $a_2$  and  $a_3$ , respectively. The values of  $E_1$ ,  $E_2$ ,  $E_3$  and  $E_4$  are given in table 4.4. The exit arm length ( $r_2$ ), the coefficient of  $a_1$ ,  $a_2$  and  $a_3$  for all VLSPG gratings are 3,447.97 m,  $-5.781 \times 10^{-4} \text{mm}^{-1}$ ,  $2.500 \times 10^{-7} \text{mm}^{-2}$  and  $9.591 \times 10^{-11} \text{mm}^{-3}$ , respectively. It should be noted that the advantage of the VLSPG monochromator is that scanning of photon energy can be done simply by a grating rotation. The monochromatic light is focused virtually to the position of the exit slit S2, so that no movement of the exit slit along the optical axis during energy scans is necessary. There is no need to move

the exit slit after switching the energy range as well.

**Table 4.4** The optimized values of  $E_1$ ,  $E_2$ ,  $E_3$  and  $E_4$  that used for determining the coefficient of line spacing and the exit arm length of the BL3's VLSPG gratings.

Grating number	$E_1$ (eV)	$E_2$ (eV)	$E_3$ (eV)	$E_4$ (eV)
VLSPG1	51.6129	129.032	65.1613	113.548
VLSPG2	250	450	85	410
VLSPG3	500	900	570	820

The footprint of the M1/1 mirror of the BL3 beamline is illustrated in figure 4.16 which explains the dimension and the optically active area of the M1/1 mirror. Furthermore, the specifications of the M1/1 mirror of the BL3 beamline are given by table 4.5.

The footprint of BL3 M1/2 mirror is illustrated in figure 4.17 which explains the dimension and the optically active area of the M1/2 mirror. Specifications of the BL3 M1/2 mirror are given in table 4.6.

**Table 4.5** Summary of the specifications of M1/1.

Features/Properties	Specifications
Material	Si
Dimensions	Length = 140 mm
	Width = 40 mm
	Thickness = 40 mm
Optical active area	120 x 30 mm <sup>2</sup>
Coating	50 nm Au
Geometry	Radius R = 171907 mm +/- 1%
Slope Error	Tangential: $\leq 0.2$ arcsec rms
	Sagittal: $\leq 0.5$ arcsec rms
Surface Roughness	$\leq 0.5$ nm rms

The footprint of the 1<sup>st</sup> VLSPG grating of the BL3 beamline is illustrated in figure 4.18 which explains the dimension and optically active area of the VLSPG

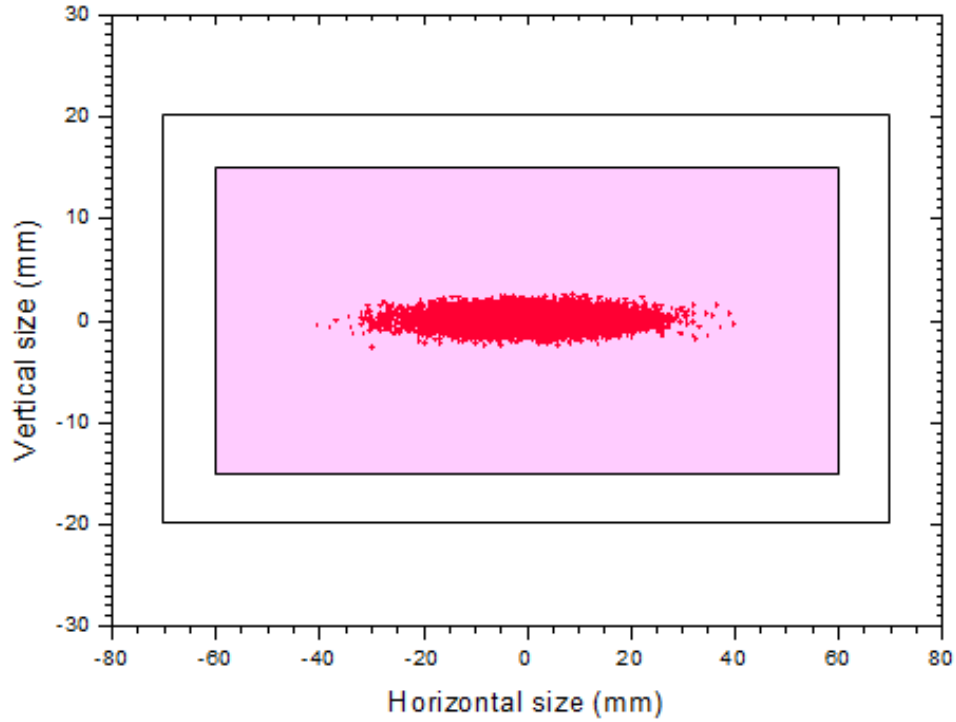


**Figure 4.16** The footprint of the M1/1 mirror for photon energy 280 eV and opening angle  $0.2 \times 1 \text{ mrad}^2$  in vertical and horizontal, respectively. The shade rectangular and the transparent rectangular are represented the optical active area and the dimension of M1/1 mirror, respectively.

**Table 4.6** Summary of the specifications of M1/2.

Features/Properties	Specifications
Material	Si
Dimensions	Length = 140 mm
	Width = 40 mm
	Thickness = 40 mm
Optical active area	120 x 40 mm <sup>2</sup>
Coating	50 nm Au
Geometry	Radius R = 63230 mm +/- 1%
Slope Error	Tangential: $\leq 0.2$ arcsec rms
	Sagittal: $\leq 0.5$ arcsec rms
Surface Roughness	$\leq 0.5$ nm rms

grating. Furthermore, the specifications of three VLSPG gratings of the BL3 beamline are given in table 4.7.

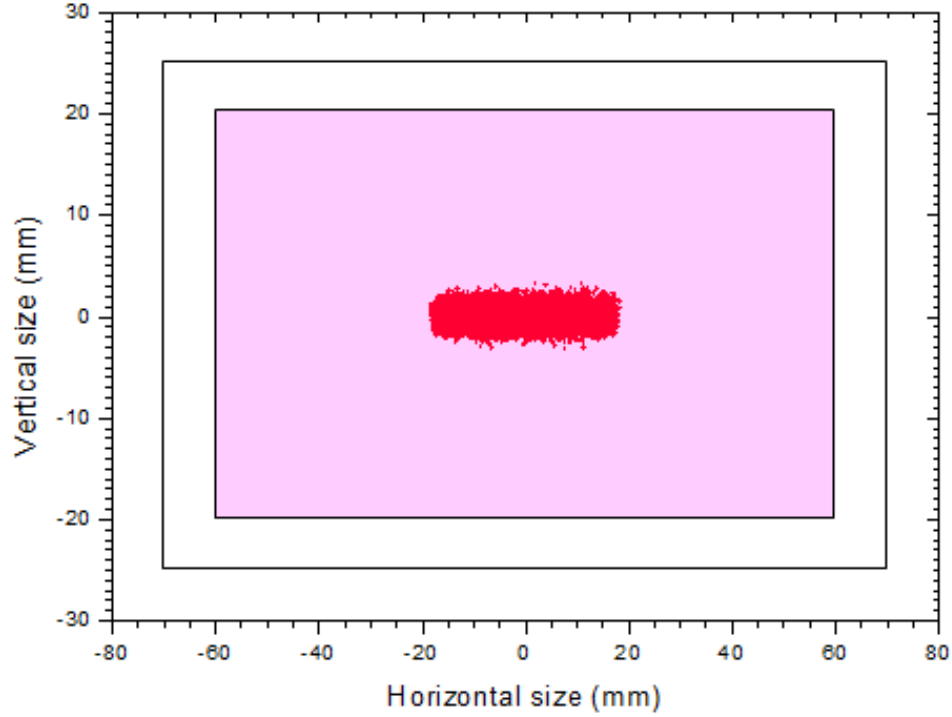


**Figure 4.17** The footprint of the M1/2 mirror for photon energy 40 eV and opening angle  $0.2 \times 1$  mrad<sup>2</sup> in vertical and horizontal, respectively. The shade rectangular and the transparent rectangular are represented the optical active area and the dimension of M1/2 mirror, respectively.

Resolution ( $\Delta E/E$ ) of the VLSPG gratings of BL3 is obtained from the analytical calculation using the equations as described in Chapter II. The results are illustrated in figure 4.19 and 4.20 for low and high photon energies, respectively. In the calculation, the widths of the entrance and exit slits are varied depending on the photon energy. The contribution to the resolution caused by the slit widths are fixed at  $1 \times 10^{-4}$ . The relationship between the widths of the entrance and exit slit and the photon energy at a fixed resolution of  $1 \times 10^{-4}$  is shown in figure 4.21 and 4.22 for low and high photon energies, respectively.

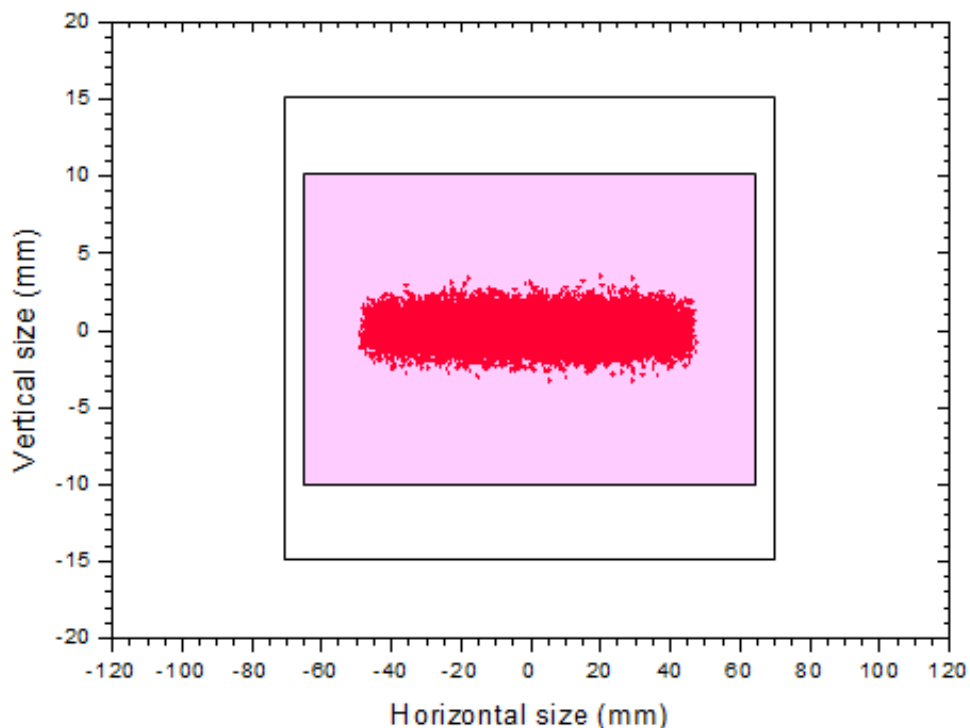


**Figure 4.18** The footprint of the 1st VLSPG grating for photon energy 40 eV and opening angle  $0.2 \times 1$  mrad<sup>2</sup> in vertical and horizontal, respectively. The shade rectangular and the transparent rectangular are represented the optical active area and the dimension of the 1st VLSPG grating, respectively.

#### 4.4 Post-focusing mirrors

The monochromatic beam is dispersed by the grating. It is then focused by post-focusing mirror to deliver the beam to the end station. Directing the beam to either end station of BL3 is done by M2Cy mirror. When the M2Cy mirror is out of the optical axis, the monochromatic beam goes directly to PEEM. On the other hand, when the M2Cy mirror is in the optical axis, the monochromatic beam is directed to ARPES. The M2Cy mirror has cylindrical configuration, and focuses the beam in sagittal direction. The M2Cy has a radius of curvature of 66.7 mm corresponding to a source distance of 1,100 mm, an image distance of 1,512.5 mm and an incidence angle of  $87^\circ$ .

**Table 4.7** The specifications of the BL3's VLSPG gratings.

	<b>VLSPG1</b>	<b>VLSPG2</b>	<b>VLSPG3</b>
Profile	Laminar holography	Laminar holography	Laminar holography
Material	Single crystal silicon	Single crystal silicon	Single crystal silicon
Optical surface	Plane	Plane	Plane
Coating	Gold	Nickel	Gold
Coating thickness (nm)	50	50	50
Dimension (mm) length×width ×thickness	140×30×20	140×30×20	140×30×20
Optical active area (mm)	130×20	130×20	130×20
Groove density at the center (lines/mm)	600	1200	2400
Energy range (eV)	40-160	220-520	440-1040
Included angle	167.5°	172.5°	172.5°
Micro roughness	≤ 0.5 nm rms	≤ 0.5 nm rms	≤ 0.5 nm rms
Slope error			
Tangential	≤ 0.2 arcsec rms	≤ 0.2 arcsec rms	≤ 0.2 arcsec rms
Sagittal	≤ 0.5 arcsec rms	≤ 0.5 arcsec rms	≤ 0.5 arcsec rms

The footprint of the M2Cy mirror of BL3 is illustrated in figure 4.23 which explains the dimension and optically active area of the M2Cy mirror.

Furthermore, the specifications of the M2Cy mirror are given in table 4.8.

#### 4.4.1 Toriodal mirror for ARPES

The configuration of the post-focusing mirror of the ARPES branchline is a toriodal mirror. This type of the mirror allows focusing power in two directions (sagittal and meridional foci). Therefore, this branchline needs only one mirror to focus the beam in both axes.

To find demagnification in the vertical axis, the calculation of the post-focusing optics must include the M2Cy mirror. The demagnification of the post-

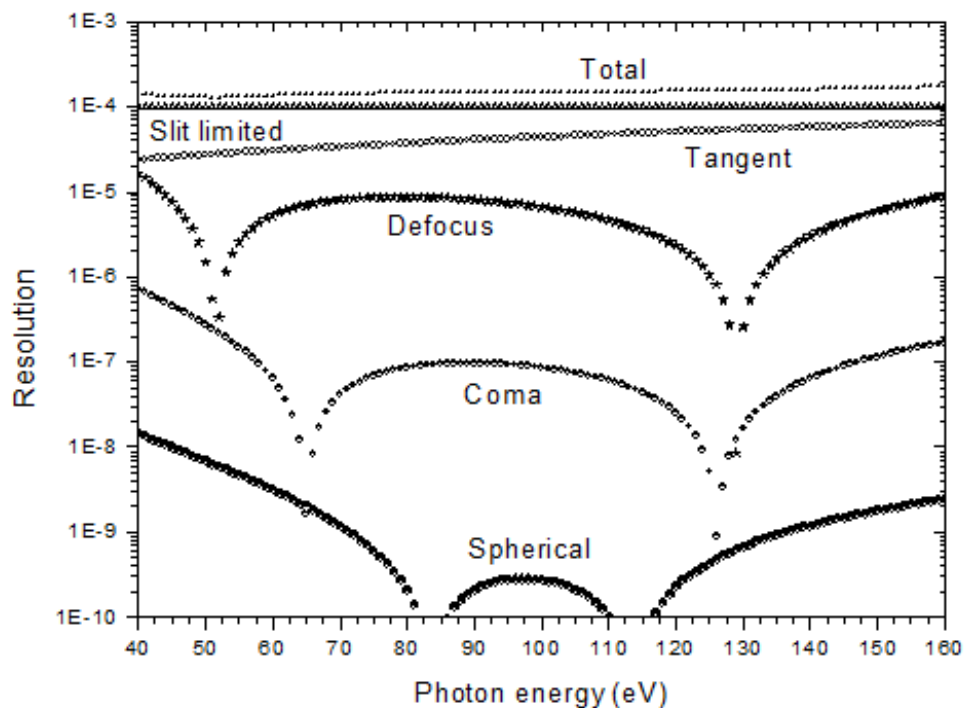


**Figure 4.19** The calculation of spherical, coma, defocus, tangent error aberrations and slit limited by the width of the entrance and the exit slit of the 1st grating of BL3 beamline.

**Table 4.8** Summary of the specifications of M2Cy.

Features/Properties	Specifications
Material	Zerodus
Dimensions	Length = 270 mm
	Width = 40 mm
	Thickness = 40 mm
Optical active area	250 x 25 mm <sup>2</sup>
Coating	50 nm Au
Geometry	Radius sagittal R = 66.7 mm +/- 2%
Slope Error	Tangential: $\leq 1$ arcsec rms
	Sagittal: $\leq 2$ arcsec rms
Surface Roughness	$\leq 0.5$ nm rms

focusing of the ARPES branchline is equal to 1, which is dependent on the vertical demagnification of the whole ARPES branchline which is 2, as shown in figure 4.2.

From this, the source distance of the M2T mirror is 4,537.5 mm and the image

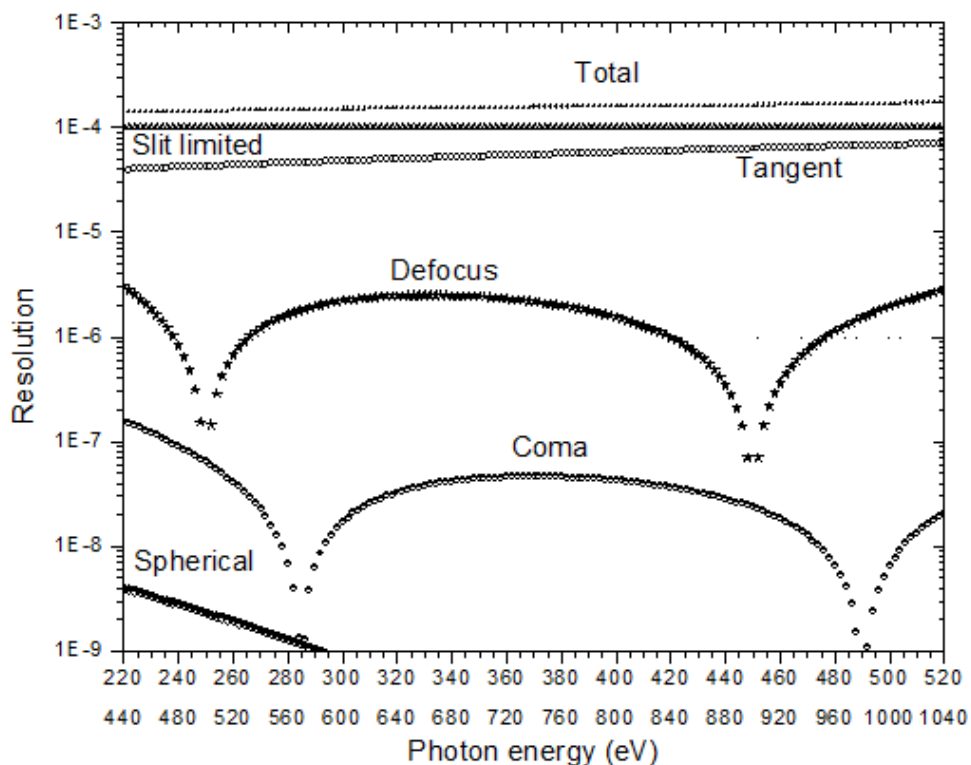


**Figure 4.20** The calculation of spherical, coma, defocus, tangent error aberrations and slit limited by the width of the entrance and the exit slit of the 2<sup>nd</sup> and 3<sup>rd</sup> grating of BL3 beamline.

distance is 3,300 mm with the incidence angle of  $87.75^\circ$  to make the beam parallel to the floor. The corresponding minor radius of curvature is 210.2 mm.

In the horizontal axis, the demagnification is chosen to 4.3, which is dependent on the horizontal demagnification of the whole ARPES branchline which is 6. The source distance of the M2T is 14,195.1 mm, the image distance is 3300 mm, and the incidence angle is  $87.75^\circ$ . The corresponding major radius of curvature is 97327 mm.

The footprint of the M2T mirror of BL3 is illustrated in figure 4.24 which explains the dimension and the optically active area of the M2T mirror. Furthermore, the specifications of the M2T mirror is given in table 4.9.

The foot print of the M2T mirror of the BL3 beamline is illustrated in

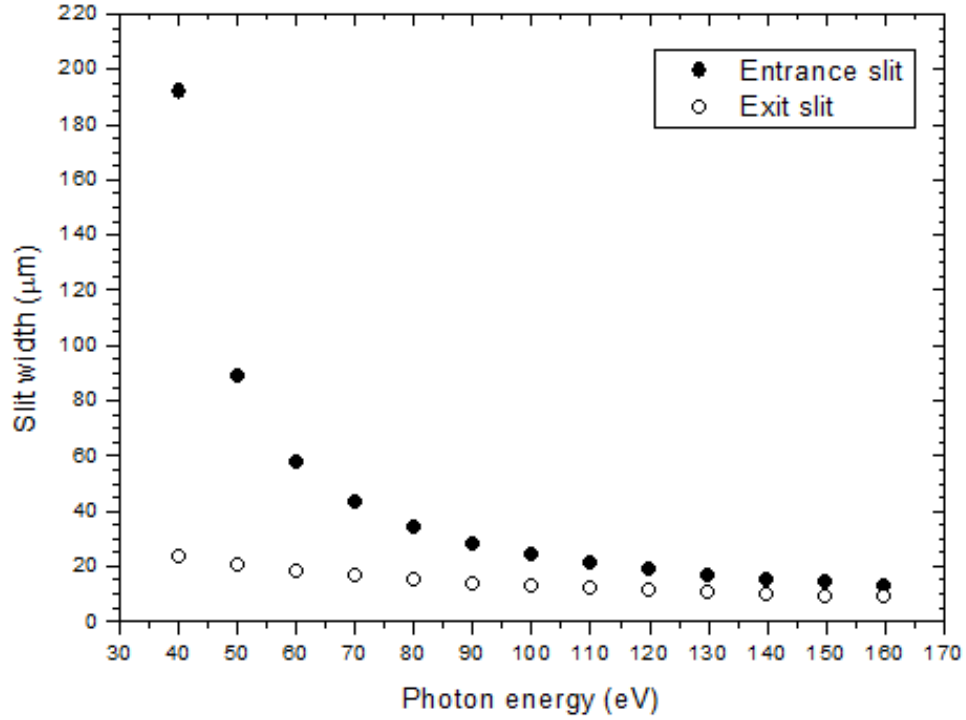


**Figure 4.21** The widths of entrance and exit slit with the photon energy for grating 1 (low photon energy) that obtain at a fixed resolution of  $1 \times 10^{-4}$ .

figure 4.24, it is explained the dimension and optical active area of the M2T mirror. Furthermore, the specifications of the M2T mirror is given in table 4.9.

**Table 4.9** Summary of the specifications of M2T.

Features/Properties	Specifications
Material	Zerodus
Dimensions	Length = 240 mm
	Width = 50 mm
	Thickness = 40 mm
Optical active area	$220 \times 35 \text{ mm}^2$
Coating	50 nm Au
Geometry	Radius tangential R = 97327 mm +/- 2%
	Radius sagittal R = 210.2 mm +/- 5%
Slope Error	Tangential: $\leq 1$ arcsec rms
	Sagittal: $\leq 5$ arcsec rms
Surface Roughness	$\leq 0.5$ nm rms

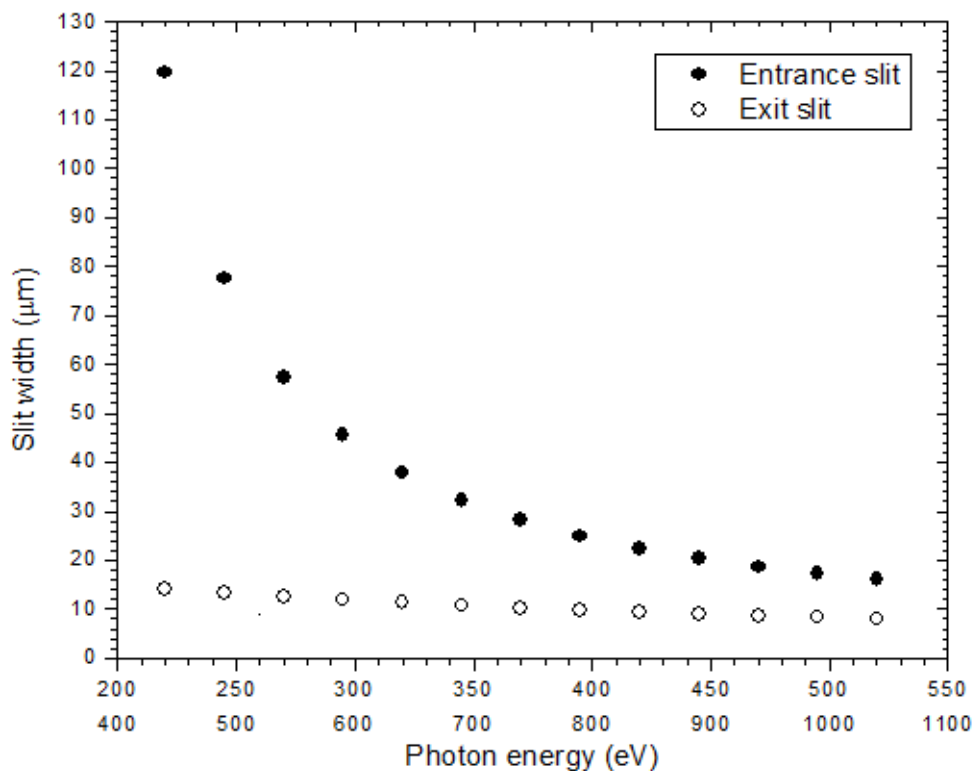


**Figure 4.22** The widths of entrance and exit slit with the photon energy for grating 2 and 3 (high photon energy) that obtain at a fixed resolution of  $1 \times 10^{-4}$ .

#### 4.4.2 K-B mirrors for PEEM

The PEEM branchline uses KB mirror configuration as the post-focusing optics. For our purpose we use two cylindrical mirrors in the KB configuration. The curvature of vertical focusing mirror is adjustable.

In the vertical direction, the M2V mirror is designed for demagnification of 1.6175, which is dependent on the vertical demagnification of the whole PEEM branchline which is 3.235. So, the source distance of the M2V mirror is 3,235 mm and the image distance is 2,000 mm with the incidence angle of  $87.75^\circ$  to make the beam parallel to the floor. The corresponding radius of curvature is 62,961 mm.

In the horizontal direction, the demagnification is chosen to 7.2, which is dependent on the horizontal demagnification of the whole PEEM branchline which

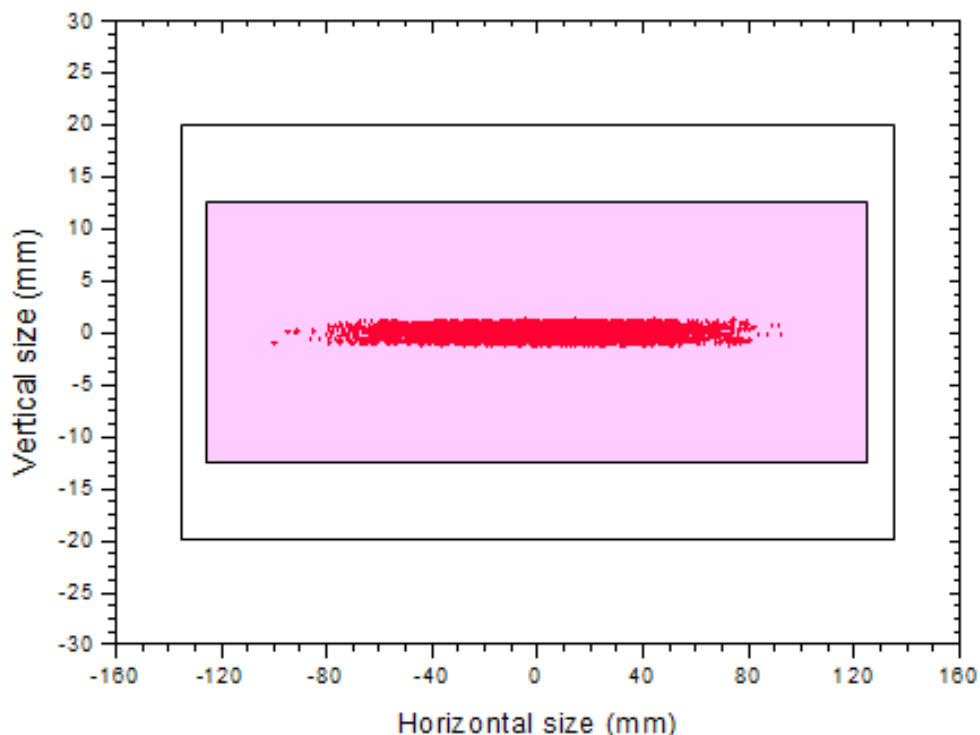


**Figure 4.23** The footprint of the M2Cy mirror for photon energy 40 eV and opening angle  $0.2 \times 1 \text{ mrad}^2$  in vertical and horizontal, respectively. The shade rectangular and the transparent rectangular are represented the optical active area and the dimension of the M2Cy mirror, respectively.

is 10. The source distance of the M2V is 10,780.1 mm, the image distance is 2,000 mm, and the incidence angle is  $87^\circ$ . The corresponding major radius of curvature is 50,320 mm.

The footprint of the M2V and M2H mirrors of BL3 is illustrated in figure 4.25 and 4.26 which explain the dimension and optically active area of the M2V and M2H mirrors, respectively. Furthermore, the specifications of the M2V and M2H mirrors are given in table 4.10 and 4.11, respectively.

The foot print of the M2V and M2H mirrors of the BL3 beamline is illustrated in figure 4.25 and 4.26, these are explained the dimension and optical active area of the M2V and M2H mirrors, respectively. Furthermore, the specifications of the M2V and M2H mirrors are given in table 4.10 and 4.11, respectively.

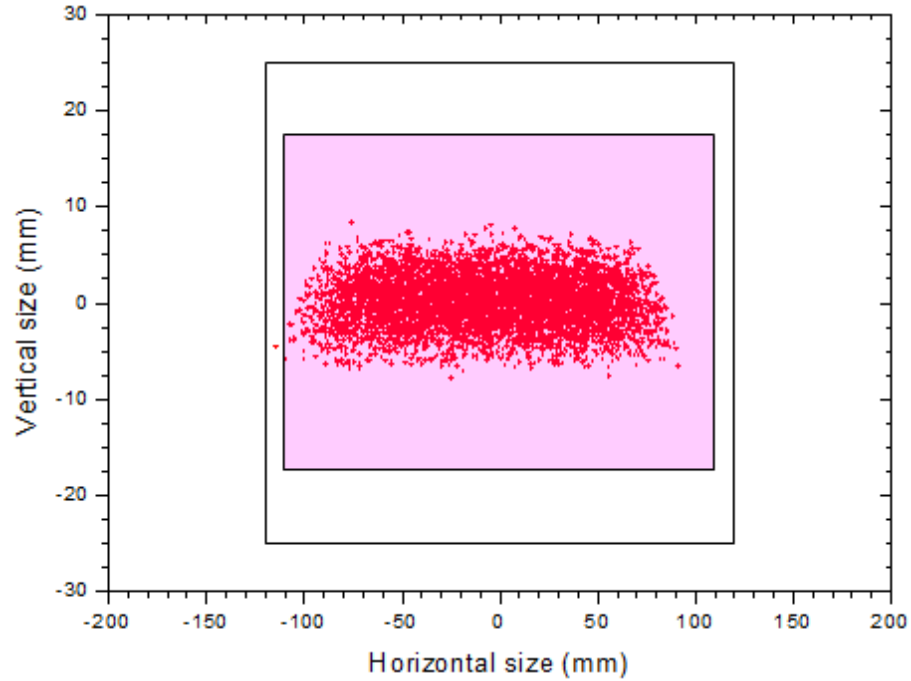


**Figure 4.24** The footprint of the M2T mirror for photon energy 40 eV and opening angle  $0.2 \times 1 \text{ mrad}^2$  in vertical and horizontal, respectively. The shade rectangular and the transparent rectangular are represented the optical active area and the dimension of the M2T mirror, respectively.

**Table 4.10** Summary of the specifications of M2V.

Features/Properties	Specifications
Material	Zerodus
Dimensions	Length = 300 mm
	Width = 40 mm
	Thickness = 15 mm
Optical active area	$250 \times 25 \text{ mm}^2$
Coating	50 nm Au
Geometry	Radius tangential R = 62961 mm +/- 2%
Slope Error	Tangential: $\leq 1 \text{ arcsec rms}$
	Sagittal: $\leq 1 \text{ arcsec rms}$
Surface Roughness	$\leq 0.5 \text{ nm rms}$

## 4.5 Flux at sample

The photon flux at the sample position is essentially proportional to the flux delivered by the central cone of the undulator radiation. The reflectivity

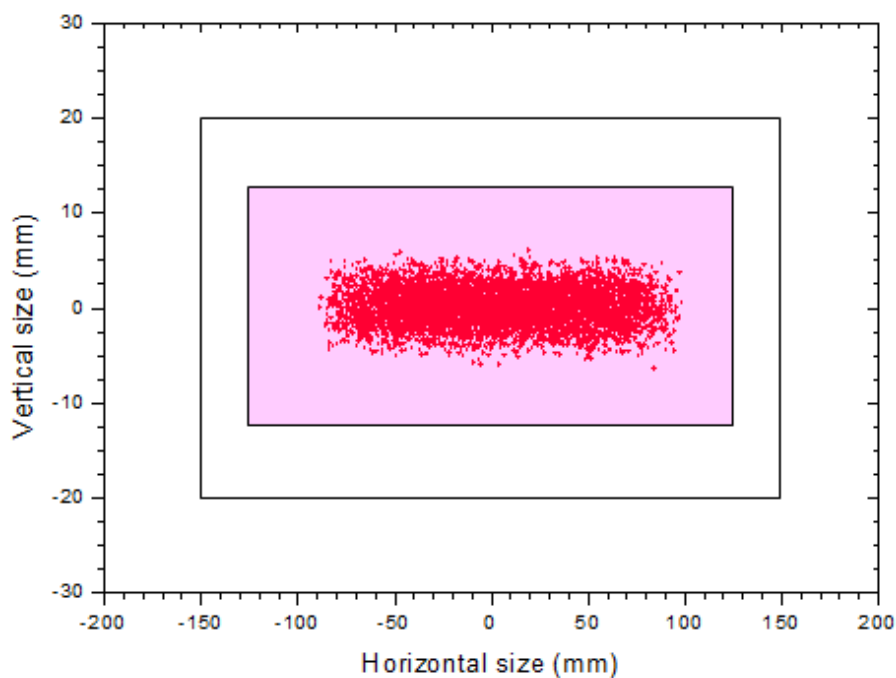


**Figure 4.25** The footprint of the M2V mirror for photon energy 40 eV and opening angle  $0.2 \times 1 \text{ mrad}^2$  in vertical and horizontal, respectively. The shade rectangular and the transparent rectangular are represented the optical active area and the dimension of the M2V mirror, respectively.

**Table 4.11** Summary of the specifications of M2H.

Features/Properties	Specifications
Material	Zerodus
Dimensions	Length = 320 mm
	Width = 40 mm
	Thickness = 40 mm
Optical active area	300 x 25 mm <sup>2</sup>
Coating	50 nm Au
Geometry	Radius tangential R = 50320 mm +/- 2%
Slope Error	Tangential: $\leq 1 \text{ arcsec rms}$
	Sagittal: $\leq 1 \text{ arcsec rms}$
Surface Roughness	$\leq 0.5 \text{ nm rms}$

of the mirrors, the efficiency and the reflectivity of the gratings, and the beam intensity after the entrance and exit slits are taken into account for the flux calculation. The calculated flux of the PEEM branchline at the sample position is

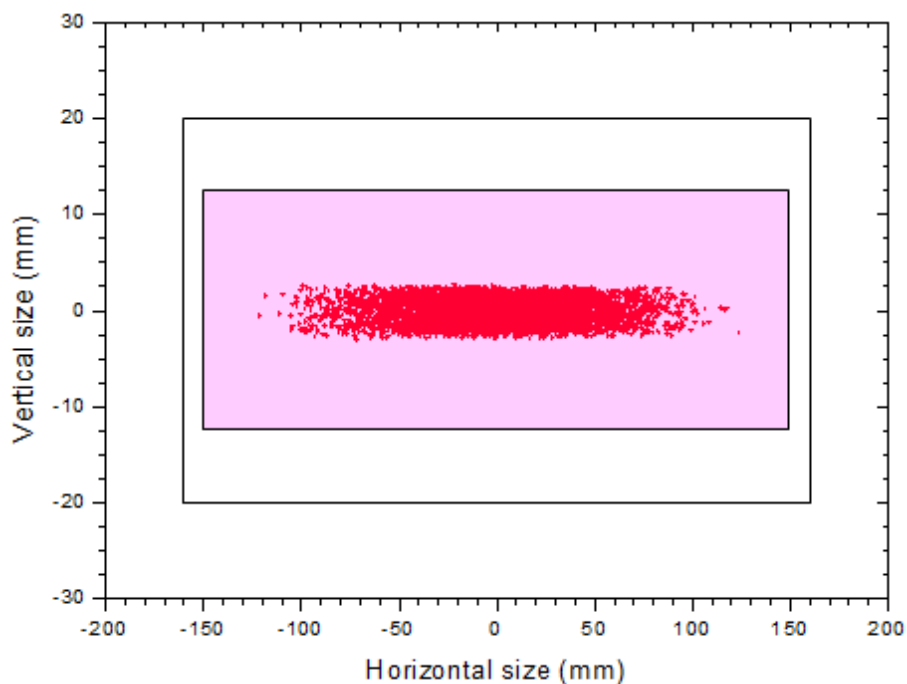


**Figure 4.26** The footprint of the M2H mirror for photon energy 40 eV and opening angle  $0.2 \times 1 \text{ mrad}^2$  in vertical and horizontal, respectively. The shade rectangular and the transparent rectangular are represented the optical active area and the dimension of the M2H mirror, respectively.

above  $2 \times 10^9$  photons/s/100 mA, as illustrated in figure 4.27.

## 4.6 Beam size at sample position

### 4.6.1 ARPES position

Grating number 1 has the groove density of 600 lines/mm at the middle. The beam size at the sample position for a photon energy of 40 eV is shown in figure 4.28.

For grating number 2, the groove density at the middle of the grating is 1200 lines/mm. The beam size at the sample position for a photon energy of 280 eV is shown in figure 4.29.

For grating number 3, the groove density at the middle of the grating is

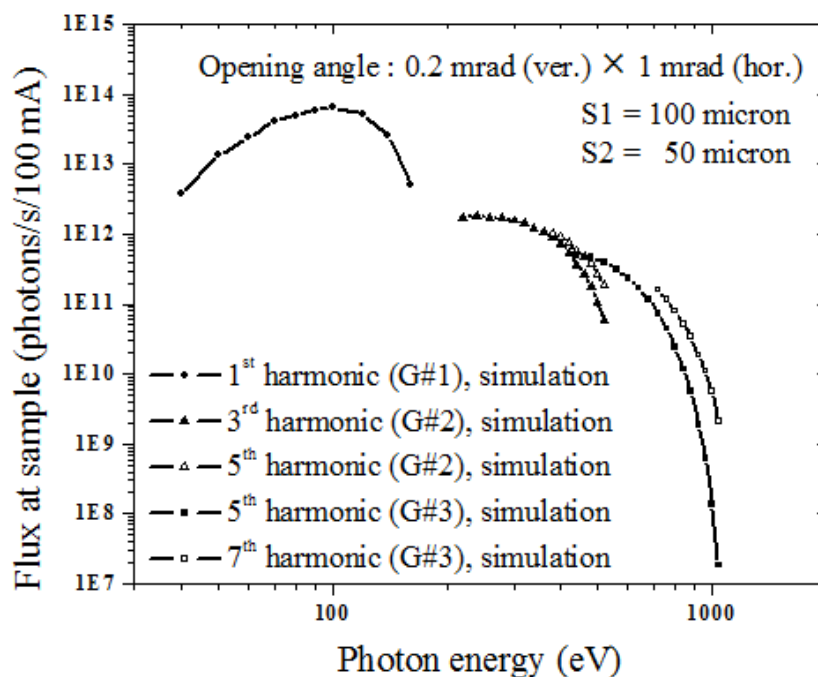


**Figure 4.27** Calculated flux of the PEEM branchline at sample position assuming an current in the storage ring 100 mA. The calculated flux includes the reflectivity of the mirrors, the efficiency of grating, the reflectivity of the grating and the beam intensity after the entrance and exit slits.

2400 lines/mm. The beam size at the sample position for a photon energy of 600 eV is shown in figure 4.30.

#### 4.6.2 PEEM position

For grating number 1, the groove density at the middle of the grating is 600 lines/mm. The beam size at the sample position for a photon energy of 40 eV is shown in figure 4.31.

For grating number 2, the groove density at the middle of the grating is 1200 lines/mm. The beam size at the sample position for a photon energy of 280 eV is shown in figure 4.32.

For grating number 3, the groove density at the middle of the grating is 2400 lines/mm. The beam size at the sample position for a photon energy of 600

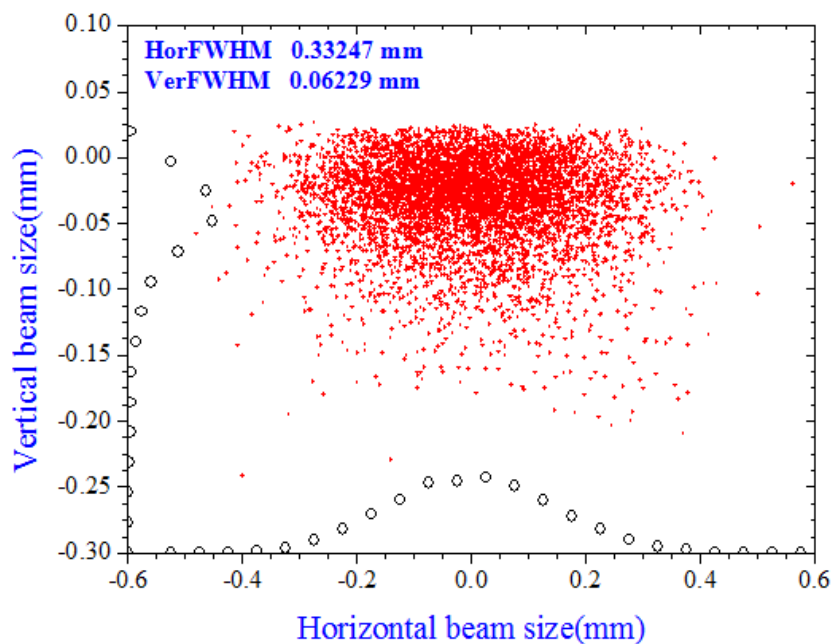


**Figure 4.28** The beam size at ARPES sample position for the photon energy 40 eV which is used grating number 1 and opening angle of  $0.2 \text{ mrad}^2$ .

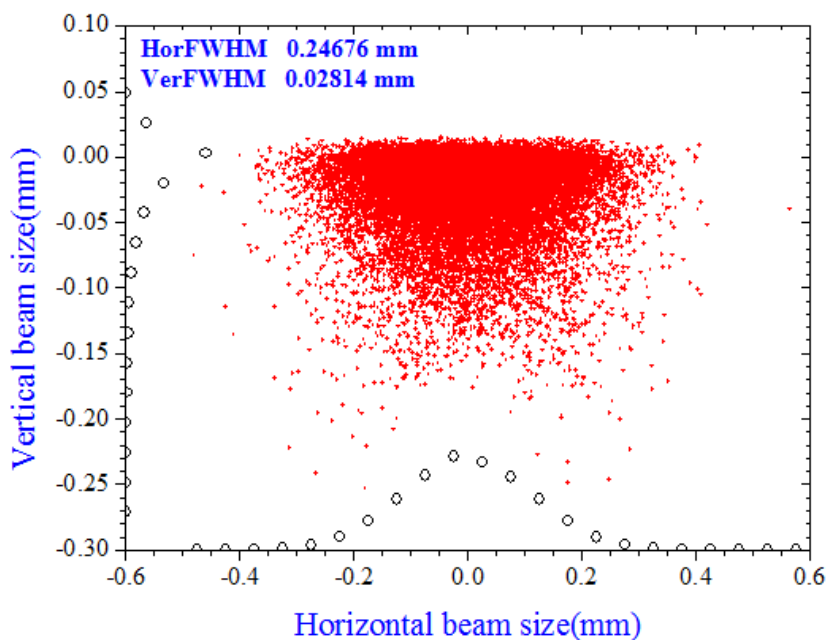


**Figure 4.29** The beam size at ARPES sample position for the photon energy 280 eV which is used grating number 2 and opening angle of  $0.2 \text{ mrad}^2$ .

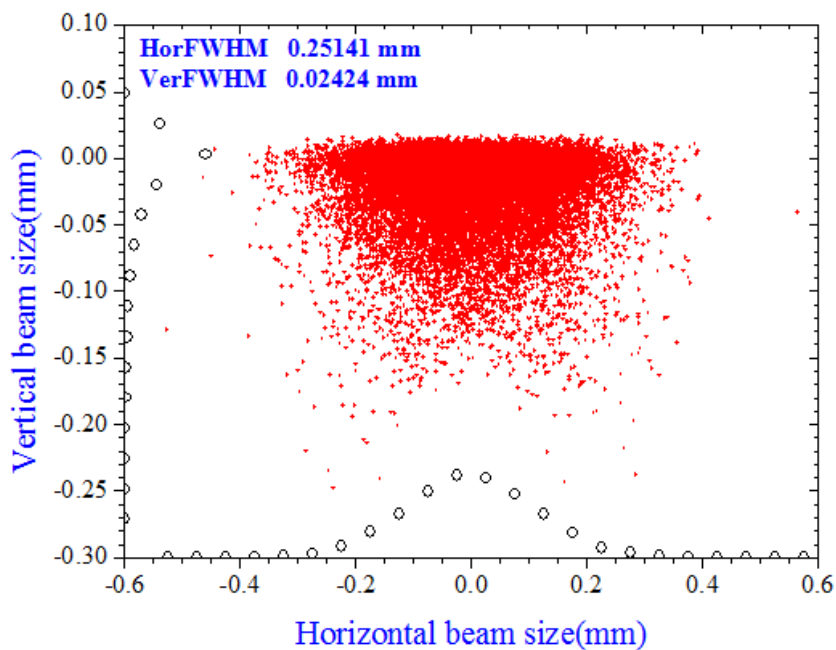


**Figure 4.30** The beam size at ARPES sample position for the photon energy 600 eV which is used grating number 3 and opening angle of  $0.2 \text{ mrad}^2$ .

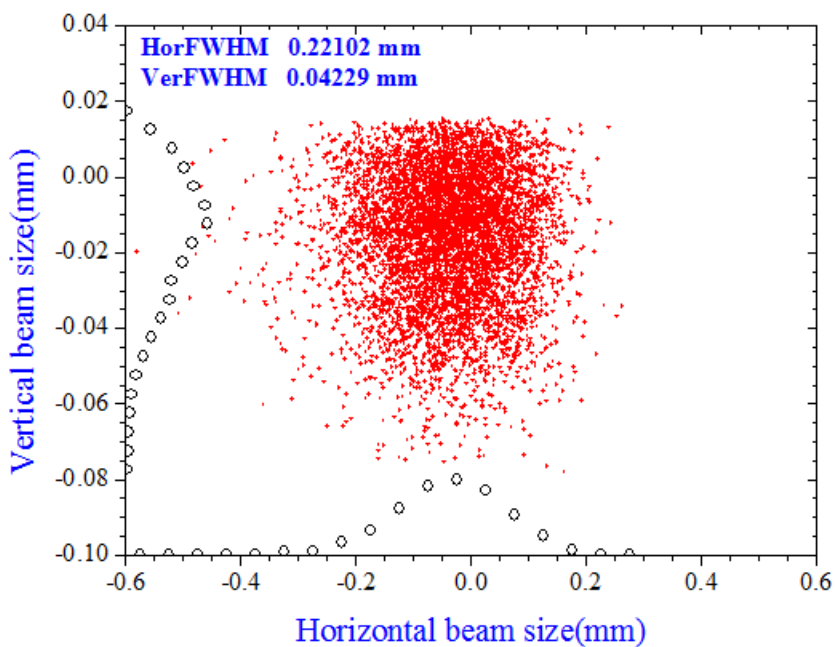


**Figure 4.31** The beam size at PEEM sample position for the photon energy 40 eV which is used grating number 1 and opening angle of  $0.2 \text{ mrad}^2$ .

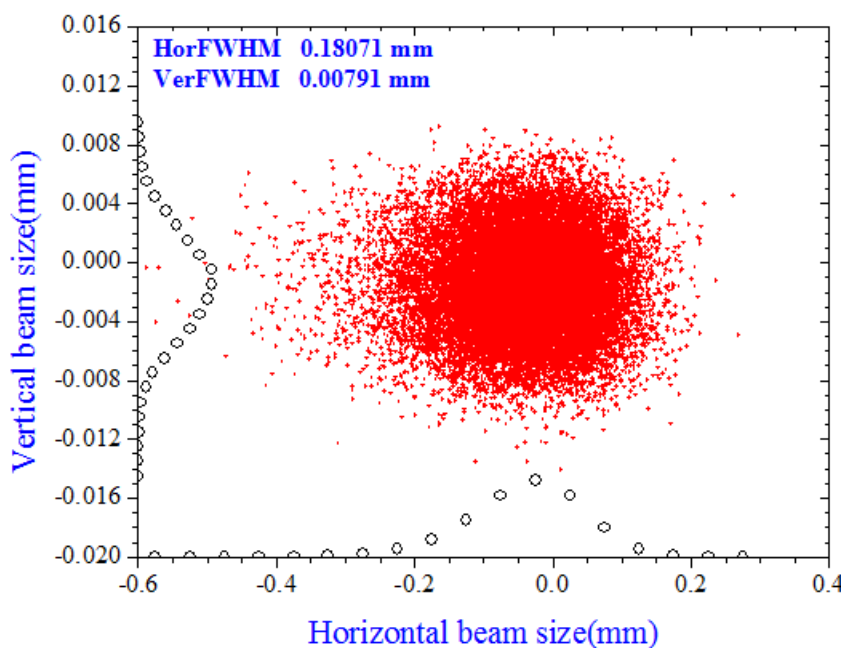


**Figure 4.32** The beam size at PEEM sample position for the photon energy 280 eV which is used grating number 2 and opening angle of 0.2 mrad<sup>2</sup>.

eV is shown in figure 4.33.

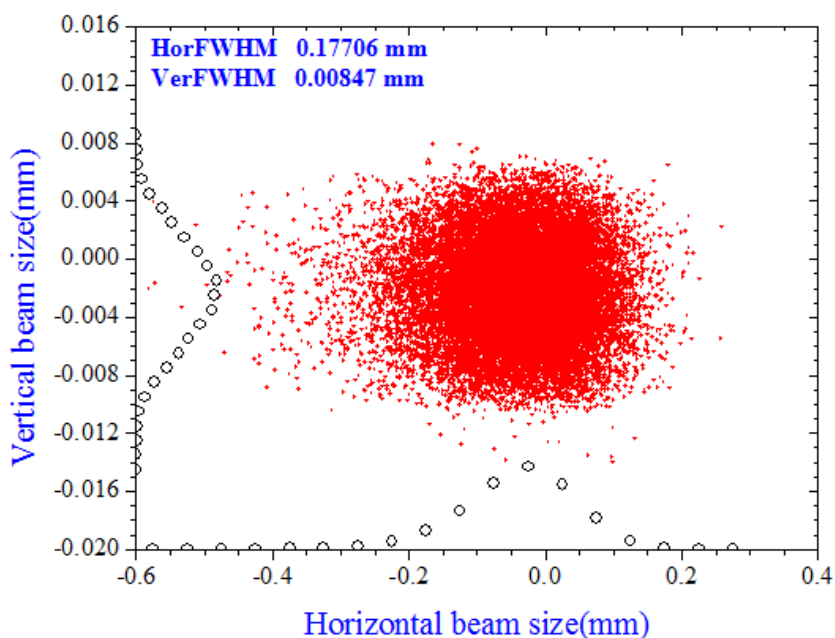


**Figure 4.33** The beam size at PEEM sample position for the photon energy 600 eV which is used grating number 3 and opening angle of 0.2 mrad<sup>2</sup>.

The ray tracing simulation results show that the beam sizes at the sample position of ARPES and PEEM agree well with the design.

For ARPES, the designed parameter of the horizontal demagnification is 5.985 for low and high photon energies, and the designed parameters of the vertical demagnification are 2.695 and 2 for low and high photon energies, respectively. As shown by the simulation results of 40eV photons, the full width half maximum of the photon source size is 2.86673 mm and 0.11238 mm for the horizontal and vertical directions, respectively. And the full width half maxima of photon beam size are 0.33247 mm and 0.06229 mm for the horizontal and vertical directions, respectively. The demagnification from simulation results are 8.6 and 1.8 for the horizontal and vertical directions, respectively.

In the case of PEEM, the designed parameter of the horizontal demagnification is 10 for low and high photon energies, and the designed parameters of the vertical demagnification are 4.359 and 3.235 for low and high photon energies, respectively. As shown by the simulation results for 40 eV photons, the full width half maximum of photon source size is 2.86673 mm and 0.11238 mm for the horizontal and vertical directions, respectively. And the full width half maxima of photon beam size are 0.22102 mm and 0.04229 mm for the horizontal and vertical directions, respectively. The demagnifications from simulation results are 12.97 and 2.66 for the horizontal and vertical directions, respectively.

## 4.7 Resolving power

The BL3 beamline is designed with resolving power about 10000 for all of energy range. The beam profile at the sample position with resolving power as 10000 is shown in figure 4.34. The simulation result shown the beam profile can be distinguished by different photon energies.

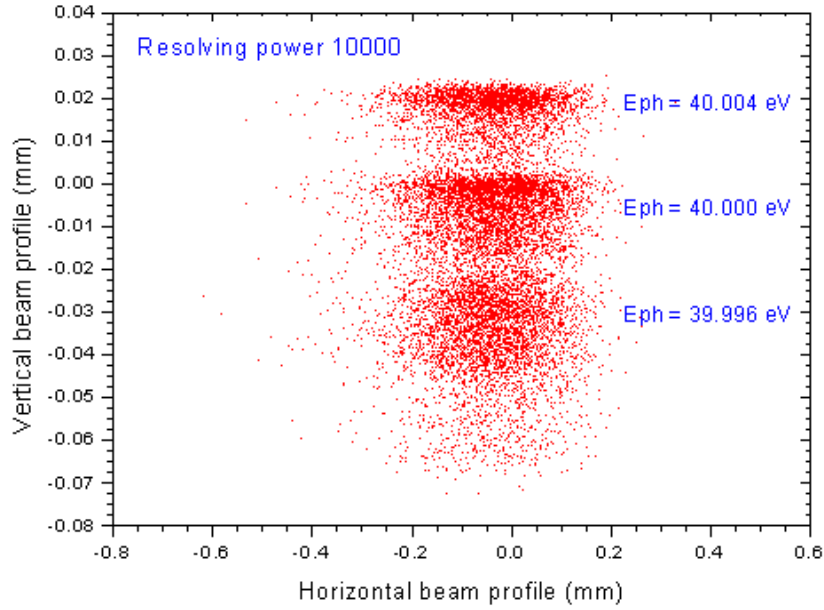


**Figure 4.34** The beam profile at the sample position of PEEM with resolving power as 10000 and the opening angle of  $0.2 \text{ mrad}^2$ .

## 4.8 Heat on the mask

The water-cooled mask is made of the stainless steel type 304 and has two apertures. The first aperture is used to deliver the undulator beam with the source radiation fan width of  $\pm 2 \text{ mrad}$ . The second aperture is used to deliver the bending magnet beam with the source radiation fan width of  $\pm 7.5 \text{ mrad}$  and is deviated from the undulator source by  $1.3^\circ$ . The front view of the mask is shown in figure 4.35. The properties of water at temperature of  $31^\circ\text{C}$  which is a cooling temperature of the SPS are given in table 4.12.

**Table 4.12** The properties of the water at temperature of  $31^\circ\text{C}$ .

Parameters	Value
Density ( $\rho$ )	$995.6 \text{ kg/m}^3$
Specific heat ( $C_p$ )	$4178 \text{ J/kg} \cdot ^\circ\text{C}$
Thermal conduction ( $k$ )	$0.6166 \text{ W/m} \cdot ^\circ\text{C}$
Dynamic viscosity ( $\mu$ )	$7.824 \times 10^{-4} \text{ kg/m} \cdot \text{s}$
Prandtl number ( $Pr$ )	$5.302$

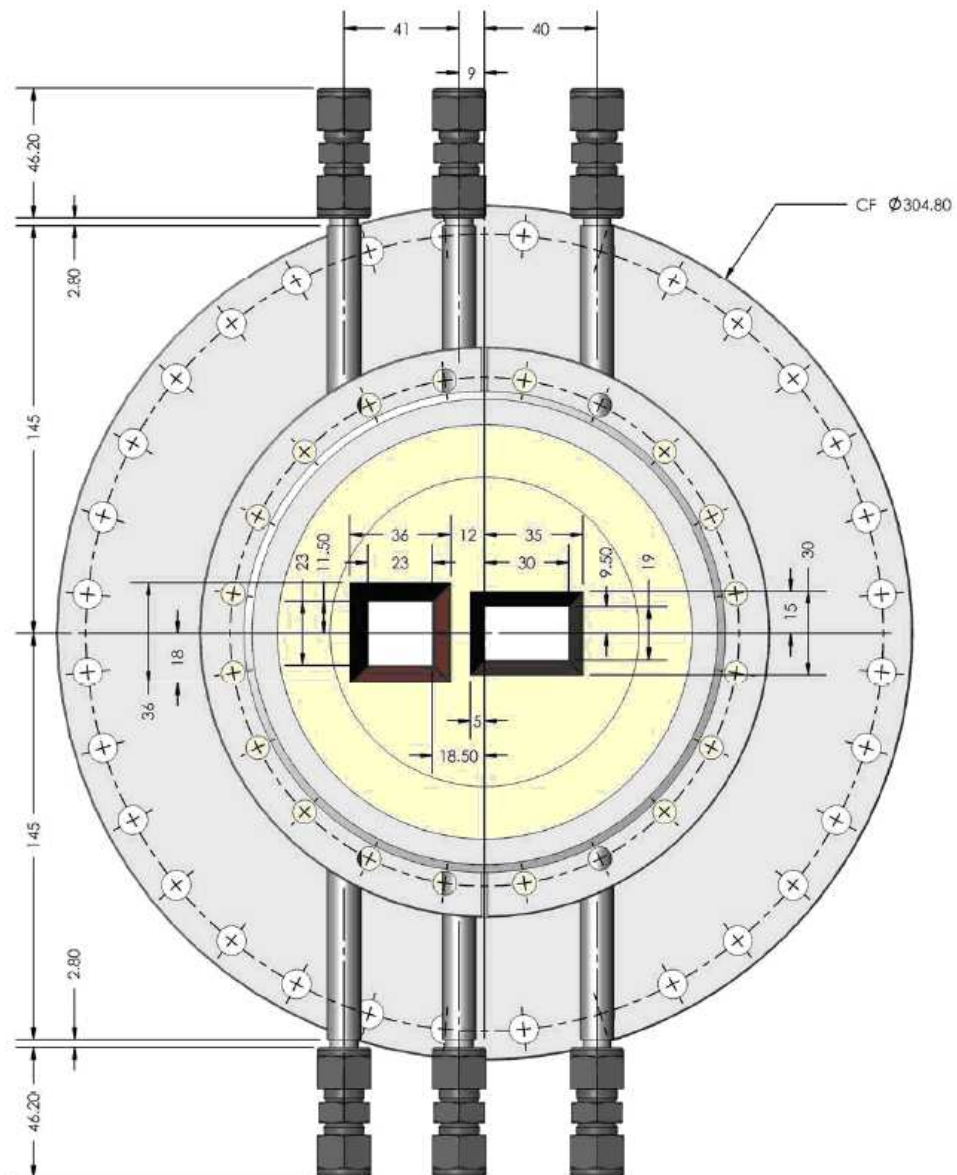


**Figure 4.35** The front view drawing of Mask of the BL3.2 beamline (a unit of length is millimeter).

The cooling tube has a diameter ( $D$ ) of 0.008 meter, so the cross section area is  $5.026 \times 10^{-5} \text{ m}^2$ . Furthermore the velocity ( $v$ ) of the water in the cooling tube is 1.9894 meter per second when the water flow rate is 6 litre per minute. To explain the viscous behavior of all Newtonian fluids, the dimensionless quantity

known as *Reynolds number* ( $Re$ ) is used, where

$$Re = \frac{\rho v D}{\mu}. \quad (4.3)$$

From the equation 4.3, the Reynolds number is 20,252. The number is higher than  $10^4$ , which means the flow mode in the cooling tube is turbulent. For the Reynolds number between  $10^4$  and  $10^6$ , the *Darcy friction factor* of the smooth tube is given as

$$f = (0.79 \cdot \ln(Re) - 1.64)^{-2}. \quad (4.4)$$

From the equation 4.4, the *Darcy friction factor* of the smooth tube is 0.026. The *Nusselt number* for the conditions  $0.5 \leq Pr \leq 2000$ , and  $3 \times 10^3 < Re < 5 \times 10^6$  is written by

$$Nu = \frac{(f/8)(Re - 1000) \cdot Pr}{1 + 12.7 \cdot (f/8)^{1/2} (Pr^{2/3} - 1)}. \quad (4.5)$$

From the equation 4.5, the *Nusselt number* is 133.9058. The convection coefficient is the input data for the simulation program such as Solid work which simulates the heat load. It is given as

$$h = \frac{Nu \cdot k}{D}. \quad (4.6)$$

The value of the convection coefficient is 10,321 W/m<sup>2</sup>.°C.

As the simulation result shown, the temperature on the surface of aperture for the U60 undulator is about 33.31°C with the cooling water temperature of 31°C and the water flow rate of 6 litre per minute.

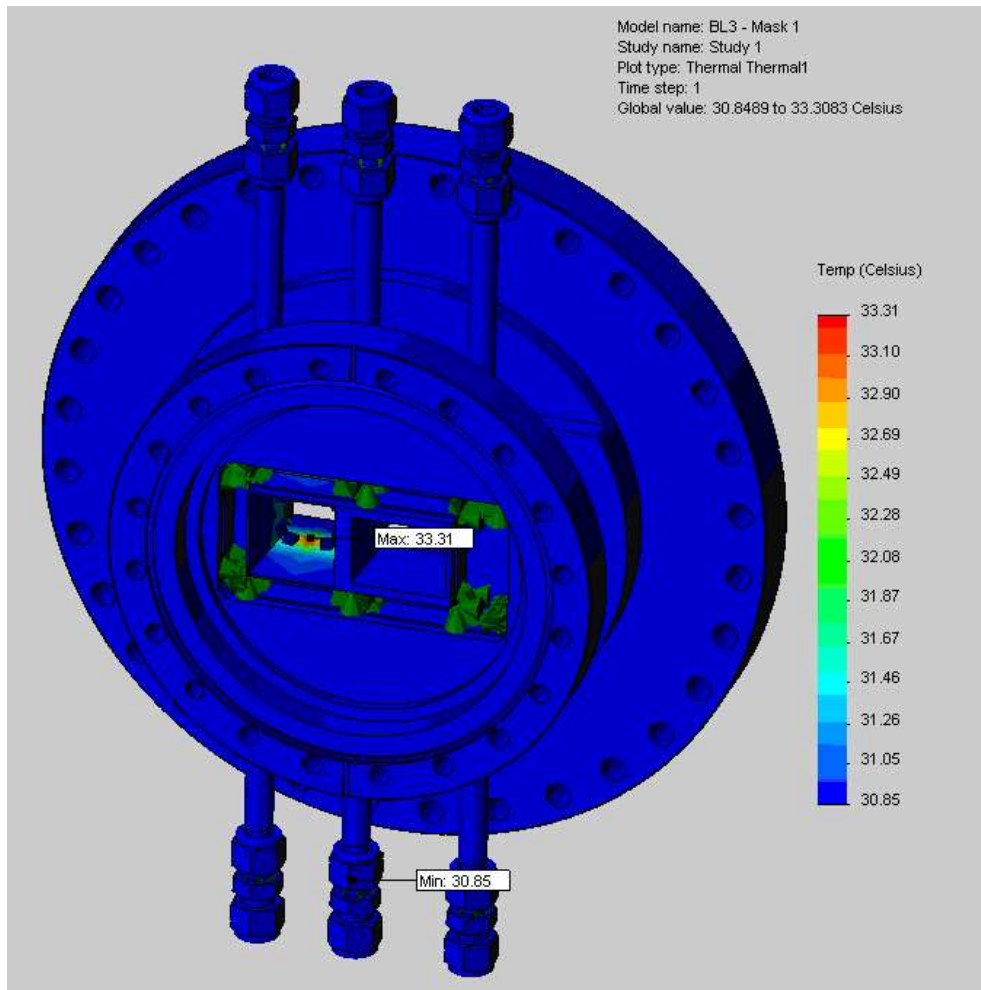


Figure 4.36 The power distribution on the Mask.

# CHAPTER V

## COMMISSIONING RESULTS AND DISCUSSION

This chapter provides the commissioning results and discussion on the performance of the undulator beamline. The first mission is to get a light from the undulator to the end-stations by adjusting the slits, mirrors and gratings. The beamline has two end-stations, namely PEEM and PES stations. In both end-stations, the light beams were observed on the sample positions with expected beam sizes in November, 2009. When the grating totally reflected a light, namely a white light, a visible light was observed in the sample position. Even though the grating monochromatized the light, fluorescence light was observed on the sample coated by the Ag-doped ZnS powder. The following sections show detailed performance of the beamline based on the commissioning results in comparison with the simulation discussed in the previous chapter. The alignment procedures of the optical elements are also described.

### **5.1 First photon beam alignment and PBPM results**

The optical elements installed in the beamline were aligned from upstream to downstream by either observing the visible and fluorescence lights or measuring the photocurrent on the optical elements. The photocurrent produced by the photoelectron emission from the materials excited by photons is measured from whether the gold-coated plate or the movable tungsten wire at a diameter of 0.05

mm. The latter is called a photon beam monitor (PBPM) located in front of M0 and entrance slit. The PBPM at the entrance slit has only a function of vertical translation with a manual drive, while the PBPM at M0 the horizontal and vertical translations controlled by the computer-controlled stepping motors.

According to the PBPM measurement in front of M0 shown in figure 5.1, the photon beam was found to be in the vertical optical axis, while not in the horizontal direction. However, the PBPM results were quite different from the ray-tracing simulation in terms of the photon beam size as described in the inset of the figures. This result will be discussed later on.

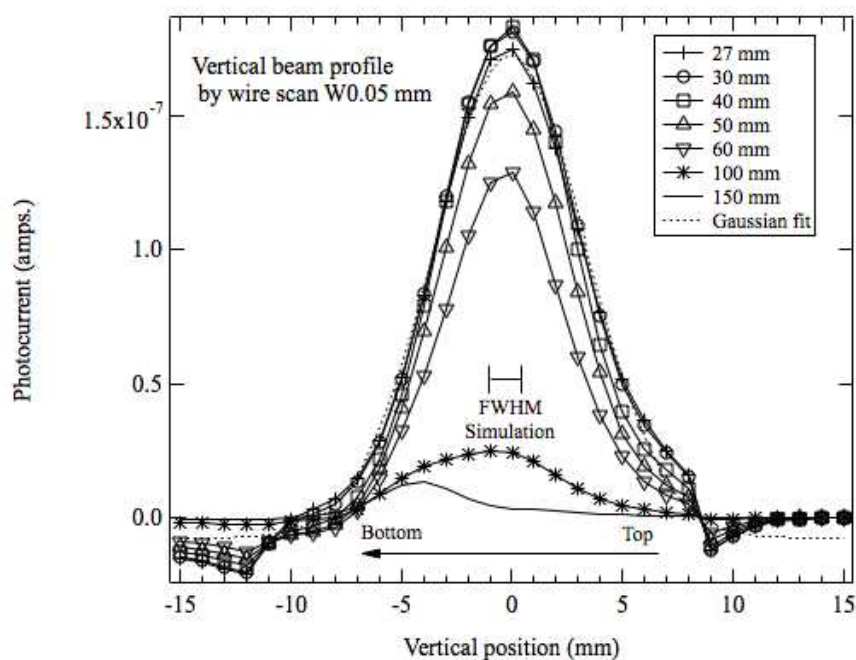


**Figure 5.1** The definitions of rotations and orientations of the pre-focusing mirror of the BL3.2 beamline.

## 5.2 The undulator photon energy spectrum

The undulator radiation is a quasi-monochromatic light, so that the photocurrent is modulated as a function of the photon energy on the basis of the

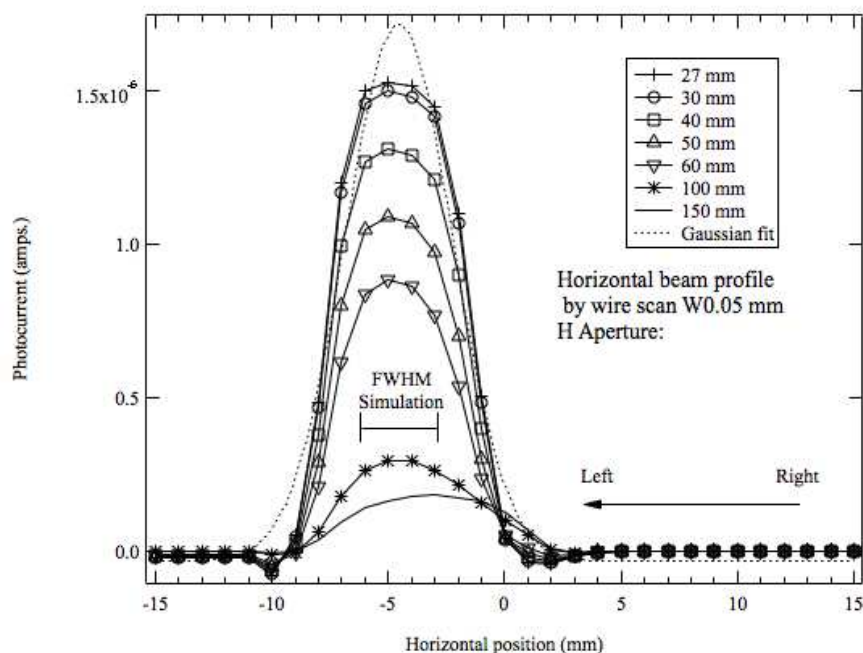


**Figure 5.2** The drain current measurement at behind entrance slit with slit width  $100 \mu\text{m}$  in the vertical translation ( $Z$ ) of the pre-focusing mirror ( $M_0$ ).

harmonic number as described in the previous chapter. To verify the undulator radiation characterized by the harmonic number, the photocurrent was measured on the gold-coated plate in the position behind the exit slit. The photon energy coming out from the monochromator was simply assumed using the diffraction parameters of gratings in the sine-bar mechanism. Figure 5.2 shows the undulator photon energy spectrum measured at an undulator gap of 55 mm and an opening angle of  $0.04 \text{ mrad}^2$ . The slit widths were set up at the  $200 \mu\text{m}$  in the entrance and exit positions. The calculated energy spectrum is also shown in the inset of figure 5.3, and shows good agreement with the experimental results. The gap between 160 and 220 eV in the measured spectrum corresponds to an unused window out of the grating efficiency as designed. The bandwidth of each harmonic photon was also evaluated using the analytical formula based on the undulator parameters, and found to be in good agreement with the experimental results.

The result of the energy spectrum shown in figure 5.3 was a first evidence of the undulator radiation in this beamline. Note that the photon energy and flux provided by the monochromator were further calibrated by measuring the Fermi edge of a gold sample and the photodiode current, respectively. These results will be shown in the following section.

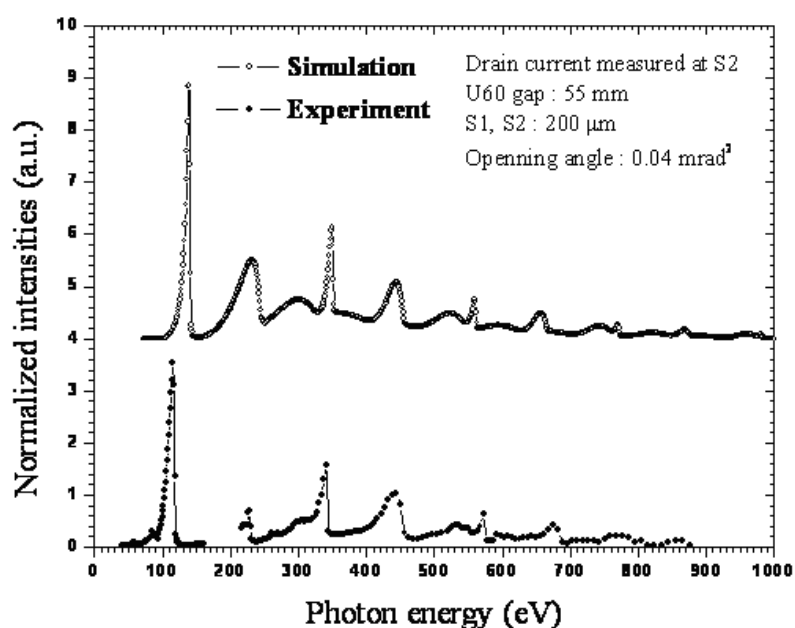


**Figure 5.3** The drain current measurement at behind entrance slit with slit width  $100 \mu\text{m}$  in the transversal translation (X) of the pre-focusing mirror (M0).

### 5.3 The pre-focusing mirror (M0) alignment

In the early stage of commissioning, the visible light from the undulator was successfully observed on the entrance slit by adjusting M0. However, the observed beam size was quite large being due to the overlap of unfocused bending magnet radiation. In the next stage, the fine adjustment of M0 was performed by finding a maximum photocurrent on the gold-coated plates behind the entrance and exit slits as a function of the linear translations and two rotations of M0. M0

was accurately controlled in a position by the four independent stepping motors shown in the figure 5.4. The definition of each stepping motor drive is described as follows:

- Vertical translation of M0 as  $Z$ : This allows M0 to move a height (up or down) in the perpendicular with the incoming photon beam.
- Transversal translation of M0 as  $X$ : This allows M0 to shift in the transversal direction to the incoming photon beam.
- Yaw of M0 as  $\theta_z$ : This adjusts the angle of incident on the mirror surface of M0 against the photon beam.
- Pitch of M0 as  $\theta_x$ : This allows M0 to tilt the mirror surface plane to the incoming photon beam.

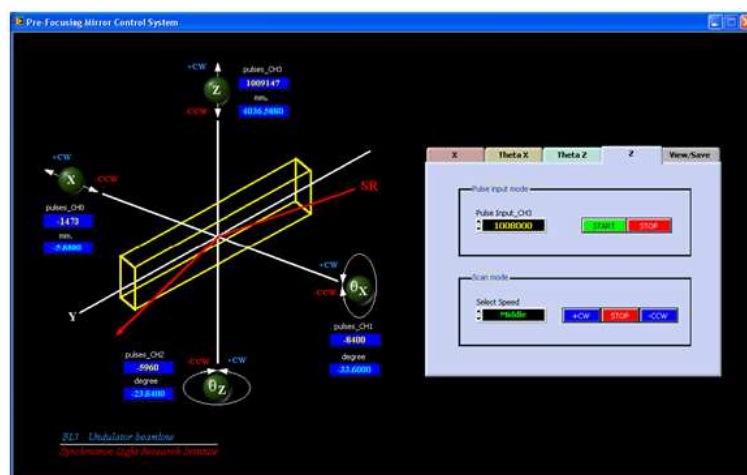


**Figure 5.4** The drain current measurement at behind entrance slit with slit width  $100 \mu\text{m}$  in the yaw ( $\theta_z$ ) of the pre-focusing mirror (M0).

Figures 5.5–5.8 show the measured photocurrent distribution in the entrance slit plotted with a step-pulse number output from each stepping motor in M0. An undulator gap of  $36.4525 \text{ mm}$  corresponding to the  $1^{\text{st}}$  harmonic energy

of 60 eV and 100  $\mu\text{m}$  of slit width were used to measure the photocurrent. All photocurrent was normalized at an electron storage current of 100 mA. Each peak position found in the figures shows no dependence on the undulator gap.

Note that all optical elements were positioned along the optical axis defined by the slit positions to minimize the influence of the electron orbit distortion or/and deviation to the photon beam alignment depending on the undulator gap. A horizontal center of each slit was defined using the V-shaped apertures in front of each slit. To get the photon beam in the optical axis, the  $X$  and  $\theta_z$  of M0 were carefully adjusted until the photocurrent maxima in the entrance and exit slits come into the same position in the  $X$  and  $\theta_z$ .

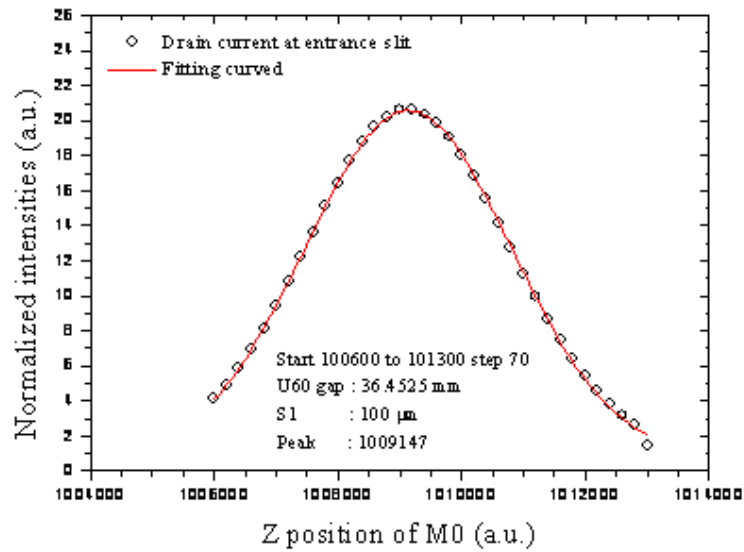


**Figure 5.5** The drain current measurement at behind entrance slit with slit width 100  $\mu\text{m}$  in the pitch ( $\theta_x$ ) of the pre-focusing mirror (M0).

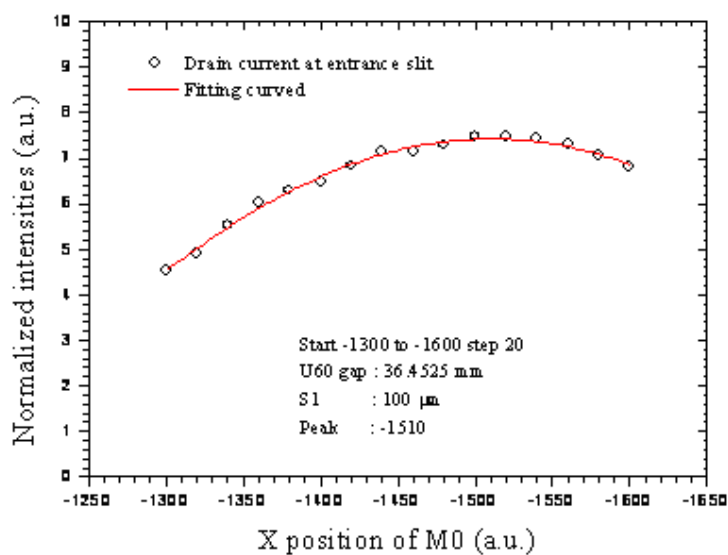


**Figure 5.6** The in-house developed software is used to measure drain current for slits alignment.

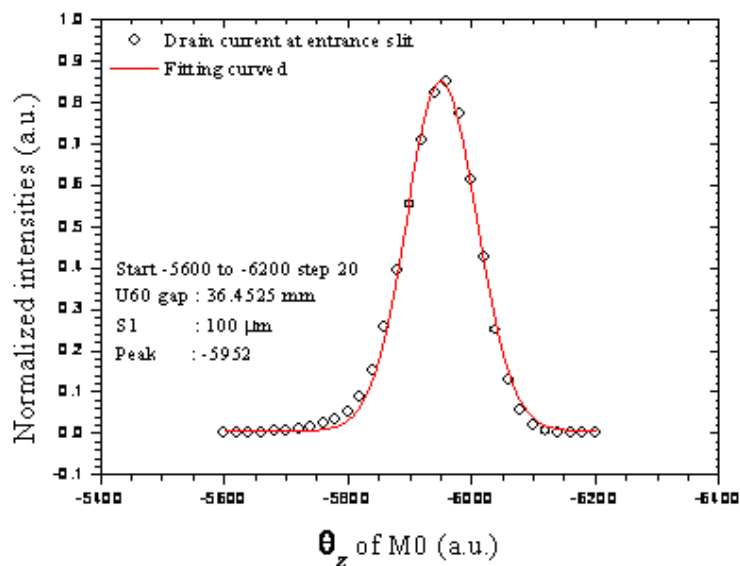


**Figure 5.7** The drain current measurement at behind entrance slit with slit width 100  $\mu\text{m}$ .

## 5.4 The slit alignment

The focal positions of M0 and grating monochromator were confirmed by measuring the photocurrent on the plate behind the slits as a function of linear

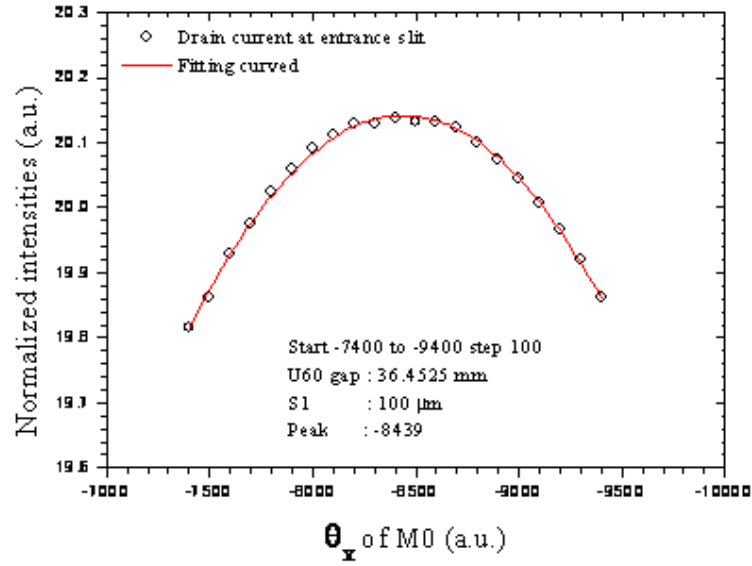


**Figure 5.8** The drain current measurement at behind exit slit with slit width 100  $\mu\text{m}$ .

translation along the optical axis. Because the linear translation along the optical axis must be manually moved, the in-house developed software was used to measure the photocurrent at a constant time interval set up in the graphical interface shown in figure 5.9. The focal positions of the white light were found at 17 and 36 mm to downstream for the entrance and exit slits as shown in the figures 5.10 and 5.11. An undulator gap of 55 mm, which provides a maximum photon flux at the 1<sup>st</sup> harmonic 110 eV photon energy, was used to maximize the photocurrent to make a clear peak structure in the photocurrent distribution. The deviation from the centers of each slit is acceptable in comparison with the designed monochromator arm length.



**Figure 5.9** The drain current measurement as a function of time at behind entrance slit with slit width  $100 \mu\text{m}$ .

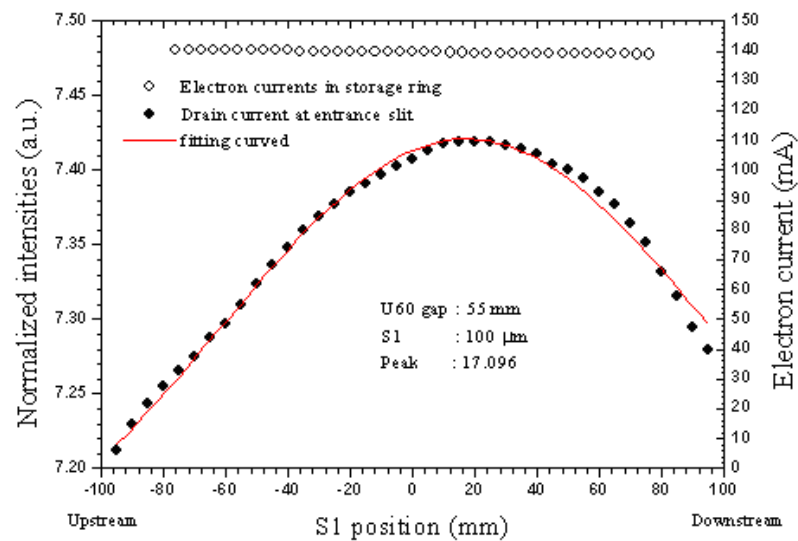


**Figure 5.10** The beam size at entrance slit position before and after open ABS.

## 5.5 The M0 stability

According to the time-dependent photocurrent measurements after ABS opened, the heat load effect on M0 from the undulator radiation was found to be

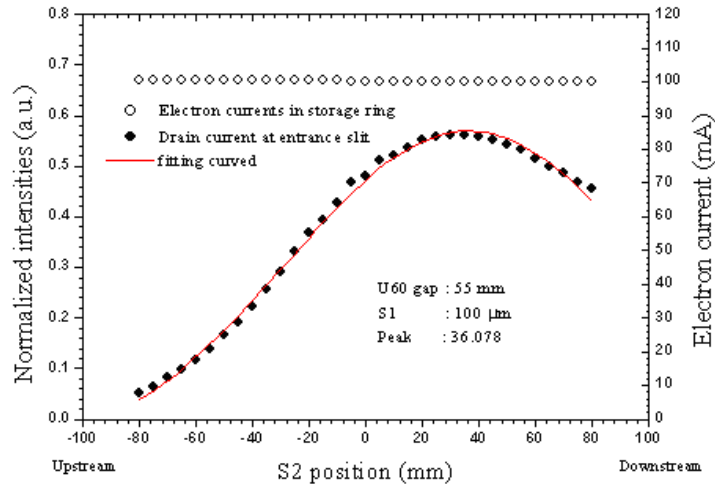


**Figure 5.11** The relationship between the undulator gap and magnetic field.

negligible. It is consistent with the results found in the focal position measurements in the slit positions. Figure 5.12 shows an 18% increment of the photocurrent in 3 hr. after ABS opening. Figure 5.13 shows a vertical PBPM profile in front of the entrance slit. Because PBPM was manually driven by hand, single profile scan took 10 min. In a time scale of 90 min. after ABS opened, the vertical profile appeared not to be affected from the heat load effect in a way that M0 locally deforms by a thermal expansion.

## 5.6 Photon energy scanning mechanism of the U60 undulator

From equation 2.16, the harmonic wavelength ( $\lambda$ ) simply changes with the magnetic field strength ( $B$ ) and the observation angle ( $\theta$ ). The on-axis magnetic field strength is a function of the undulator gap as shown in figure 5.14. In other words, by changing the undulator gap,  $\lambda$  can be varied. The effect of  $\theta$  will be discussed later on.

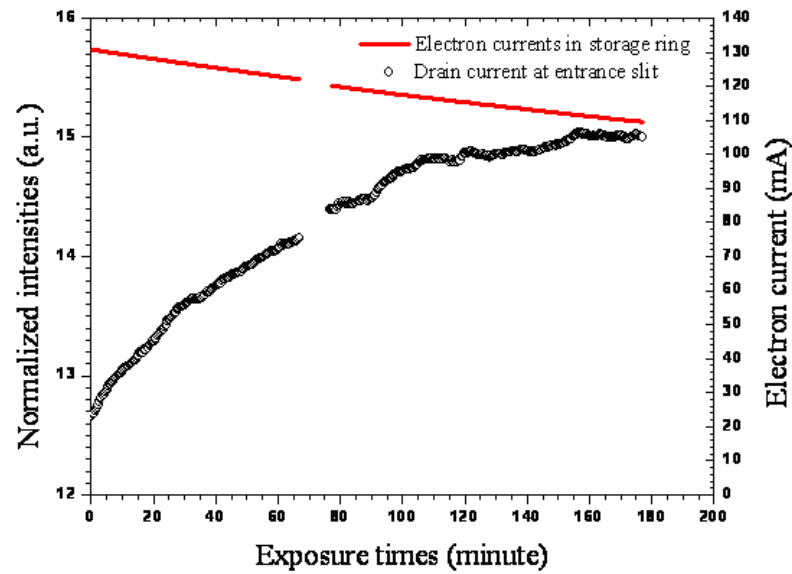


**Figure 5.12** The in-house developed software which is used for scanning undulator.

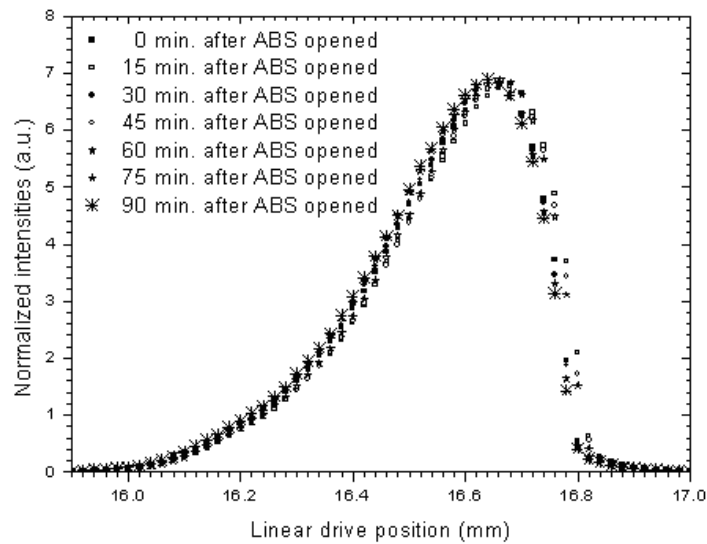


**Figure 5.13** The comparison of the U60 spectrum from the simulation and experiment results.

In the U60 undulator, the relationship between the undulator gap and magnetic field is described in an exponential function. According to the magnetic field

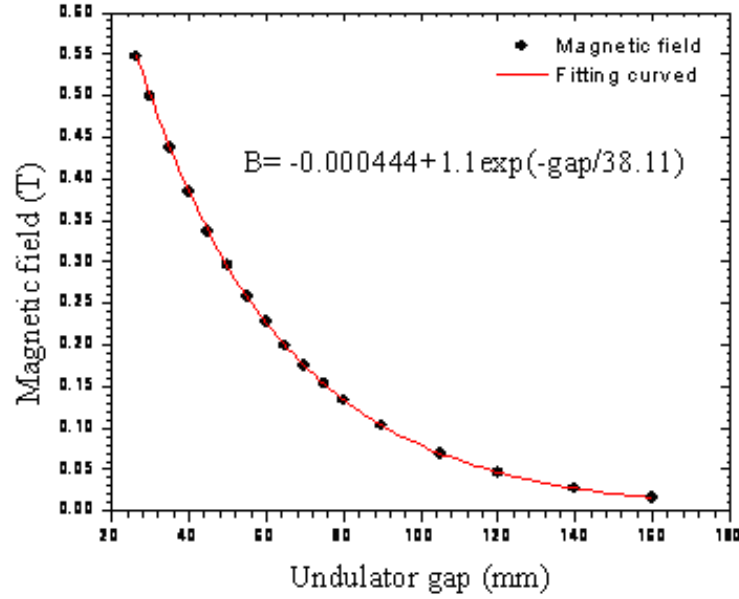


**Figure 5.14** The photon wavelength calibration curve for VLSPGs of BL3.2 beam-line by measured from photoemission spectra of gold.

measurement of the U60 undulator, the gap equation was obtained in the logarithmic form as follows:

$$Gap [mm] = -38.11 \cdot \ln \left( \frac{B [T] + 4.44 \times 10^{-4}}{1.1} \right) \quad (5.1)$$

This equation is used with the equation of 2.17 and 2.18 when the photon energy is scanned, for instance, in the measurement of absorption spectroscopy.

For example, if the photon energy is started from 40 to 160 eV, the magnetic field strength which is calculated from the equation 2.17, is varied from 3.065 to 0.922 and the corresponding of the magnetic field which is calculated from the equation 2.18, is varied from 0.5469 to 0.1645 Tesla. And the undulator is moved from the gap of 26.6 to 72.312 mm which is calculated from the equation 5.1.



**Figure 5.15** The new in-house developed software which is developed for scanning the undulator and grating in the same time and energy.

## 5.7 Photon energy calibration of the VLSPGs

In the front-end of the beamline, the slits and apertures were basically set up at a designed opening angle, which was calculated from the electron beam size in the storage ring and fundamental parameters of the undulator. As far as the undulator coherence is concerned, the beam should be shaped only in the range of the theoretical central cone.

To evaluate the central cone of the undulator radiation, the red shift should be measured as a function of the observation angle. Prior to the red shift measurements, the photon energy was carefully calibrated by measuring the Fermi edge of a gold sample to identify the exact harmonic peak energy. The photon energy was estimated from the sum of the work function of the photoelectron detector and the Fermi energy. The work function was assumed to be 4.2 eV based on the manufacturer calibration of the instrument.

The photoemission spectra were measured in the PEEM station. The CLAM2 electron energy analyzer (Thermo VG Scientific) was used to measure the photoelectron energy from the gold surface. The gold surface was sputtered by Ar ion with a kinetic energy of 0.5 keV prior to the measurement. The measurement was performed at room temperature, so that the Fermi edge profile is possibly fitted with a Fermi-Dirac function. Figure 5.16 shows an example of the photoemission spectrum on the gold near the Fermi edge. The estimated photon energy of 80.92 eV was calculated from the sum of the Fermi energy (76.72 eV) and the work function (4.2 eV), instead of the analytically calculated photon energy of 82 eV. Because the photoionization cross section of the valence electrons decreases as the photon energy increases, the Fermi energy was evaluated from the  $4f$  core level measurements in a higher photon energy range. A binding energy of  $4f$  core levels was assumed from the standard atomic binding energy table (<http://srdata.nist.gov/xps/>). According to the sine-bar mechanism, the wavelength of the monochromatized light is proportional to the linear translation of the sine-bar. Figure 5.17 shows a linear relation between the wavelength of the light and the linear translation of the sine-bar for each grating. The linear fitting coefficients in the results of each grating were used to evaluate the universal grating equation to set up a photon energy in the whole available photon energy range of this monochromator as described in the inset of figure 5.17.

## 5.8 Harmonic photon energy shift (red shift)

Here, let come back to the red shift observation using the finely calibrated grating monochromator. The first harmonic photon energy is known from the fundamental parameters of the undulator, and importantly varied with the gap and observation angle. In the first stage of the red shift measurement, however,

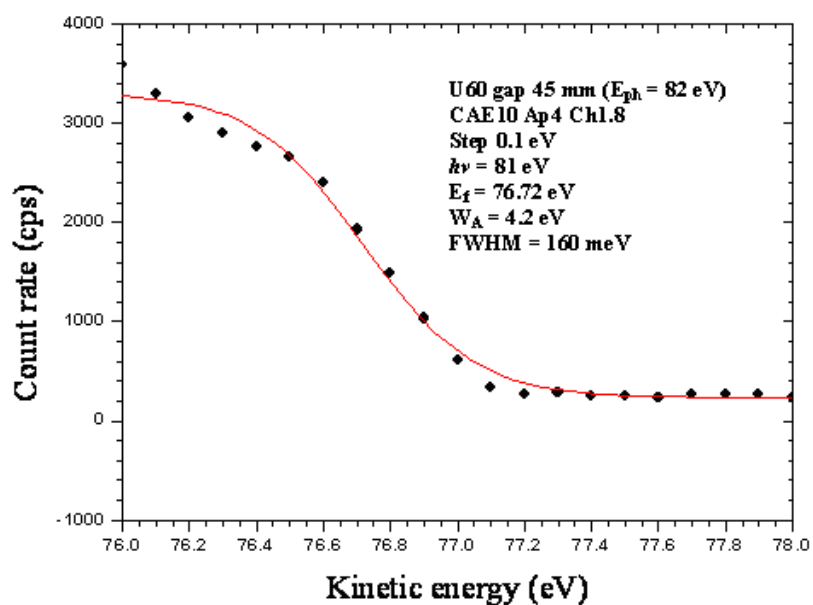


**Figure 5.16** The flux of the undulator from experiments is compared with simulation result.

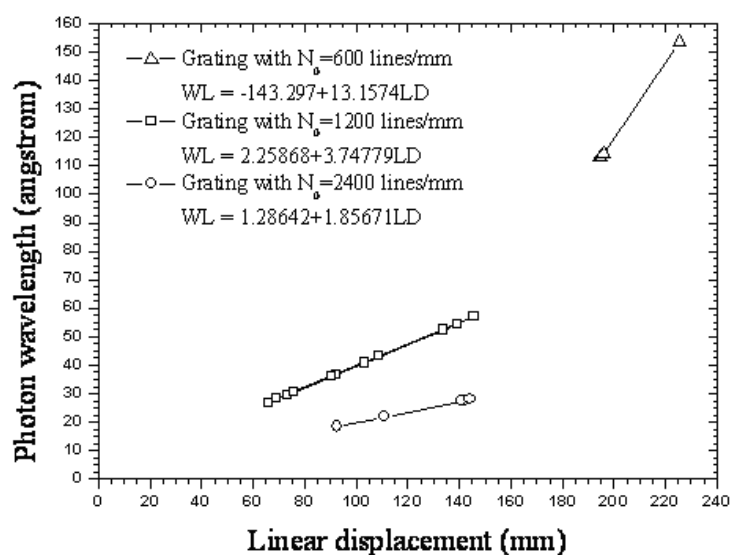


**Figure 5.17** The photoemission spectra of the Fermi edge of gold.

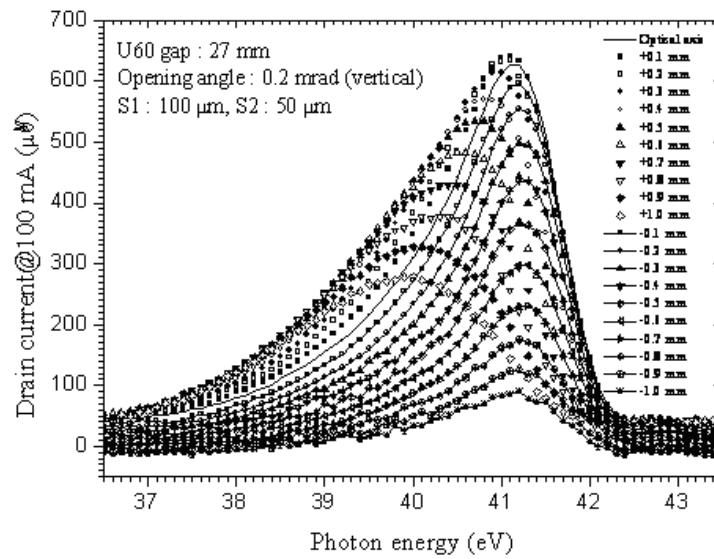
the gap and observation angle are fixed, and the photocurrent is measured as a function of the photon energy controlled only by the grating monochromator. In

the next stage, the energy spectrum is measured in the same way with a different observation angle. The observation angle is varied by shifting the vertical apertures at a constant width corresponding to a central cone opening angle of 0.2 mrad in the vertical direction.

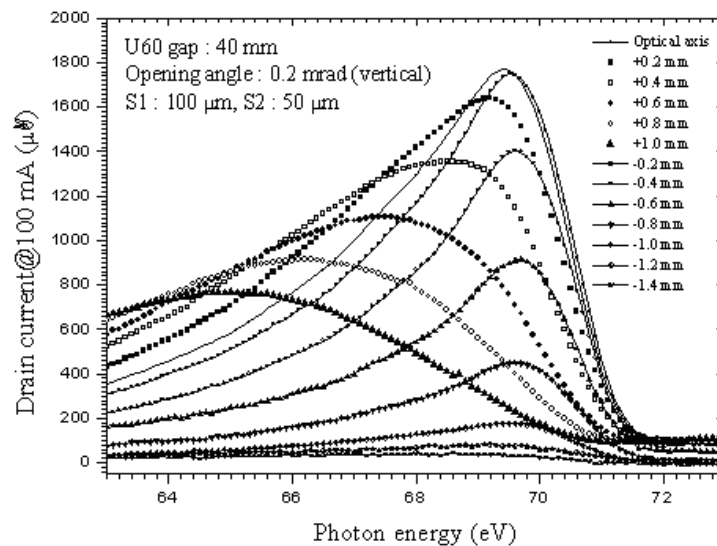
Figures 5.18–5.20 show a controversial beam profile of the undulator. The energy spectrum of the first harmonic peak shows a symmetric intensity distribution with respect to the optical axis. On the other hand, the peak energy shifts is asymmetric to the optical axis, which was clearly observed in the spectra when the aperture shifted to the downward. These abnormal red shifts in the vertical direction, which were against the theory of the undulator radiation, were observed in the measurements at three different undulator gaps as shown in figures. A possible cause is the alignment of the electron beam to the undulator in the vertical direction. In previously reported figures 5.1 and 5.2, PBPM also measured the unexpected large beam size by a factor of 8 and 2 in the vertical and horizontal directions. It is almost impossible to explain this large photon beam from the undulator based on the 100-micron electron beam without considering the misaligned electron beam orbit in the storage ring, and this is out of scope of this thesis.

## 5.9 Flux measurement at sample position

The photon flux was measured on the photodiode sensor at the position behind the exit slit. The quantum efficiency of the photodiode was provided from the standard data calibrated by the company (IRD, Inc.: AXUV100Al2). The drain current from the photodiode was measured in the pico-ampere order DC current monitor (Keithley Instruments Inc.) and normalized by an electron storage ring current of 100mA. To compare with the simulation, the photon flux at the sample position was estimated from the reflectivity of the mirrors in-between.

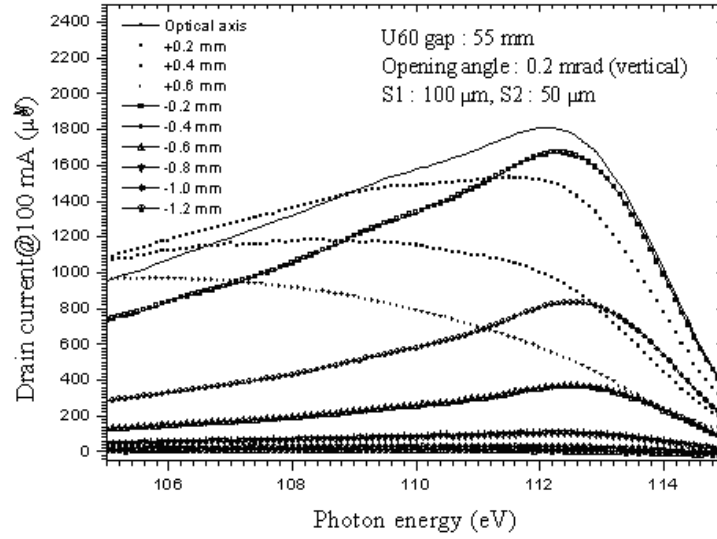


**Figure 5.18** The drain current behind exit slit is measured by scanning photon energy with the undulator gap is 27 mm.



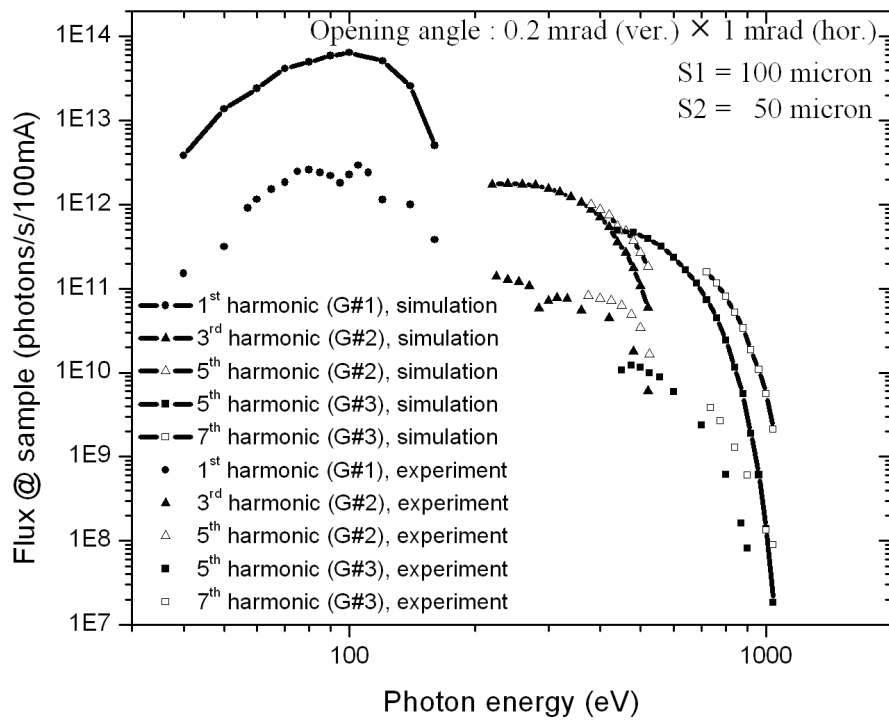
**Figure 5.19** The drain current behind exit slit is measured by scanning photon energy with the undulator gap is 40 mm.

Figure 5.21 shows the photon flux measured and simulated by the ray-tracing program in the beamline. The measured photon flux decreased by two



**Figure 5.20** The drain current behind exit slit is measured by scanning photon energy with the undulator gap is 55 mm.

orders of the magnitude in comparison with the simulation, especially in the lower photon energy ranges of each grating. This might be due to the horizontal deviation of electron trajectory caused in the constant dipole field produced by the earth, building and so on. This dipole field as a function of the undulator gap was previously reported (Rugmai et al., 2007). The correction coil compensating for this constant dipole field should be developed to improve the photon flux in the low photon energy ranges.



**Figure 5.21** The photon flux measured and simulated in the beamline at the sample position.

# CHAPTER VI

## CONCLUSIONS

- At the designed and 1<sup>st</sup> harmonic central-cone opening angle of 0.2 mrad and 1 mrad in the vertical and horizontal directions, the front-end slits reduce the maximum power to 24 W for the beamline optics. As a result, the front-end slits absorb a power of 43 W at an electron storage ring current of 100 mA. According to this estimation, the cooling unit for the slits was designed.
- The photon source of the U60 undulator with a period of 60 mm and a minimum gap of 26.5 mm was used to design the optical beamline. The photon energy scanning mechanism of the U60 undulator and the VLSPGs was integrated and controlled in the LabVIEW-based software.
- The meridional focusing of M0 was simulated from the ray-tracing calculation, and the radius of curvature for a required focusing position was designed. In the commissioning, the focal position was found in the appropriate range around the entrance slit.
- The stability of M0 was evaluated. The photocurrent, produced by the photoelectron excitation, at the position behind the entrance slit was saturated about 3 hr. after the ABS opened at an 18% improvement. The vertical beam profiles as a function of exposure time after the ABS opened was also found to be negligible.
- In the case of ARPES, the horizontal demagnification was designed at 5.985 for both low and high photon energies, and the vertical demagnifications were

designed at either 2.695 or 2 for low or high photon energies, respectively.

- In the case of PEEM, the horizontal demagnification was designed at 10 for both low and high photon energies, and the vertical demagnifications were designed at either 4.359 or 3.235 for low or high photon energies, respectively.
- The beamline was designed for a tunable photon energy range of 40 to 1040 eV with two exchangeable focusing spherical mirrors (M1/1 and M1/2) with two constant-included angles and three exchangeable VLSPGs.
- The wavelength provided from the beamline was calibrated by measuring a gold photoemission spectrum. For the grating with  $N_0 = 600$  lines/mm, the Fermi edge of gold spectra was used to evaluate the photon energy. For the grating with  $N_0 = 1200$  and 2400 lines/mm, the  $4f$  peak of gold spectra was used.
- The best performance of the beamline was expected when the electron beam quality in the storage ring would be improved, such as the smaller emittance and size of the electron beam. In particular, the COD correction is necessary to compensate for the influence of the electron orbit to the photon beam depending on the undulator gap.

## REFERENCES

## REFERENCES

- Attwood, D. T., Sommargren, G., Beguiristain, R., Nguyen, K. Bokor, J., Ceglio, N., Jackson, K., Koike, M., and Underwood, J. (1993). Undulator radiation for at-wavelength interferometry of optics for extreme-ultraviolet lithography. **Appl. Opt.**, 32(34):7022–7031.
- Briggs, D. and Seah, M. P. (1990). **Practical Surface Analysis 2nd edition Vol. 1 Auger and X-ray Photoelectron Spectroscopy**. England:John Wiley & Sons Ltd.
- Clarke, J. A. (2004). **The Science and Technology of Undulators and Wigglers**. New York:Oxford University Press, Inc.
- Codling, K. (1997). Atomic and Molecular Physics Using Synchrotron Radiation – the Early Years. **Journal of Synchrotron Radiation**, 4(6):316–333.
- Cramer, P., Bushnell, D. A., Fu, J., Gnatt, A. L., Maier-Davis, B., Thompson, N. E., Burgess, R. R., Edwards, A. M., David, P. R., and Kornberg, R. D. (2000). Architecture of RNA polymerase II and implications for the transcription mechanism. **Science.**, 288(5466):640–649.
- Duke, P. J. (2000). **Synchrotron Radiation Production and Properties**. New York: Oxford University Press, Inc.
- Elder, F. R., Gurewitsch, A. M., Langmuir, R. V., and Pollock, H. C. (1947). Radiation from Electrons in a Synchrotron. **Phys. Rev.**, 71:829–830.
- Jiang, Y., Lee, A., Chen, J., Ruta, V., Cadene, M., Chait, B. T., and MacKinnon,

- R. (2003). X-ray structure of a voltage-dependent K<sup>+</sup> channel. **Nature.**, 423(6935):33–41.
- Kim, K. J. (1995). Optical and power characteristics of synchrotron radiation source. **Opt. Eng.**, 34(2):342–352.
- Kukk, E., Wills, A. A., Langer, B., Bozek, J. D., Nayandin, O., Alshehri, M., Farhat, A., Cubaynes, D., and Berrah, N. (1998). Angle-resolved two-dimensional mapping of electron emission following Cl 2p excitations in the HCL molecule. **Phys. Rev. A.**, 57(3):1458–14883.
- Larabell, C. and Le Gros, M. A. (2004). X-ray tomography generates 3-D reconstructions of the yeast, *Saccharomyces cerevisiae*. **Mol. Biol. Cell.**, 15(3):957–962.
- Liu, G., Wang, G., Zhu, Y., Zhang, H., Zhang, G., Wang, X., Zhou, Y., Zhang, W., Liu, H., Zhao, L., Meng, J., Dong, X., Chen, C., Xu, Z., and Zhou, X. J. (2008). Development of a vacuum ultraviolet laser-based angle-resolved photoemission system with a superhigh energy resolution better than 1 meV. **Rev. Sci. Instr.**, 79(2):023105.
- Miller, L., Dumas, P., Jamin, N., Teillaud, J. L., Miklossy, J., and Forro, L. (2002). Combining IR spectroscopy with fluorescence imaging in a single microscope: Biomedical applications using a synchrotron infrared source. **Rev. Sci. Instr.**, 73(3):1357–1360.
- Peatman, W. B. (1997). Gratings, Mirrors and Slits Beamline Design for Soft X-ray Synchrotron Radiation Source. **Journal of Synchrotron Radiation**, 4(6):316–333.

- Rugmai, S., Dasri, T., Siriwattanapaitoon, S., Kwankasem, A., Sooksrimuang, V., Chachai, W., Suradet, N., Juthong, N., and Tancharakorn, S. (2007). Soft X-ray undulator for the Siam Photon Source. Ninth International Conference on Synchrotron Radiation Instrumentation: AIP Conference Proceedings, 879:335–338.
- Sands, M. (1970). **The Physics of Electron Storage Ring an Introduction**. California: University of California.
- Shin, H. J. (1993). Design of an undulator radiation beamline at the Pohang Light Source using variable-included-angle plane-grating monochromator. **J. Korean Phys. Soc.**, 34(4):350–358.
- Sinn, H., Glorieux, B., Hennet, L., Alatas, A., Hu, M., Alp, E. E., Bermejo, F. J., Price, D. L., and Saboungi, M. L. (2003). Microscopic dynamics of liquid aluminum oxide. **Science.**, 299(5615):2047–2049.
- Songsiriritthigul, P., Pairsuwan, W., Ishii, T., and Kakizaki, A. (2001). Photoemission beamline at the Siam Photon Laboratory. **Surf. Rev. Lett.**, 8:497–500.
- Talbayev, D., M. L. and Zhou, J. (2004). Antiferromagnetic resonance in LaMnO<sub>3</sub> at low temperature. **Phys. Rev. Lett.**, 93(1):017202.
- Wernet, P., Nordlund, D., Bergmann, U., Cavalleri, M., Odelius, M., Ogasawara, H., Nslund, A., L., Hirach, T. K., Ojamäe, L., Glatzel, P., Pettersson, L. G. M., and Nilsson, A. (2004). The structure of the first coordination shell in liquid water. **Science.**, 304(5673):995–999.
- Williams, G. P. (2001). **X-Ray Data Booklet**. Berkeley: Lawrence Berkeley National Laboratory.

Winick, H. (1994). **Synchrotron Radiation Sources A Primer**. Singapore:  
World Scientific Publishing Co. Pte. Ltd.

## APPENDICES

# APPENDIX A

## APPENDICES

### A.1 BL3 front-end

The front-end of the BL3 beamline has been designed to accommodate 2 optical beamlines; i.e. an undulator beamline and a bending magnet beamline. The front-end of the beamline serves primarily to prevent damage to the storage ring and radiation hazards to the user of the beamline. The main front-end of the BL3 beamline components are consisting masks, a heat absorber (ABS) with a bremsstrahlung shutter (BS), water-cooled slits, photon beam position monitoring (BPM) and vacuum gate valves. The water-cooled mask is installed with the exit gate valve as an all metal valve and isolated the front-end from the storage ring. The water-cooled mask is made of the stainless steel type 304 and has two apertures. The first aperture is used to deliver the undulator beam with the source radiation fan width is taken to be  $\pm 2$  mrad. The second aperture is used to deliver the bending magnet beam with the source radiation fan width is taken to be  $\pm 7.5$  mard and is deviated from the undulator source at  $1.3^\circ$ . The drawings in the front-end of top and side views are shown in Figure A.1. The heat absorber (ABS) has two sets relative with the apertures of mask. These heat absorbers are made of the oxygen free high thermal conductivity (OFHC) copper. The front face of heat absorbers is aligned  $45^\circ$  with respect with the beam axis. So, the reflected beam will be hit on a water-cooled flange. The water-cooled slits have two pairs which are installed in the front chamber (V1A, V1B, H1A and H1B) and rear chamber (V2A, V2B, H2A and H2B). The opening angle of the beam is defined

by the water-cooled slits which have an opening angle of 0.2 mrad and 1 mrad in vertical and horizontal directions, respectively.

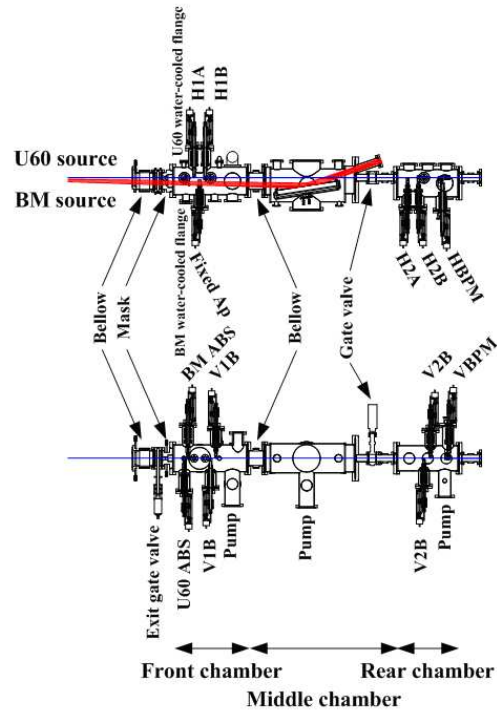


**Figure A.1** The front-end drawing of the BL3 beamline. The exit gate valve is installed to isolate the vacuum from the storage ring. Top view (a) and side view (b), are shown. The radiation source from U60 and bending magnet are passed trough to the front-end.

The front-end chambers of the first undulator beamline at the Siam Photon Laboratory (SPL) has been designed, fabricated and assembled in-house. The front-end chambers are installed inside the radiation shielding wall and connected with the exit gate valve, as shown in Figure A.1. The exit gate valve will be close when during the shutdown period time for the maintenance of the system. The front-end vacuum system consists of three main chambers (Front-, Middle- and Rear chamber), as shown in Figure A.3. The front and middle chambers are connected together by the bellow CF 304. The front chamber consists of U60ABS, BM ABS, Fixed Ap and slits (V1A, V1B, H1A and H1B). The back side of ABS

has a thick tungsten plate which used for protected the bremsstrahlung radiation. The middle chamber has two exit CF 114 ports. It is planed to install the mirror to reflect the bending magnet light which deviated from the center of the undulator light about  $1.3^\circ$  to BL3.1 beamline and the other port is used for the undulator to deliver the undulator light to BL3.2 beamline. Furthermore, the two exit ports of the Middle chamber are connected with the CF 114 pneumatic gate valve. The rear chamber is connected with the CF 114 pneumatic gate valve by CF 114 bellow. The components of the rear chamber consist of VBPM, HBPM and slits (V2A, V2B, H2A and H2B). The back side of the slit has a tantalum plate which has a sharp edge like a blade shape to cut a part of the beam. In addition, the BPM is used for the beam position measurement. All components in the front-end chamber have water-cooled units and are controlled by the stepping motor. Each of front-end chamber has the sputter ion pump (IP) and two titanium sublimation pump (TSP). After bakink at  $150^\circ$  for a week, the vacuum of the front-end reached down to  $2 \times 10^{-10}$  torr.

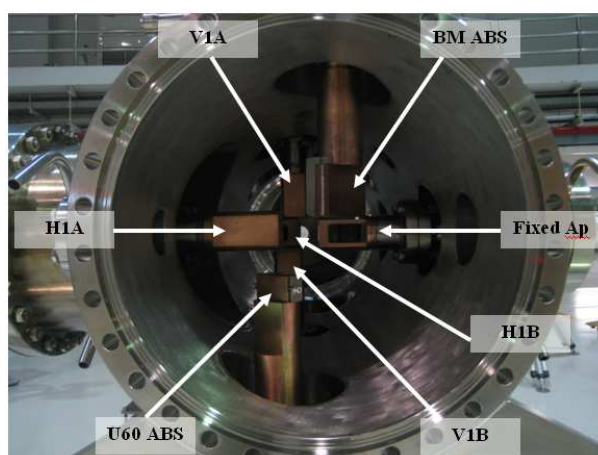


**Figure A.2** The photo of the front chamber of the BL3 beamline front-end. The image shows that the components are installed and aligned with the optical axis.

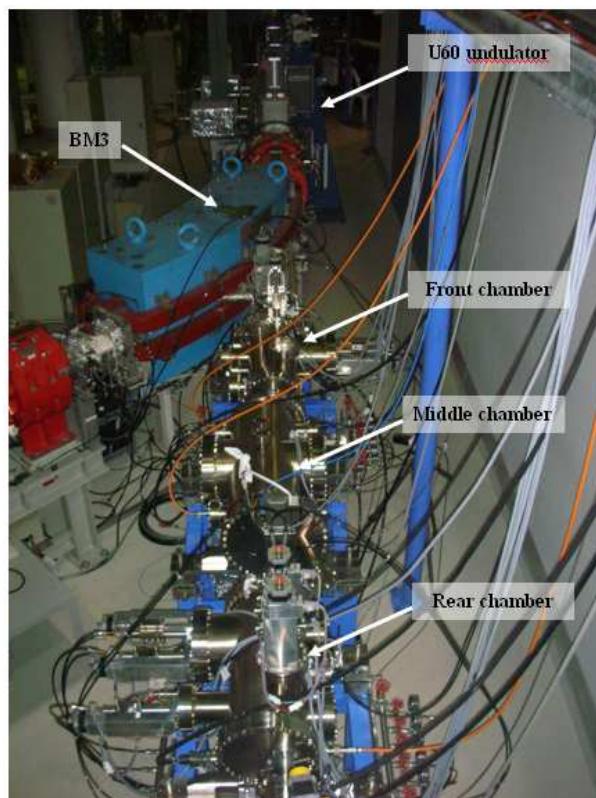


**Figure A.3** The photo of the front-end of the BL3 beamline connected to the bending magnet port number 3.

## A.2 Vacuum system

The VUV and soft X-ray beamline is under vacuum conditions, because of the photon energy of these regions is strongly absorbed by gas molecules in air. The ultra high vacuum at a base pressure below  $1 \times 10^{-9}$  Torr is operated for the VUV and soft X-ray beamline and avoids the contamination on surfaces of the optical elements with carbon. The diagram of the vacuum system of the BL3 beamline is shown in Figure A.4. The goal of the vacuum system of the BL3 beamline must be in the ultra high vacuum region for the whole length of the beamline. This is compatible with the vacuum requirements of the storage ring that the pressure in the storage ring is in the range of  $10^{-10}$  Torr and the end stations of the BL3 beamline are the photoemission techniques which required the

ultra high vacuum for surface researches. The chambers and ducts are fabricated in-house from stainless steel type 304 for the new mechanical components. And some components have a part of copper made from OFHC copper. Due to the budget constrained, the old mechanical components from the BL4 beamline are reused as many as possible. All seals are used by copper gaskets. The whole length of the BL3 beamline as illustrated in Figure A.5, is divided into eight sections, the each section is isolated by the vacuum gate valve. The vacuum gate valves in the BL3 beamline have two types as manual or pneumatic gate valves. The pneumatic gate valves are driven by the compressed air and controlled by the electric power.

The pressure of the whole length of the BL3 beamline is in the range of  $10^{-10}$  Torr. To get a good vacuum condition, the front-end chambers have been baked at  $200^{\circ}\text{C}$  for 1 week. Each component of the front-end has been baked one by one before re-assemble with motorized stage, and was baked them again with chambers at  $120^{\circ}\text{C}$  for 1 week. Front-end baking is should be carefully performed because of some part of the motorized stage are made of aluminum and fragile motors. All of vacuum components and chambers without optical elements have been baked at  $150^{\circ}\text{C}$  for 1 week.

In the beamline construction time, the vacuum components were installed from the 1<sup>st</sup> section up to the 8<sup>th</sup> section. The process was done by step by step in such away that the vacuum components were installed and baked one by one section. Only the sections of the optical elements with mirrors and gratings were baked again at  $120^{\circ}\text{C}$  for 1 week, otherwise those were baked at  $120^{\circ}\text{C}$  for 1 week once in a section.

When baking process was finished, leak test was followed after the vacuum components were cooled down to  $100^{\circ}\text{C}$ . The leak test is done by the quadrupole mass spectrometer (QMS) or residual gas analyzer (RGA). The major components

of residual gases are  $H_2$ ,  $CO$ ,  $CO_2$ ,  $CH_4$  and Ar. The normally of the leak test is detecting the helium mass by blowing the He gas outside the chamber. Then, sputter ion pumps (IP) are used with titanium sublimation pumps (TSP) to achieve ultrahigh vacuum condition. Cold cathode gauges (CCG) and hot filament gauges such as nudge ionization gauges (NIG) were used for measuring the vacuum pressure in the beamline. Furthermore, the beamline interlock were used to prevent the vacuum accident monitor by the CCG controller and interface unit that will be explained more detail in next topic.

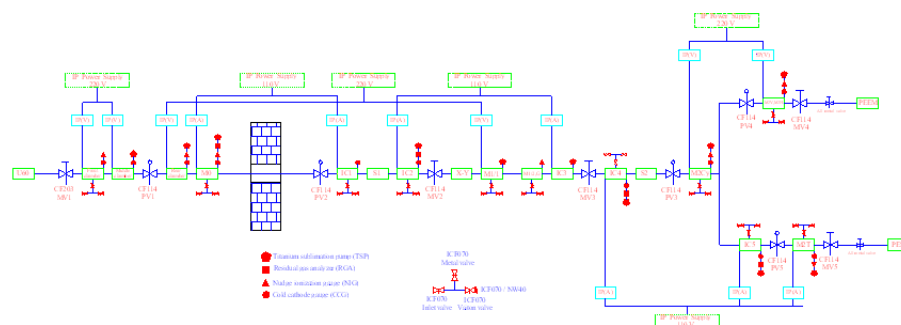


**Figure A.4** The diagram of vacuum system of the BL3 beamline.

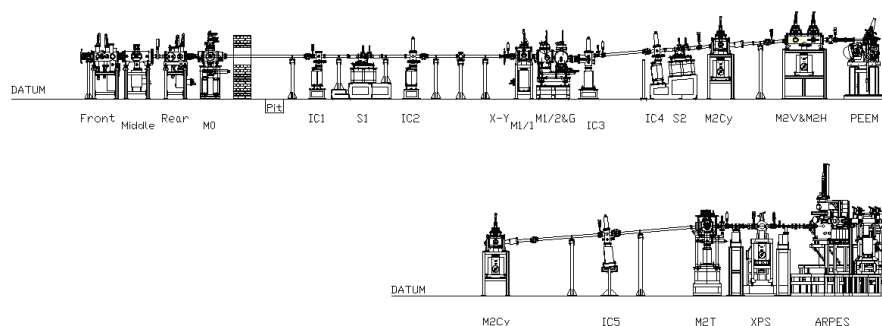


**Figure A.5** The drawing of the BL3 beamline. The drawing is shown the PEEM branchline (top) and the ARPES branchline (bottom). When the M2Cy mirror is out of the optical axis, the monochromatic beam is passed to the PEEM. On the other hand, when the M2Cy mirror is in the optical axis, the monochromatic beam is passed to the ARPES.

### A.3 Interlock system

The idea of the BL3 beamline interlock system is shown in Figure A.6. Programmable logic controller (PLC) was used to control the system. In this system, the main hardware device is an OMRON CS1 series and consists of CPU module, input and output units and interface units. The BL3 beamline consists of the vacuum interlock system which runs in the PLC, and the ABS with BS are under control of programs running on the main beamline computer. The main functions of the vacuum interlock system for BL3 beamline is to protect the SPS storage ring and other photon beamline from an accidental of the vacuum failure of the BL3 beamline or end-stations. The other function is to protect the uncooled vacuum components in the beamline from exposure to synchrotron radiation and the water-cooled beamline components from the interruption of the cooling water flow.

The input and output units were used to acquire status from the field devices such as the pressure switch for cooling-water flow to cooled components, the vacuum pressure, the manual and pneumatic gate valves (MV and PV), M2Cy position and ABS and BS status displayed on a touch screen. Only pneumatic gate valves are controlled by manual as shown in Figure A.7. Furthermore, the ABS and BS are controlled by PC.

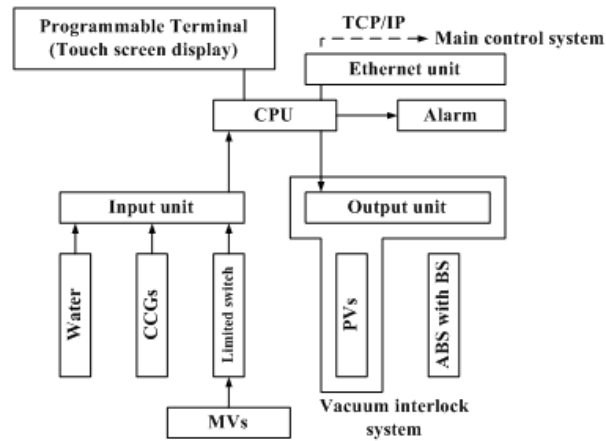


Figure A.6 The block diagram of the interlock system for the BL3 beamline.

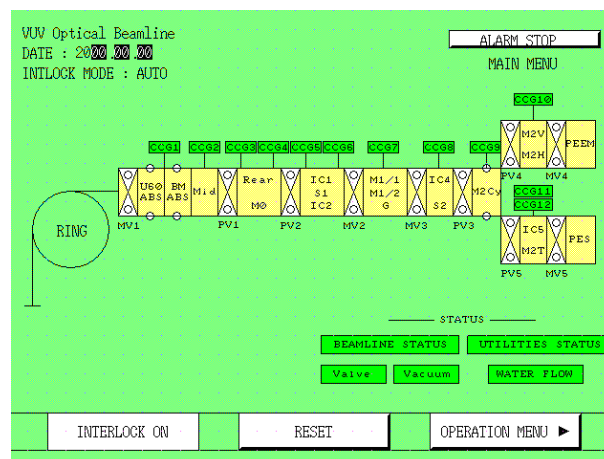


Figure A.7 The diagram of interlock of the BL3 beamline on the touch screen monitor.

**APPENDIX B**  
**PUBLICATION PAPER**



Available online at www.sciencedirect.com

Nuclear Instruments and Methods in Physics Research A 582 (2007) 100–102

**NUCLEAR  
INSTRUMENTS  
& METHODS  
IN PHYSICS  
RESEARCH**  
Section A

www.elsevier.com/locate/nima

## Design of the first undulator beamline for the Siam Photon Laboratory

P. Songsiriritthigul<sup>a,b,\*</sup>, B. Kjornrattanawanich<sup>a,c</sup>, A. Tong-on<sup>a,b</sup>, H. Nakajima<sup>a</sup>

<sup>a</sup>National Synchrotron Research Center, P.O. Box 93, Nakhon-Ratchasima 30000, Thailand

<sup>b</sup>School of Physics, Suranaree University of Technology, Nakhon-Ratchasima 30000, Thailand

<sup>c</sup>Universities Space Research Association, NSLS Beamline X24C, 75 Brookhaven Avenue, Upton, NY 11973, USA

Available online 12 August 2007

### Abstract

The first VUV/soft X-ray undulator beamline (BL3) is being constructed at the Siam Photon Laboratory. This beamline employs a varied line-spacing plane grating monochromator which operates in two constant-included-angle configurations to cover two photon energy ranges of 40–160 eV and 220–1040 eV. The two branchlines, designed for photoemission electron microscopy and photoemission measurements, will be operated in a time-sharing mode.

© 2007 Elsevier B.V. All rights reserved.

PACS: 07.85.Qe; 42.15.Eq; 42.15.Dp

Keywords: Synchrotron radiation; Undulator; VUV beamline; PEEM; PES

### 1. Introduction

The Siam Photon Source (SPS) [1] has been providing synchrotron radiation from bending magnets since the start of its operation. A planar undulator purchased from Danfysik [2] is the first insertion device to be installed to provide high radiation brightness in the VUV/soft X-ray region. Two different measurement techniques, i.e. photoemission electron microscopy (PEEM) and photoemission spectroscopy (PES) are planned for this undulator beamline 3 (BL3). One important consideration for this design work is to use most of the existing mechanical components from beamline 4 (BL4) [3]. BL3 will cover two photon energy ranges: 40–160 eV and 220–1040 eV.

### 2. Source

The source of BL3 is a planar Hallback-type undulator (U60), which has 41 periods and a period length of 60 mm. The expected flux density is several orders of magnitude higher than that of the bending magnet radiation, shown in

Fig. 1. The minimum photon energy of  $\sim 40$  eV is limited by the minimum undulator gap of 26 mm, corresponding to an effective deflection parameter  $K$  of 3.11 and the peak magnetic field of 0.56 T. The electron beam size and the emittance at the middle of U60 are the followings:  $\sigma_x = 1.08$  mm,  $\sigma_y = 0.05$  mm,  $\epsilon_x = 65.72$  nm rad and  $\epsilon_y = 0.65$  nm rad.

### 3. Beamline descriptions

The BL3 optical layout, consisting of a pre-focusing system, a monochromator and two post-focusing systems, is shown in Fig. 2. The two post-focusing systems will be operated in a time-sharing mode by a linear translation of a cylindrical mirror, M2Cy, located downstream of the monochromator. The monochromatic beam is horizontally deflected to the PES system. PEEM measurements are carried out when the mirror is retracted from the optical axis.

The pre-focusing system employs a water-cooled toroidal mirror, M0, to deflect the light beam  $6^\circ$  horizontally and sagittally focus the beam onto the entrance slit, S1, of the monochromator. A demagnification of 2 is chosen for M0 for flux optimization. M0 is located at a distance of

\*Corresponding author. National Synchrotron Research Center, P.O. Box 93, Nakhon-Ratchasima 30000, Thailand. Tel.: +66 44 217040; fax: +66 44 217047.

E-mail address: prayoon@nsrsc.or.th (P. Songsiriritthigul).

8940 mm from the source and S1 is located at a distance of 4470 mm from M0.

Because of a simple approach to obtain high resolving power by choosing proper line-space-variation coefficients of a grating and the simplicity of the photon energy scanning mechanism, a varied line-spacing plane grating (VLSPG) monochromator is adopted [4,5]. Two exchangeable focusing spherical mirrors (M1/1 and M1/2) with constant-included angles and three exchangeable VLSPGs are necessary to cover two photon energy ranges of 40–160 eV and 220–1040 eV. The included angles are  $167.5^\circ$  and  $172.5^\circ$  for the low- and high-energy ranges, respectively. A grating with groove density at the middle of the grating,  $N_0$ , of 600 lines/mm is used for the low-energy range. Two gratings with groove density  $N_0$  of 1200 and

2400 lines/mm are used for the high-energy range. Because the monochromator is optimized for the 220–1040 eV range, the demagnification of the focusing spherical mirror M1/1 is chosen to be 1.0 to minimize optical aberrations. Switching to the 40–160 eV energy range is done by moving M1/1 upward, allowing the beam to travel to the second focusing spherical mirror, M1/2.

The line-space-variation coefficients are defined in the groove density function as  $N(\omega) = N_0(1 + a_1\omega + a_2\omega^2 + a_3\omega^3 + \dots)$ . The coefficient  $a_1$ ,  $a_2$  and  $a_3$  and the exit arm length,  $r_2$ , of the grating are determined by minimizing the aberrations with procedures given elsewhere [6,7]. The  $r_2$ ,  $a_1$ ,  $a_2$  and  $a_3$  for all gratings are 3447.97 mm,  $-5.781 \times 10^{-4} \text{ mm}^{-1}$ ,  $2.500 \times 10^{-7} \text{ mm}^{-2}$  and  $-9.591 \times 10^{-11} \text{ mm}^{-3}$ , respectively. It should be noted that the advantage of VLSPG monochromator is that scanning of photon energy can simply be done by grating rotation. The monochromatic light is focused virtually at the position of the exit slit, S2. Thus no movement of the exit slit along the optical axis is necessary when photon energy is varied. In this design, there is no need to move the exit slit when switching the energy range. The total lengths of the monochromator are 9014 and 9012 mm for the  $167.5^\circ$ - and  $172.5^\circ$ -included-angle configurations, respectively.

For the PEEM branchline, the beam size on a sample should not exceed the maximum field of view of PEEM, typically  $\sim 500 \mu\text{m}$ . Because of the large horizontal size of the light source, the nominal horizontal demagnification of the beamline is chosen to be 10. Different combinations of mirrors for the post-focusing system have been tested by ray-tracing simulations using SHADOW program [8]. A combination of two cylindrical mirrors with meridional focus yields lowest aberrations and high photon flux. The beam at the sample position is shown in Fig. 3a. From ray-tracing simulations, the effective horizontal demagnification of the beamline for PEEM is close to the nominal

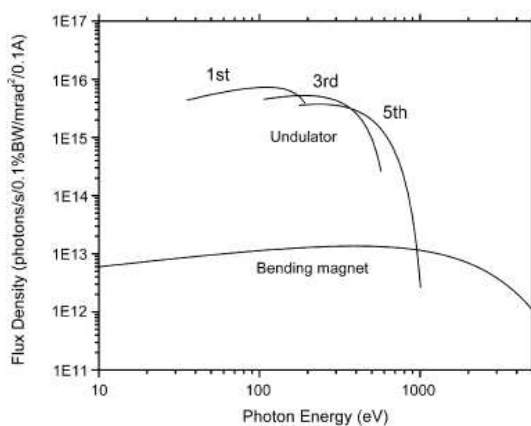


Fig. 1. Synchrotron radiation spectra from the bending magnet and the first undulator of SPS.

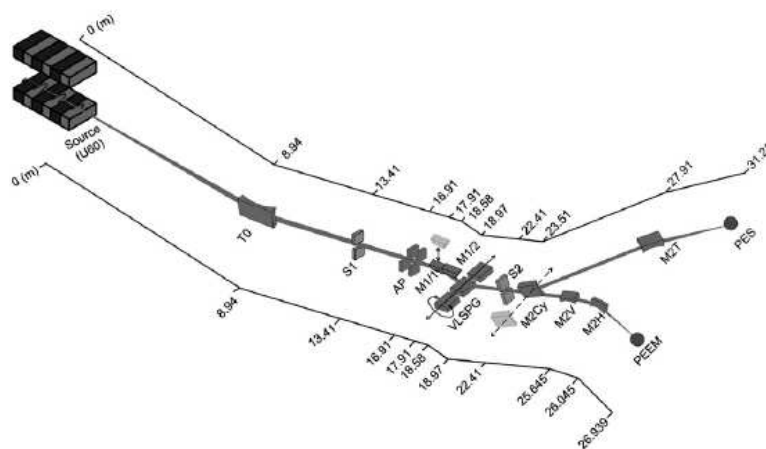


Fig. 2. Optical layout of BL3 at the Siam Photon Laboratory.

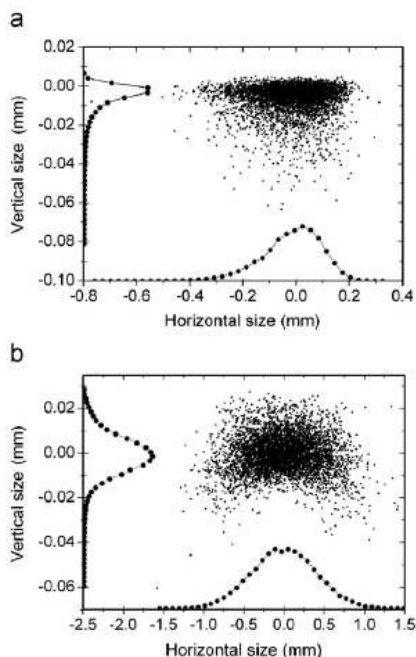


Fig. 3. Images of synchrotron beam at the sample position of the PEEM (a) and PES (b) systems when the opening angle is 0.2 mrad.

demagnification of 10 when central cone radiation of U60 is used. PEEM will be installed in such a way that the axis of the electron optics is in the dispersive plane of the monochromator, inclining towards to the downstream of the beamline to utilize most photons illuminated on the sample.

For the PES branchline, a combination of M2Cy and a toroidal mirror is used as a post-focusing mirror system. The image of photon beam at sample is shown in Fig. 3b. The parameters of the mirrors obtained from this design are given in Table 1.

Fig. 4 shows the calculated photon flux at sample assuming that S1 and S2 are fixed at 100 and 50  $\mu\text{m}$ , respectively. These slit widths correspond to resolving power of  $\sim 3000$  at the low-energy end and  $\sim 1200$  at the high-energy end of each grating.

Table 1

Parameters for the BL3 mirrors used in this work

	Surface type	Angle of incidence ( $^\circ$ )	$R$ (mm)	$\rho$ (mm)
M0	Toroidal	87	341,639	311.9
M1/1	Spherical	88.5	171,907	–
M1/2	Spherical	86	63,229.5	–
M2V	Cylindrical	87.75	62,960.7	–
M2H	Cylindrical	87	50,320.1	–
M2Cy	Cylindrical	87	–	57.6
M2T	Toroidal	87.75	84,055.4	259.1

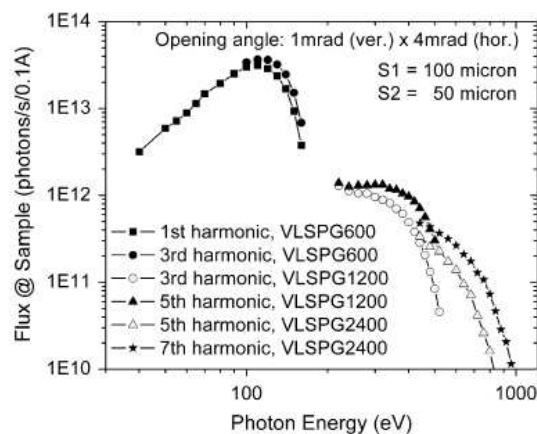


Fig. 4. Calculated photon flux at sample when the entrance and exit slits are 100 and 50  $\mu\text{m}$ , respectively.

#### Acknowledgments

The authors thank Dr. Steven Hulbert (NSLS) for useful suggestions on the beamline design, and Krekrit Sitisard (NSRC) for assistance in the beamline drawings.

#### References

- [1] P. Kengkan, et al., *J. Synchrotron Radiat.* 5 (1998) 348.
- [2] S. Rugmai, et al., *AIP Conference Proceedings* 879 (2007) 335.
- [3] P. Songsirithigul, et al., *Surf. Rev. Lett.* 8 (2001) 497.
- [4] M. Ito, M.I. Harada, T. Kita, *Appl. Opt.* 28 (1989) 146.
- [5] M. Fujisawa, et al., *Rev. Sci. Instrum.* 67 (1996) 345.
- [6] P. Songsirithigul, et al., *Nucl. Instr. and Meth. A* 467–468 (2001) 606.
- [7] H. Noda, T. Namioka, M.J. Seya, *Opt. Soc. Am.* 64 (1974) 1037.
- [8] B. Lai, F. Cerrina, *Nucl. Instr. and Meth. A* 246 (1986) 337.

# CURRICULUM VITAE

**NAME:** Anusorn Tong-on.

**GENDER:** Male.

**NATIONALITY:** Thai.

**DATE OF BIRTH:** 23 March 1978

**PLACE OF BIRTH:** Phetchabun, Thailand.

## **EDUCATIONAL BACKGROUND:**

1996 - 2000 Prince of Songkla University (Hatyai), Songkhla, Thailand.

Bachelor of Science (Physics)

2000 - 2003 Prince of Songkla University (Hatyai), Songkhla, Thailand.

Master of Science (Physics)

## **WORK EXPERIENCE:**

2003 - 2003 Synchrotron Light Research Institute (Public organization),

Nakhon Ratchasima, Thailand.